UNIVERSITÄT PADERBORN
Die Universität der Informationsgesellschaft

FAKULTÄT FÜR
ELEKTROTECHNIK,
INFORMATIK UND
MATHEMATIK

Investigation of Receiver Concepts for Coherent Optical Orthogonal Frequency Division Multiplexing Communication Systems

Von der Fakultät für Elektrotechnik, Informatik und Mathematik
der Universität Paderborn

zur Erlangung des akademischen Grades

Doktor der Ingenieurwissenschaften (Dr.-Ing.)

genehmigte Dissertation

von

M.Eng. Kidsanapong Puntsri

Erster Gutachter: Prof. Dr.-Ing. Reinhold Noé
Zweiter Gutachter: Prof. Dr.-Ing. Reinhold Häb-Umbach

Tag der mündlichen Prüfung: 04.02.2014

Paderborn 2014

Diss. EIM-E/238

Dedicated to my beloved prarents

วิชประสิทธิ์ และ เพลินจันทร์ พันธ์ศรี

Abstract

Coherent optical orthogonal frequency division multiplexing (CO-OFDM) is highly tolerant against channel impairments such as chromatic dispersion (CD) and polarization-mode dispersion (PMD) because of the added cyclic prefix (CP). To make CO-OFDM work, the signal must be preprocessed before the received one can be demodulated; additionally, CD and PMD compensation must be don after the received signal has been demodulated. Two important issues for OFDM receiver preprocessing are treated.

The first issue is synchronization. It is the alignment of the starting point of the OFDM symbols to acquire the fast Fourier transform (FFT) window. In case of mismatch, intersymbol interference (ISI) and intercarrier interference (ICI) will occur. A simple and powerful method to detect the starting point of OFDM frames, and to compensate for IQ swapping and inversion is proposed. The second issue is carrier frequency offset (CFO) correction. CFO leads directly to ICI. Two steps RF-pilot based method is proposed. Only one pilot tone is needed.

Next, for channel compensation, several pilots are uniformly inserted into each OFDM symbol. The proposed method can continuously track the effect of CD symbol-by-symbol, and it outperforms the common phase error method (CPE) method. It is performed in the frequency domain after the FFT unit to recover the information.

For long-haul communication, the accumulated CD effect becomes very large. To neglect ISI due to CD, the CP length must be large as well. However, these additional samples reduce the effective data rate, and the laser phase noise (PN) becomes a serious problem. Therefore, reduction or neglecting of CP for OFDM symbol is very attractive for our investigation. To increase the ISI tolerance, this thesis investigates the predistortion of OFDM symbols by the windowing method where a half and a full window are considered. All of them are done in the time domain.

Zusammenfassung

Kohärent optisches orthogonales Frequenzmultiplexverfahren (CO-OFDM) ist robust gegenüber Beeinträchtigungen aufgrund der Übertragungsstrecke wie chromatische Dispersion (CD) und Polarisationsdispersion (PMD) aufgrund des hinzugefügten zyklischen Präfixes (CP). Um CO-OFDM, muss das Signal in gewissem Maß vorverarbeitet werden. Werden zwei wichtige Gesichtspunkte für die Vorverarbeitung im OFDM-Empfänger behandelt.

Der erste Gesichtspunkt ist die Synchronisation, die Ausrichtung der Startpunkte, Bei Nichtübereinstimmung gibt es Inter-Symbol-Interferenz (ISI) und Interferenz zwischen den einzelnen Trägern (ICI). Eine einfache und wirksame Methode zur exakten Detektion des Startpunkts der OFDM-Symbole sowie Kompensation von IQ-Übersprechen und IQ-Inversion wird an dieser Stelle vorgeschlagen. Der zweite Gesichtspunkt ist Kompensation des Offset der Trägerfrequenz (CFO). CFO direkt zu ICI führt. Eine zweistufige auf einem RF-Pilotsignal basierende Methode wird hierbei vorgeschlagen. Nur ein Pilotsignal gebraucht.

Als nächstes werden zur Kompensation der Auswirkung der Übertragungsstrecke in jedes OFDM Symbol mehrere gleichmäßig verteilte Pilotfrequenzen eingefügt. Die hierbei vorgeschlagene Methode kann die Auswirkung der CD von Symbol zu Symbol nachverfolgen und übertrifft dabei die häufig verwendete Methode des gemeinsamen Phasenfehlers (CPE).

Bei langen Übertragungsstrecken häuft sich viel CD an. Um dennoch ISI vernachlässigen zu können, muß das CP sehr groß sein. Leider führen diese zusätzlichen Abtastpunkte einerseits zu einer Reduktion der effektiven Datenrate, andererseits wird Phasenrauschen des Lasers zu einem ernsthaften Problem.

Die Reduktion des CP für OFDM sehr interessant für unsere Untersuchung. Demnach schlägt diese Dissertation für die Erhöhung der ISI-Toleranz eine Vorverzerung durch Fensterung vor, wobei Fenster für halbe wie ganze Symboldauern Verwendung finden.

ACKNOWLEDGEMENTS

I am greatly indebted to my advisor, Prof. Dr.-Ing. Reinhold Noé, for his invaluable comments on the completion of this dissertation and for his patient guidance, supervision and encouragement throughout this study. Furthermore, his wisdom and knowledge has been invaluable to the development of idea in the study.

I would like to express my gratitude to Dr.-Ing. David Sandel and Prof.Dr.-Ing. Sebastien Hopmman for all invaluable discussions, imparting their knowledge and experience, which are really helpful.

I would not have finished if I worked without Dr.-Ing. Ali Al-Bermani, M.Sc. Omar H.A. Jan, M.Sc. Saleh Hussin, Dip.-Ing Christian Wördehoff, M.Sc.Muhammad Fawad Panhwar and M. Sc. Mohamed El-Darawy. They spended a lot of very valuable time to help me to develop my experimental systems and theoretical discussions.

To Dr.-Ing.Vitali Mirvoda and Dr.-Ing.Banjamin Kock, I would like to express my deepest thanks for their help, advice and enjoyable in the coffee time.

To Herr.Bernhard Stute, Herr.Michael Franke, Herr.Gerhard Wieseler, I could not have done this without their support. Thanks for their help, friendship and compassion.

I would like to thank Ms.Montakarn Petapirak and Mr. Kornpatsitt Promasa for thier help to prove English and check every detial of this dissertation.

I could not have lived here comfortably without Ms.Suchada Byer, Mr.Marious Nueman and family Walter. Many thanks for everything here in Paderborn.

I want to express my gratitude to my parents and my family for their patience and encouragement throughout the period of this accomplishment.

Finally, I would like to thank Rajamangala University of Technology Isan, Khon Kaen Campus, Thailand, for the financial support.

List of contents

List of Figures

List of Tables

CHAPTER 1

Introduction and Motivation

1.1 Overview

It is well-known that the demand of the Internet application is currently increasing, especially in multimedia field. These applications include YouTube, Internet protocol television (IPTV), and live internet video streaming. A high capacity telecommunication facility to serve these modern applications is required. A high capacity media, e.g., fiber-to-the-home (FTTH), will be introduced to every household in a very near future [1]. To fulfill these high capacity demands, it would be needed to operate backbone networks with multiplexed transmission systems; one of the most common multiplexing techniques used presently is wavelength-division multiplexing (WDM) [2-3]. However, each WDM channel bandwidth is limited to 50 GHz or 100 GHz only. Therefore, another solution to increase the capacity of the same spectrum bandwidth is needed. One solution is to develop a more advanced modulation format that can carry more bits of information per symbol and provide greater bandwidth efficiency. Examples include quaternary phase-shift keying (QPSK) and 16-quadrature amplitude modulation (QAM) modulation format, which offer 2 and 4 symbols, respectively. There are variations in QAM, such as 16-QAM, 32-QAM, 64-QAM and so on, which are generally referred to *M-ary* QAM. For instance, if the sampling rate of 50 Gs/s (or Giga baud) and 16-QAM is used, the total bit rate is 200 Gb/s (4 × 50).

In general, a good communication performance requires high computations and hardware resources. In an optical communication channel, there are impairments owing to physical media limitation, where impact is increased at high data rates. These impairments include chromatic dispersion (CD) and polarization mode dispersion (PMD). Furthermore, the higher bit/Hz, the higher the sensitivity to phase and amplitude offsets. These impacts are significant at higher speeds (or high sampling rates). CD and PMD cause optical signal dispersion. The dispersion causes

optical pulses to overlap and combine [3]. Then, intersymbol interference (ISI) occurs. Consequently, the signal error will be increased and the dispersion limits the communication speed [3].

QPSK and *M-ary* QAM are generally first operated on single carrier (SC) (or single radio frequency (RF)) communication systems, which implies that the digital bit information is transmitted on one frequency. However, SC communication tolerates less ISI [4] compared to multi-carriers such as the orthogonal frequency division multiplexing (OFDM) communication system. Therefore, OFDM is very attractive to use. OFDM is a multi-carrier communication system, in which each subcarrier transmits some data that maps the bit information streaming to QPSK or *M-ary* QAM. OFDM was first used successfully in wireless communication to combat dispersion (or multi-paths) communication channels [25, 26, 32, 48].

Because of the advantages of OFDM, which is for high speed wireless communication, it has been adapted for optical communication within the last half decade, thereby neglecting ISI for optical communication [4-18]. OFDM can be used for both optical coherent detection [4-14] and direct detection [15-18]. However, in this dissertation coherent detection is considered, which is called coherent optical orthogonal frequency division multiplexing (CO-OFDM).

However, in this work, self-homodyne is used for experimental measurement. For full coherent detection as well as multiple input multiple output (MIMO) detection, those can be found in [5-6]. This is a very complicated and challenging. The present work can gain its proper value only when also these other problems have been solved and CO-OFDM can be put into practical systems.

In addition, OFDM is one of the advanced modulation format for optical communication system, which can solve linear optical dispersion impairments by adding the cyclic prefix (CP) to the head of each OFDM symbol. The basic idea of OFDM transmission is to divide the available spectrum bandwidth into multiple frequencies called subcarriers, where each subcarrier is orthogonal to each other. To make the subchannels orthogonal, a discrete inverse Fourier transform (DIFT) is used as a modulator, while a discrete Fourier transform (DFT) is used as the demodulator. Thus, if the number of subcarriers is sufficient, the bandwidth per subcarrier will be very narrow compared to the coherence bandwidth of the whole total spectrum bandwidth, which is equal to that of SC communication systems. Then, the channel

impulse response in each subcarrier can be approximately flat. Therefore, the channel effects would be less than those of a single carrier system.

However, the OFDM transmission system is sensitive to phase mismatch and rotation, such as that caused by carrier frequency offset (CFO), sampling clock frequency offset (SCFO), and IQ component mismatch [20, 21]. Therefore, the compensation and equalization at the receiver part are necessary. In addition, a DFT window and CFO are also necessary for synchronization in order to demodulate the received signal back correctly. Otherwise, phase rotation will occur and cause ICI directly.

1.2 Motivation and contribution

To make OFDM work properly at the receiver part, there are some preprocesses that must be considered. This thesis considered only the areas of primary importance: the OFDM frame synchronization, the radio frequency synchronization between the transmitter and receiver, and the channel estimation and compensation to recover both the phase and amplitude, as shown in the yellow and blue units in Figure 1.1. The Figure is described in detail in the next chapter.

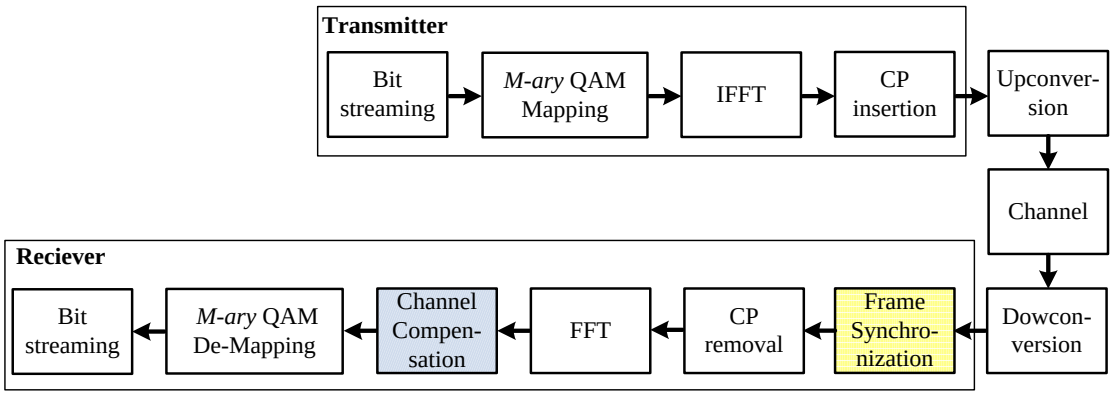

Figure 1.1. A general OFDM communication system.

This dissertation proposes new methods for OFDM frame synchronization to correctly obtain the FFT window, which is one of the most important processes for OFDM to function properly. All the widely used methods are from Schmidl and Cox [4-9, 50]. They proposed one special complete OFDM symbol, which is used as the

training sequence (TS), and split it into two halves, both of which are identical in time domain. In the receiver part, the starting point of the OFDM frame is found by calculating the correlation peak of the received signal (first part of the TS) with the delayed version of the received signal (second part of the TS). In addition, this method also has low tolerance to noise and optical channel effects [13]. Therefore, to overcome these problems, a shorter TS having high tolerance to noise and optical channel effects is proposed and will be discussed in chapter 3.

The CFO is an important problem that affects system performance and occurs if the two frequencies of the transmitter and receiver (local oscillator) do not match exactly. As a result, the OFDM spectrum band shifts and ICI occurs. CFO is divided into two parts: one is integer and the other is fractional. Schmidl and Cox [50] proposed CFO estimation in time domain by calculating the phase angle of the two halves of the TS symbol. Moose method [55] proposed that the CFO is estimated in the frequency domain by calculating the phase angle of the two identical TS symbols. Unfortunately, these two methods can handle only the fractional CFO part and the maximum estimation range is only a half of subcarrier frequency spacing. Recently, S. Cao proposed a wide range CFO compensation by combining Schmidl and Cox method and RF-pilot-based method [56]. The integer part was estimated by counting the number of FFT bin*th* index where the RF-pilot peak is located and the fractional part was estimated by Schmidl and Cox method. For this, one TS symbol and one RF-pilot tone were used, which reduced OFDM frame efficiency. Thus, the two steps RF-pilot is proposed in this thesis. Only one RF-pilot is needed, which covers all the estimated range of CFO. The proposed method does not need TS symbol, unlike that needed in S. Cao method [56], because the RF-pilot tone is inserted to every OFDM symbol.

Focusing on channel compensation, the CD and phase noise (PN) effects are neutralized in the frequency domain, which is the blue unit seen in Figure 1.1. The unit is called one-tap equalization. For PN, the widely used methods are RF-pilot [5-7] and common phase error (CPE) [8-10]. For CD compensation, several pilot OFDM symbols are used to extract the CD coefficient in the following step. To complete all the optical channel compensation, many OFDM symbols are consumed. This causes a loss of communication bandwidth. Thus, this dissertation proposes both CD and PN compensations simultaneously by distributed insertion of the known pilot into every

OFDM symbol. At the receiver part, the optical channel impairment and the PN are acquired from the pilot data and are then interpolated between the adjacent channel coefficients (CCs) to obtain all the CC for data recovery. Compared to the CPE method, the proposed method has higher throughput and is less complex to implement, while the system performance is maintained or even improved.

In addition, CO-OFDM combats channel dispersion by adding CP to the head of the symbol. If the CP is chosen to be longer than the channel impulse response, ISI can be neglected. However, for long-haul communication, the accumulated CD becomes very large. Therefore, a large CP is required to neglect ISI, and these additional samples reduce the effective data rate. In addition, the laser PN can become a serious problem. To overcome this problem, this work also demonstrates CP-free CO-OFDM. Sang-Yuep Kim [22], Chen Chen [23], and Liang B. Du [24] proposed precompensation for CD before it is demodulated by the DFT unit. It contains a feedback loop and precompensation to modulate the received signal by the FFT unit. To combat ISI, each OFDM symbol is windowed with an exponential decay window at either side of each OFDM symbol in time domain. The various types of windowing are also investigated and compared. However, the proposed and validated method contains no feedback loop and no CD precompensation.

Finally, a high performance comes with high complexity to implement or impossibility to implement the hardware because of the limitations of the current technology. Therefore, this dissertation proposes very high efficiency algorithms and methods for implementation in terms of hardware that meets the system performance needs.

1.3 Thesis organization

Chapter 2 presents the basic theory of the CO-OFDM communication system. First, this provides the details of the OFDM modulation technique, which includes the benefits of appending CP to neglect ISI and zero padding for oversampling. Next, the details of the optical coherent communication detection, which includes balanced detectors and phase diversity detectors, are discussed. Then, the optical channel effects, such as CD, PMD, and amplified spontaneous emission (ASE), are detailed. Finally, the RF impairments, including phase noise, are given. To

meet the system performance, the system parameters such as FFT size, the number of CP samples, the calculation of the bandwidth requirement, the subcarrier frequency spacing, and the bit rate are defined.

Chapter 3 will discuss one of the important processes in the CO-OFDM communication system: the FFT window synchronization. It is split into two main sections: the first section will provide literature reviews of the conventional methods and the second section will provide the proposed method. The results are confirmed by simulation and experimental methods. In the second section, frequency synchronization will be discussed. This section will present the impact of the CFO impairments and discuss the conventional compensation methods. Finally, the proposed compensation method will be given.

Chapter 4 will detail another important unit, which is the demodulation and data recovery back process. This chapter contains two main topics. First, the impact of OFDM phase rotations owing to optical channel impairment, which is discussed in separate sections for CD and PN, is discussed. Then, to cancel those effects, the channel estimation and compensation follow in the next module. Second, the CP reduces the effective bit rate of the communication system. In particular, for long haul communication, the necessary CP length becomes very large in order to eliminate ISI. Thus, to increase the bit rate efficiency, the CP-free OFDM symbol that increases the communication speed is studied.

Chapter 5 will provide the conclusions and future work.

CHAPTER 2

Principle of Coherent Optical OFDM

2.1 Introduction

To clearly understand the proposed work in this dissertation, this chapter will provide all the basic theories of coherent optical orthogonal frequency division multiplexing (CO-OFDM) communication systems. Firstly, the basic idea of the OFDM modulation technique will be discussed. It is the modulation format with the best tolerance to the dispersive channel (or the "fading channel" or "multi-paths channel" in wireless communication systems). This will be discussed in Section 2.2. Next, in Section 2.3, the principle of coherent optical communication both for transmission and detection will be given, such as homodyne and heterodyne schemes, which have the greatest flexibility and high sensitivity detection.

Then, topics concerning the optical channel including chromatic dispersion (CD), polarization-mode dispersion (PMD) and amplified spontaneous emission (ASE) noise are discussed in Section 2.4. Phase noise (PN) to the non-ideal laser diode that does not generate only one frequency but rather generates many frequencies differing by some kHz or MHz will be detailed in the following section.

Finally, to meet the system performance requirements and make the system implementable, some system parameters have to be considered and carefully selected; for example, the number of subcarriers, length of the cyclic prefix (CP) (called guard time), sampling frequency, bit rate, and spectrum bandwidth. All these parameters will be discussed in Section 2.5.

2.2 Basic OFDM modulation technique

This section will provide details about how the OFDM modulation works for optical commutation systems. The advantages, disadvantages and some useful schemes to eliminate intersymbol interference (ISI) and inter-carrier interference (ICI) will also be discussed.

2.2.1 Overview of OFDM

The key concept of OFDM signal is a modulation method in which the digital information is modulated onto a multi-frequency scheme in parallel. This is called multi-carriers. Each subcarrier has a lower frequency when compared to the main carrier while the single carrier (SC) uses only one carrier. Then, all the multi-carriers are summarized and transmitted out, as shown in Figure 2.1. All subcarriers are orthogonal to each other.

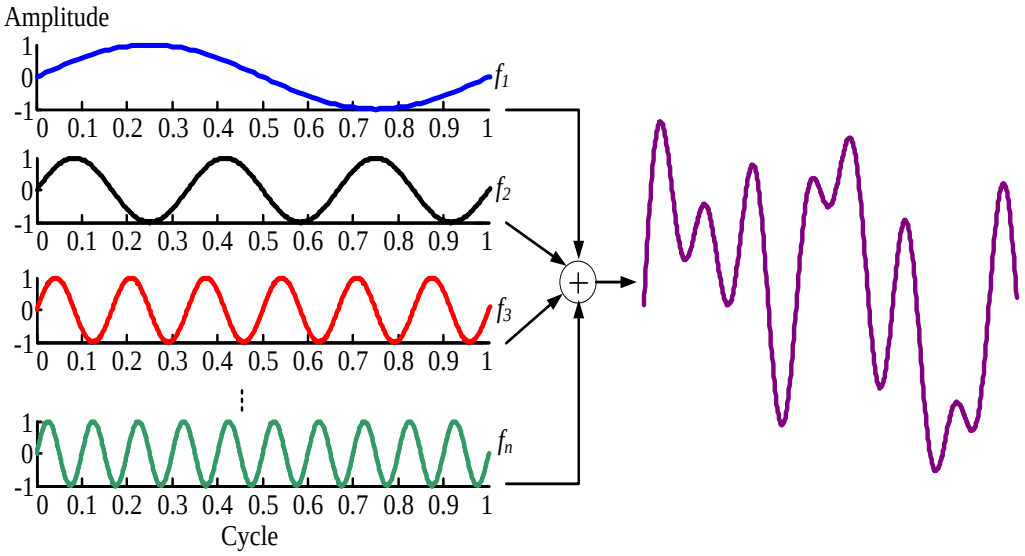

Figure 2.1. Principle of the multi-carrier modulation system.

In general, each carrier is called subcarrier. Compare to SC communication systems, OFDM would be more robust to dispersive channel effects [26, 32, 48].. Furthermore, the OFDM overcomes ISI problems by adding some parts of its data sample to the head of the OFDM symbol. This is called the cyclic prefix extension [25-27, 31] which will be discussed in more detail in the next section.

In addition, the OFDM is similar to conventional frequency division multiplexing (FDM), but it uses the frequency band for modulation systems more efficiently than FDM. To make it efficient, in each subcarrier, the central or maximum peak of each spectrum has to cross the zero spectrum power of the neighbor subcarrier, as shown in Figure 2.2. To implement this condition, the inverse fast Fourier transform (IFFT) can be applied, which is expressed in Equation (2.1). Therefore, there is no cross-talk between the subcarriers, and the frequency spectrum

can be shifted to the left and overlapped with the neighbors, which is called the orthogonal phenomenon. Thus, in contrast to the conventional FDM, a guard band frequency is not required, as shown in the comparison between Figures 2.2 and 2.3.

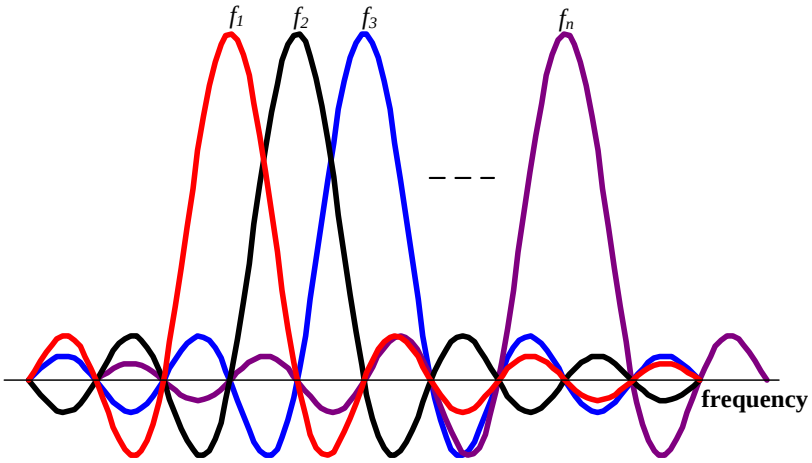

Figure 2.2. An example of using spectrum band for the OFDM.

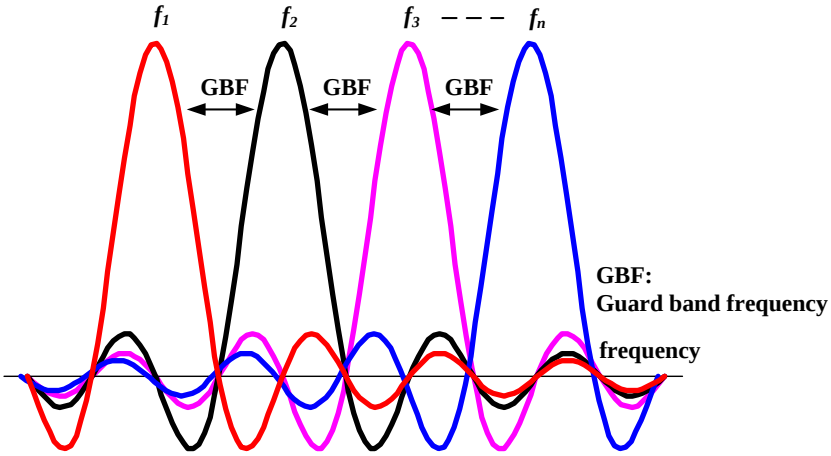

Figure 2.3. An example of using spectrum band for the conventional FDM.

Figures 2.2 and 2.3 compare the use of spectrum band for the OFDM and the conventional FDM communication system. It shows that OFDM need not GBF unlike FDM. This means that OFDM saves a lot of bandwidth.

2.2.2 OFDM transceiver

The details of the OFDM transmitter and receiver architecture are provided. The schematic of the transmitter part is illustrated in Figure 2.4.

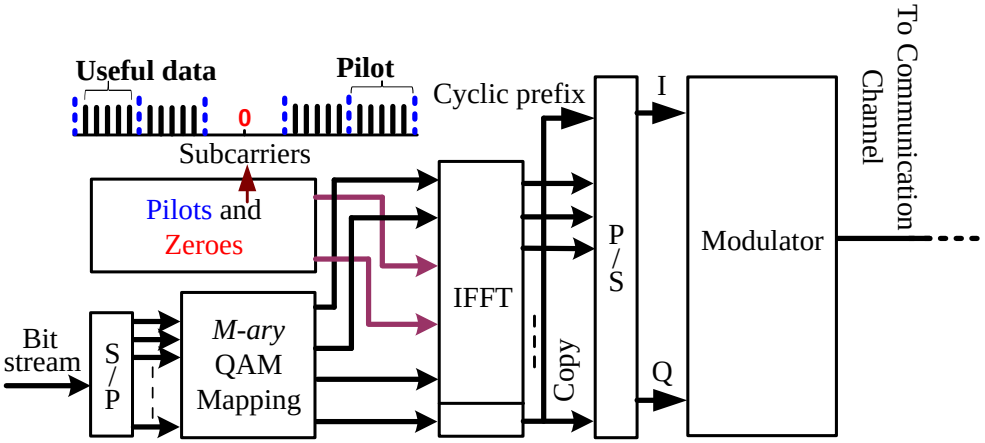

Figure 2.4. A basic configuration of the OFDM transmitter.

The high speed serial bit streaming is converted to a parallel slow data stream and then mapped into constellation points in the complex plane, for example, using binary phase-shift keying (BPSK), quadrature phase-shift keying (QPSK) or quadrature amplitude modulation (QAM). Usually, *M-ary* QAM is used. For constellation mapping and de-mapping, see appendix A. Then, all the constellation points are fed into an inverse fast Fourier transform (IFFT) block to convert the mapped constellation to the time domain. Some pilot data and zeros, which are used for channel estimation and oversampling (anti-aliasing), respectively, are inserted. The zeros are inserted into the subcarrier around the middle of the IFFT input unit. Finally, a CP is added and then all these data, which also include useful data, are converted to the radio frequency (RF) domain or the optical domain for optical communication. The schematic of the transmitter is shown in Figure 2.4.

At the receiver part, after demodulation (or the conversion from the optical domain to the base band signal), the received OFDM symbol sample signal, which is sampled using analog to digital converter (ADC), is converted from serial to parallel. Next, the CP part is removed and fed with the useful data into the FFT block to convert back from the time domain to frequency domain. To compensate for channel communication impairments, the channel impulse response (CIR) must be known. In general, to obtain the CIR for data recovery, a pilot-aided algorithm that transmits known data from the transmitter is used. Finally, the information data are de-mapped from the constellation point to obtain bit streaming before back conversion to serial data. The schematic of the receiver is shown in Figure 2.5.

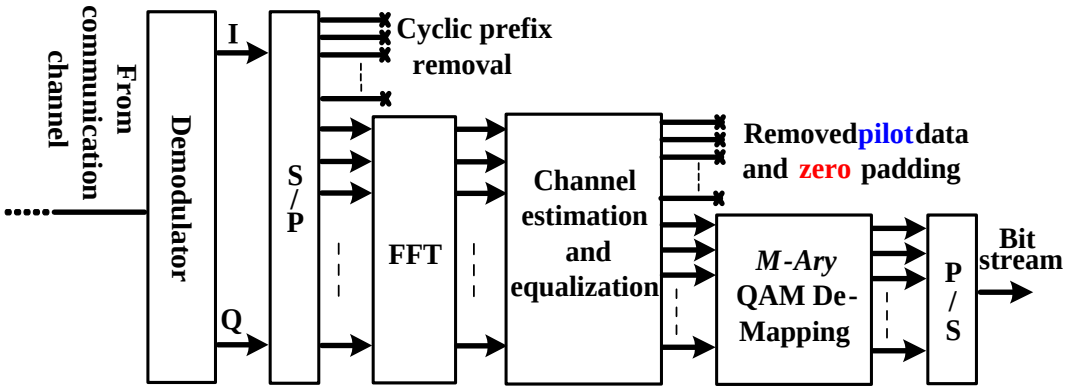

Figure 2.5. A basic configuration of the ODFM receiver.

Given the property of the discrete Fourier transform (DFT) of a sinusoidal signal, the spectra in all the subcarriers (sub-frequencies) are always orthogonal [28]. In addition, the DFT is computed by the FFT algorithm, which is a faster calculation. Thus, the OFDM modulation is very efficient for computing the orthogonal subcarriers.

Therefore, to model the OFDM signal, the definition of the IFFT should be firstly provided as expressed by [29-30]:

$$x(n) = \frac{1}{N_C} \sum_{k=0}^{N_C-1} X(k) e^{j2\pi kn/N_C}, \quad n = 0,1,2,..., N_C - 1, \tag{2.1}$$

and the definition for FFT is as follows:

$$X(k) = \sum_{n=0}^{N_C-1} x(n) e^{-j2\pi kn/N_C}, \quad k = 0,1,2,..., N_C - 1, \tag{2.2}$$

where N_C is the number of IFFT/FFT-points which must be a power of two, n is the discrete sample index, and k is the frequency bin index. Thus, we slightly change $X(k)$ to be d_k, and $f_k = k/(N_C T_s)$, which is called the frequency spacing [31].

$$t = nT_s, \tag{2.3}$$

is the time of the *n*th sample with a sampling rate of T_s. Then, Equation (2.1) can be rewritten as follows:

$$S(t) = \frac{1}{N_C} \sum_{k=0}^{N-1} d_k e^{j2\pi f_k t}, \tag{2.4}$$

where $S(t)$ is the OFDM signal in time domain. Finally, the OFDM transmitter signal can be described in terms of infinite transmission time by [8, 32]:

$$S(t) = \sum_{l=-\infty}^{\infty} \sum_{k=0}^{N_C-1} d(k,l) e^{j2\pi f_k t} \Pi(t - lT), \tag{2.5}$$

where $\Pi(t) = \begin{cases} 1, 0 \le t \le T \\ 0, elsewhere \end{cases}$ represents the unit rectangular function and T is the symbol duration . For simplicity, the CP data are not considered here.

Thus, $d(k,l)$ is the constellation data to be transmitted, which are complex numbers mapped into QPSK or QAM modulation. The index *l* represents the time dependence of a symbol and *k* is a subcarrier index. For example, with QPSK (or 4-QAM), the constellations on the complex plane are $\{1+1j, 1-1j, -1+1j, -1-1j\}$. Thus, the outputs of IFFT/FFT are also complex numbers [14]. Furthermore, in this case, the number of transmitted bits is 2 for QPSK.

OFDM has many advantages compared to single carrier systems. Firstly, the oversampling can be done easily by adding some zeros to the subcarrier around the middle of the IFFT input block. This is called zero padding. However, some useful subcarriers to transmit zeros instead of data are lost. Hence, an oversampling factor of 1.2 can be achieved by zero padding of 20% of all IFFT-points [4]. Secondly, because the frequency band is split into many lower subcarrier frequencies, each subcarrier has a longer impulse response. However, all the subcarriers are required to be frequency independent and orthogonal. Therefore, the channel effects will not affect the OFDM symbols much if we can maintain the orthogonality of each subcarrier with no ICI. Next, the channel compensation can be performed in the frequency domain with a one-tap equalizer, which is simple and easy. Finally, ISI can be

eliminated by the CP extension [25-26]. ICI and ISI will be discussed in the next section.

The disadvantage of OFDM is that it is very sensitive to phase and frequency error because it makes the carrier signals in each subcarrier no longer orthogonal [5, 12, 55]. In particular, when high or multi-level QAM constellation mapping is employed to each subcarrier, it would be more sensitive to the phase offset. Thus, ICI occurs and it makes the signal power of each subcarrier leak to the neighbor subcarriers. Furthermore, the peak to average power ratio (PAR) should be considered when the FFT size is increased [37]. In addition, the OFDM communication system needs to know where the FFT window is located. If it is misaligned or shifted, the phases are rotated. More details will be discussed in the next chapter.

2.2.3 Zeros padding

In the OFDM modulation system, oversampling (by increasing the sampling frequency at the receiver side) is very important because it gives a greater resolution of the signal information in the time domain. Oversampling can be simply performed by two places. One is done at the receiver end by increasing the clock frequency of the analog to digital converter (ADC). However, there is a simpler way, which is also another advantage of OFDM; the oversampling can be conducted at the transmitter part by insertion of zeros into the subcarrier around the middle of the IFFT unit. The insertion scheme is shown in inset A of Figure 2.6, called zeros padding [32].

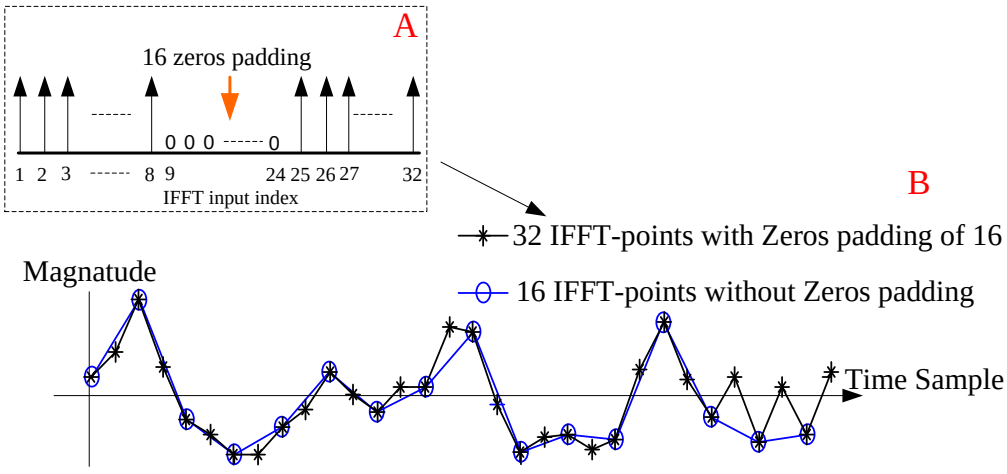

Figure 2.6. Oversampling the OFDM signal by zero padding.

Inset B in Figure 2.6 is an example output of an IFFT unit with and without oversampling. The blue represents the output of 16 IFFT-point where there is no zero padding and the black line represents the output of 32 IFFT-point, such that 16 zeros are inserted into the middle of the IFFT unit. It is clear that the oversampling ratio is 2 and that it gives a higher resolution in the time domain, which is very useful for sampling the received signal at the receiver side.

The two methods are oversampling and both shift out the alias components away from the OFDM signal. The distinction is that in one case oversampling is in the ADC whereas in the other it is in the DAC, and that one of them the input signals is in the time domain whereas in the other it is in the frequency domain.

2.2.4 Cyclic prefix

The cyclic prefix (CP) is very useful to eliminate ISI and maintain subcarrier orthogonality properly. Every OFDM symbol is preceded by a CP, which is taken from some of the sample data information itself. Therefore, the total OFDM symbol becomes longer as given below [25, 32]:

$$N_{sym} = N_C + N_{CP}, \tag{2.6}$$

where N_{sym} is the total length of one complete OFDM symbol, N_C is the number of subcarriers, and N_{CP} is the CP length, generally measured in sample unit, as shown in more detail in Figure 2.7. Thus, the CP is the redundancy data and it degrades the communication speed (bit rate).

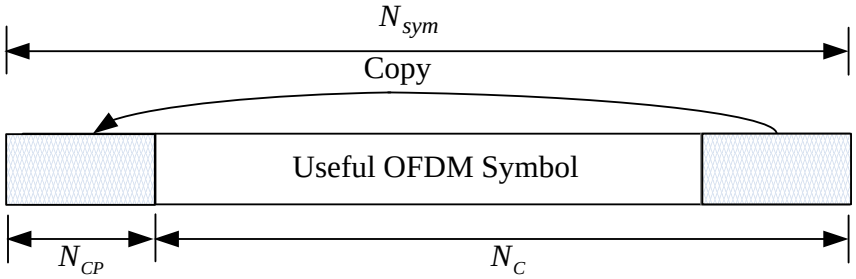

Figure 2.7. Cyclic prefix insertion scheme.

In general, the CP precedes the head of each OFDM symbol, and the length of CP is normally $N_C/8$. Figure 2.8 shows the advantage of applying the CP to OFDM

symbol. As can be seen, after the OFDM symbol $x(t)$ is passed through a dispersive optical channel (CD and PMD) denoted by $h(t)$, it overlaps with the neighbor OFDM symbols, and then ISI occurs when the CP is not applied or insufficient. On the other side, when the CP is applied and is longer than the channel impulse response in the time domain, ISI still occurs but it will be discarded at the receiver. Therefore, only the effective part (useful sample) remains and ISI can be neglected in this situation.

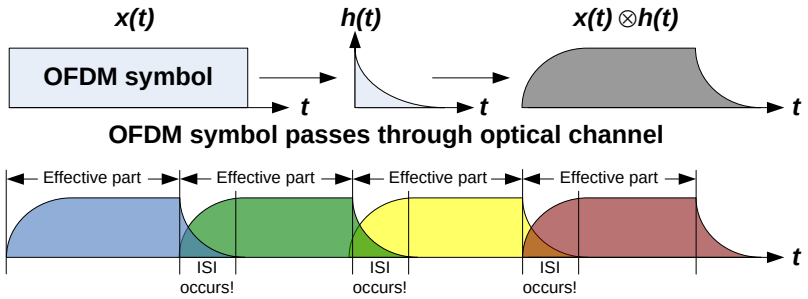

A. An example of the received OFDM symbol (ISI occurs) at the receiver part when CP is not applied (or the CP is not long enough).

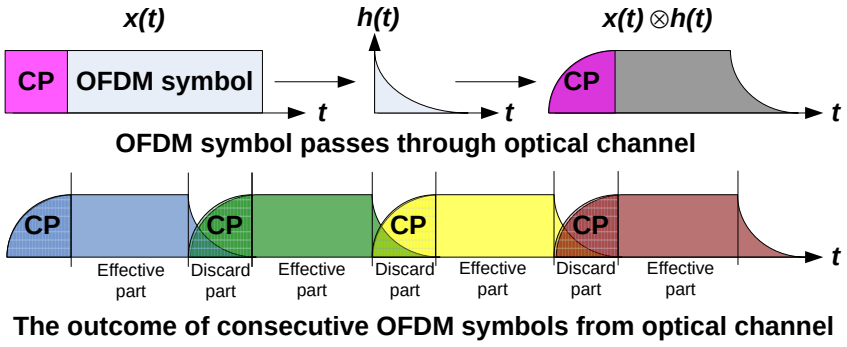

B. An example of the received OFDM symbol (ISI can be neglected) at the receiver part when CP is applied (or the CP is long enough).

Figure 2.8. Benefit of using CP [33].

In addition, the CP is advantageous in terms of FFT window synchronization to demodulate the received signal. It can be used for OFDM symbol synchronization, which will be given in detail in the next chapter. Moreover, the starting point of the FFT window can be anywhere within the CP region to guarantee that the subcarrier orthogonality is still maintained and there is no ICI, but the phase is shifted.

However, if the length of CP is sufficient, ISI can be ignored, but the ICI could still occur owing to the carrier frequency effect (CFO) and the random phase noise (PN) effects. Thus, ICI is not prevented. These effects will be discussed in the next chapter.

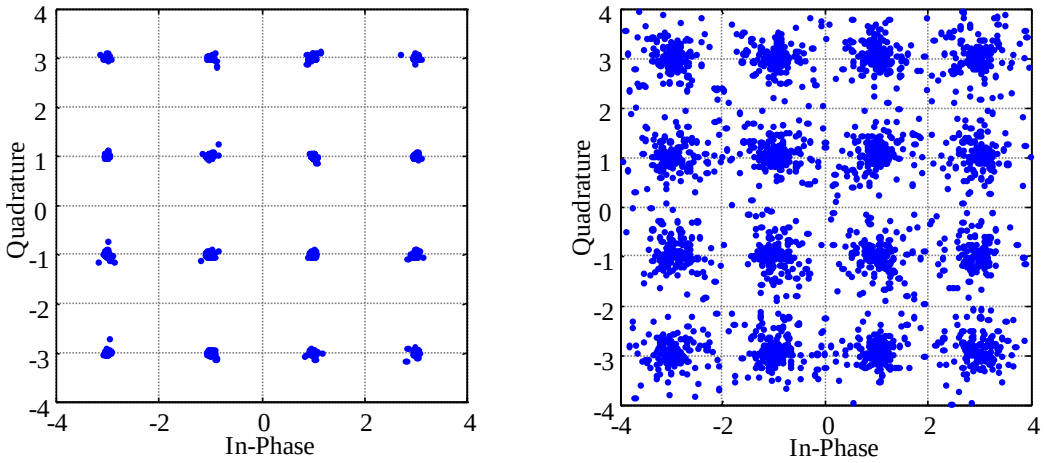

A: CIR are less than the CP length. **B:** CIR are more than the CP length.

Figure 2.9. Impact comparison of the CP length with channel effect taps length.

Figure 2.9A shows an example result of a 16-QAM constellation diagram where the channel impulse response (CIR) is less than the CP length, while the case where the CIR is larger than the CP length is presented in Figure 2.9B. These diagrams were simulated with a FFT size of 256, a CP length of 32 samples (256/8), and an optical signal to noise ratio (OSNR) of 30 dB. The results show that if the CP is shorter than the CIR length, ISI will occur. Therefore, the constellation is distributed because the phase and amplitude are distorted. The constellation is correct and not distributed over the whole complex plane when the CIR is equal to (or less than) the CP length. Therefore, it is confirmed that the CP length has to be selected to be longer than channel taps. Otherwise, the ISI will occur and degrade the system performance.

2.3 Coherent optical OFDM

This section begins with the basic concept of coherent optical communication systems (COCS) and continues with operating COCS with OFDM. COCS have many advantages. For instance, coherent detection allows the reception of amplitude and phase information. Consequently, highly spectrum efficient modulation formats, such

as QPSK and 16-QAM, can be applied. The receiver sensitivity of the coherent detection is higher than direct detection [3, 34-35]. In particular, over the last decade, channel estimation and compensation have been performed in the electrical domain by using digital signal processing (DSP) which is more efficient. Therefore, coherent detection is very attractive for multi-gigabit and long-haul optical communication systems including coherent optical OFDM communication systems.

2.3.1 Coherent optical OFDM transmitter

For the transmitter, there are two modes of up-conversions from the electrical domain to the optical domain: direct and indirect up-conversions [11]. However, for simplicity, in this thesis, only the direct up-conversion will be analyzed. Thus, for the coherent optical OFDM transmitter (Tx), nested Mach-Zehnder modulators (MZM) are used to up-convert the electrical OFDM signal into the optical domain, as shown in Figure 2.10. For more details on MZMs and optical modulation, please see Appendix A.

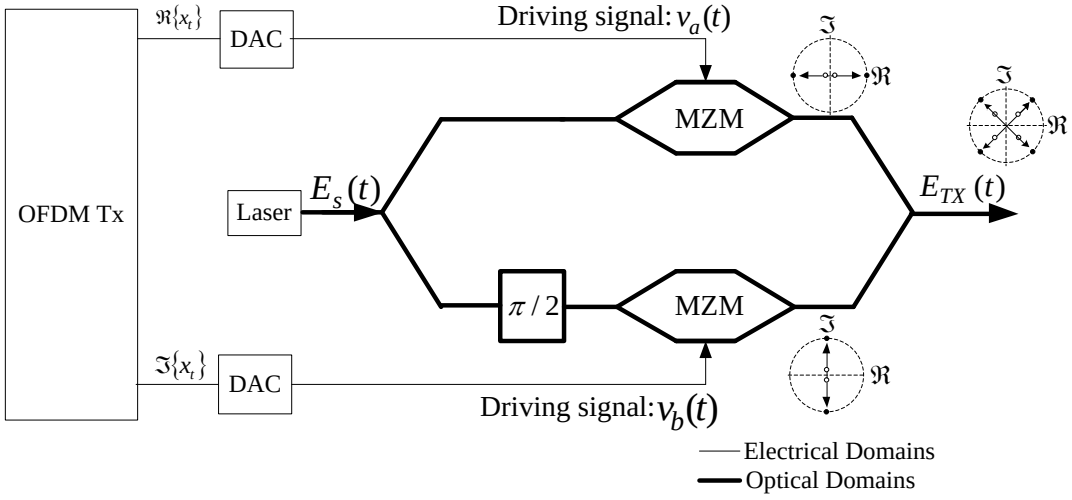

Figure 2.10. General configuration of the coherent optical OFDM transmitter.

In Figure 2.10, the unit OFDM Tx (or digital signal processing: DSP) is the digital domain which can be implemented either by an application-specific integrated circuit (ASIC) or field programmable gate array (FPGA). The digital outputs for real part $\Re$ (inphase) and imaginary part $\Im$ (quadrature) of $x(t)$ are converted into analog

signals $v_a(t)$ and $v_b(t)$ by separately two DACs. Then, $v_a(t)$ and $v_b(t)$ are modulated onto the optical carrier $E_s(t)$ with the frequency $\omega_S/2\pi$ and $E_s(t)=\sqrt{2P_s}e^{j(\omega_s t+\varphi_s(t))}$ with the power $P_s=(1/2)|E_s|^2$, and $\varphi_s(t)$ is a random laser phase fluctuation [36]. . The signal in the lower path is delayed by an additional angle of 90°, and the transmitted optical OFDM signal E_{TX} is determined by [73]

$$E_{TX}(t)=E_S(t)\left(\frac{1}{2}\cos\left(\frac{v_a(t)}{2V_\pi}\pi\right)+j\frac{1}{2}\cos\left(\frac{v_b(t)}{2V_\pi}\pi\right)\right). \tag{2.8}$$

As shown in Equation (2.8), the optical coherent transmitter is very flexible because the signal can be modulated in two quadratures or by amplitude and phase. Consequently, the OFDM signal can be generated and transmitted out to optical fiber.

2.3.2 Coherent optical OFDM receivers

In this section, two receiver architectures will be described. Firstly, the fundamental technique, the balanced detector, is shown. The other more sophisticated architecture is the optical 90° hybrid which can recover the I- and Q-component of the received signal. These architectures are shown in Figures 2.11 and 2.12, respectively.

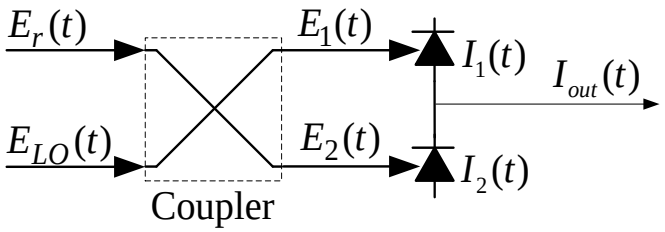

Figure 2.11. Optical coherent balanced detector.

Figure 2.11 shows the balanced detector setup. The received signal $E_r(t)$ and the local oscillator (LO) signal $E_{LO}(t)$ are fed into the two inputs of an optical coupler.

For the sake of simplicity, the received signal is assumed to be corrupted only by noise and not by channel dispersion. The received signal is denoted by

$E_r(t) = E_{TX}(t) + \tilde{n}(t)$, where $E_{TX}(t)$ is the transmitted signal as discussed in the previous section and $\tilde{n}(t)$ is the noise signal. The photocurrents are $I_1(t) = \frac{1}{2} R|E_1(t)|^2$ and $I_2(t) = \frac{1}{2} R|E_2(t)|^2$, where R is the photo diode responsivity and $E_1(t)$ and $E_2(t)$ are the sum and the difference of the electric fields, respectively, given by [35-36] as follows:

$$E_1(t) = \frac{1}{\sqrt{2}}[E_r(t) - jE_{LO}], \tag{2.9}$$

$$E_2(t) = \frac{1}{\sqrt{2}}[-jE_r(t) + E_{LO}]. \tag{2.10}$$

The optical powers at the photo-receiver inputs are P_1 and P_2, which are expressed by

$$P_{1,2} = \frac{1}{4}(|E_r|^2 \pm 2\Re(jE_{LO}^* E_r) + |E_{LO}|^2). \tag{2.11}$$

Finally, the output of the balanced detector $I_{out}(t)$ can be described as follows [35]:

$$\begin{aligned} I_{out}(t) &= R(P_1 - P_2) = R\Re(E_{LO}^* E_r e^{j\omega_{IF}t}) \\ &= -2R\sqrt{P_r P_{LO}} \frac{|E_{LO}^* E_r|}{|E_{LO}||E_r|} \sin(\omega_{IF} t + \theta(t)), \end{aligned} \tag{2.12}$$

where $R = e\eta / h\omega_s$ is the detector responsivity, e is the electron charge, η is the quantum efficiency of the photodiode, and h is Planck's constant. Additionally, $\omega_{IF} = (\omega_s - \omega_{LO})$ is the angular intermediate frequency (IF) where ω_s is the signal carrier angular frequency and ω_{LO} is the local oscillator angular frequency. The case where $\omega_s = \omega_{LO}$, $\omega_{IF} = 0$ and $\theta(t)$ is either $\pi/2$ or $3\pi/2$ is called the "*Homodyne Receiver*" and when $\omega_s \neq \omega_{LO}$ and $\omega_{IF} \neq 0$ is called the "*Heterodyne Receiver*." The variable $\theta(t)$ is the phase difference between the recovered signal and the local

oscillator signal. Variables P_r and P_{Lo} are the received optical power and the local oscillator power, respectively. Hence, if the polarizations of signal and LO are identical, $\left|E_{LO}^{*}E_r\right| \Big/ \left(\left|E_{LO}\right|\left|E_r\right|\right)$ is equal to one [35], which is assumed throughout this dissertation hereafter.

In practice, the local oscillator power P_{Lo} is constant and greater than P_r. Therefore, the gain of the received signal and sensitivity increases. It can be proved that the sensitivity of coherent detection is better than that of direct detection, which is also a great advantage [3, 4].

However, the signal cannot be demodulated separately by real and imaginary parts which are necessary for QPSK, various QAM formats, and OFDM. Therefore, a more sophisticated technique has to be considered. In this thesis, an optical 90^0 hybrid demodulator is used as shown in Figure 2.12.

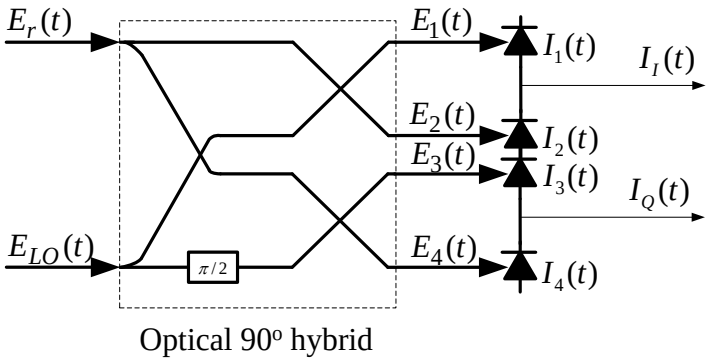

Figure 2.12. Optical coherent demodulator by using the optical 90° hybrid.

The 90° hybrid combines the received signal and the LO signal to generate four states in quadratures in the complex-field space. Then, the four signals are fed into two pairs of balanced photodetectors. The complete transfer function of optical 90^0 hybrids is given by [37]

$$H_{hb} = \frac{1}{2}\begin{bmatrix} 1 & 1 \\ 1 & -1 \\ 1 & j \\ 1 & -j \end{bmatrix}, \tag{2.13}$$

and the output of the optical 90^0 hybrid is as follows:

$$\begin{bmatrix} E_1 \\ E_2 \\ E_3 \\ E_4 \end{bmatrix} = \frac{1}{2}\begin{bmatrix} (E_S + E_{LO}) \\ (E_S - E_{LO}) \\ (E_S + jE_{LO}) \\ (E_S - jE_{LO}) \end{bmatrix}. \tag{2.14}$$

Finally, the output photocurrents from the balanced photodetectors are expressed as [34]

$$I_I(t) = I_1(t) - I_2(t) = R\sqrt{P_S P_{LO}}\cos(\omega_{IF}t + \theta(t)), \tag{2.15}$$

$$I_Q(t) = I_3(t) - I_4(t) = R\sqrt{P_S P_{LO}}\sin(\omega_{IF}t + \theta(t)), \tag{2.16}$$

and by combining Equations (2.19) and (2.20), a complex signal can be derived as follows:

$$I(t) = I_I(t) + jI_Q(t) = R\sqrt{P_S(t)P_{LO}(t)}e^{j(\omega_{IF}t+\theta(t))}. \tag{2.17}$$

2.4 Impairments owned by optical channel

This section discusses the linear effects which occur in real-world optical communication systems and cannot be avoided. However, they can be compensated for. The main causes of linear distortions of the signal are chromatic dispersion (CD) and polarization mode dispersion (PMD), which will be discussed in the following section.

2.4.1 Chromatic dispersion

Chromatic dispersion (CD) means that the group delay of a signal depends on the wavelength λ. Thus, a non-monochromatic signal is distorted because it consists of different spectral components which travel at different velocities and result in pulse

broadening, denoted by $\Delta\tau$, unless an appropriate chirp (e.g., squared phase) is used, as shown in Figure 2.13. In general, the lower the λ, the faster the speed.

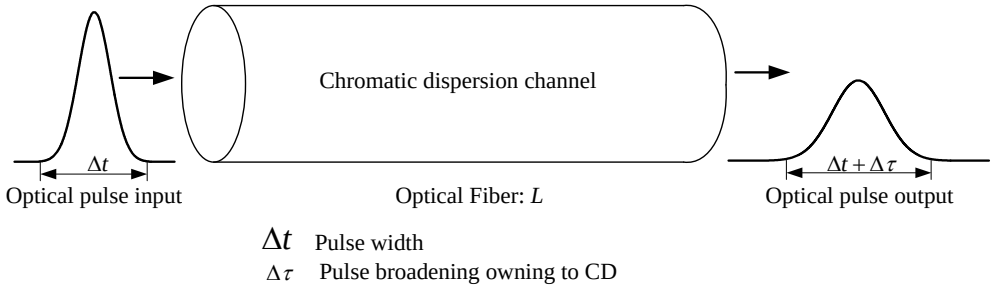

Figure 2.13. Chromatic dispersion phenomenon.

The second derivative of the phase constant β by the angular frequency is given by [35]

$$\beta_2 = -\frac{\lambda^2}{2\pi c} D, \tag{2.18}$$

where D is the CD coefficient, c is the speed of light in vacuum, and $\lambda = 1550\,nm$ for standard single mode (SSM) fiber. In general, CD is expressed as $ps/(nm \cdot km)$. In ITU-T Fiber recommendations G.653 and G.655 [38], $D = 17\,ps/(nm \cdot km)$. Additionally, the accumulated CD, which has units of *ps/nm*, is given by

$$D_{AC} = \int_0^L D\, dz, \tag{2.19}$$

where L is the length of the optical fiber in kilometers (km). Equation (2.23) shows that the greater L, the greater the accumulation of CD. Therefore, in data transmission systems, the broadened pulses overlap with each other, leading directly to ISI, as shown in Figure 2.14.

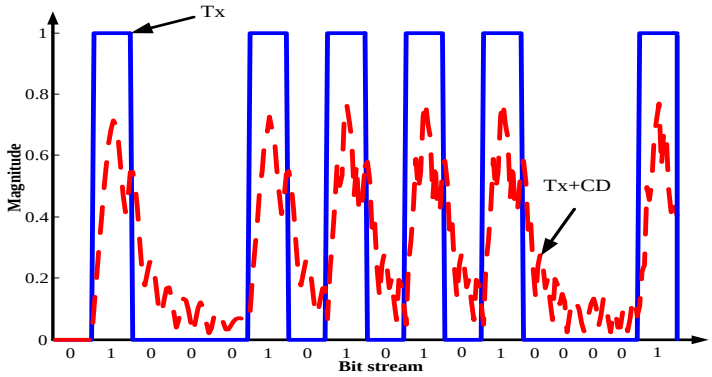

Figure 2.14. Pulse broadening owing to chromatic dispersion.

Figure 2.14 presents an example of pulse broadening after the bit streaming signal passes to the CP channel. The red dash line is broadened and the power is decreased. Tx is the transmitted bit stream and Tx + CD is the transmitted signal corrupted by CD.

2.4.2 Polarization-mode dispersion

Polarization-mode dispersion (PMD) means that the group delay of a signal depends on the state of polarization (SOP); in particular, there are two distinguished SOPs that travel at different velocities. The timing difference between them is the differential group delay (DGD, τ_{DGD}) [39-40]. PMD results from the physical geometric shape of the core (which is elliptical instead of circular), fiber torsion, bending, and thermal stress which leads to a local fiber birefringence. The total PMD in the whole fiber is the concatenation of many elementary PMDs. Because PMD is randomly distributed and changes over time due to temperature and manual movement, the total DGD is a stochastic quantity. Figure 2.15 depicts the PMD for PSPs in the x and y directions.

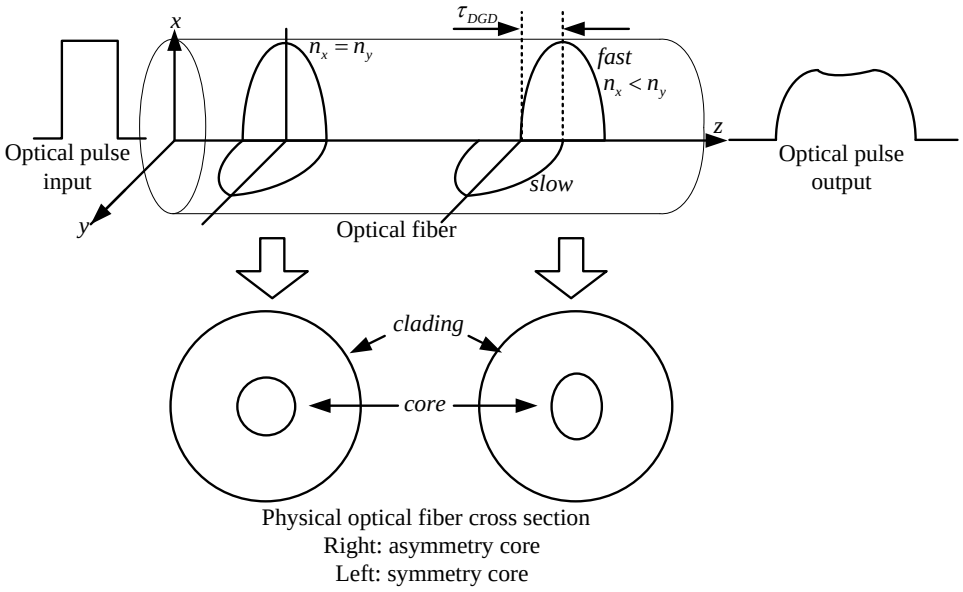

Figure 2.15. Polarization-mode dispersion phenomenon.

Figure 2.15 can be explained by simple mathematics. The speed of light in the optical fiber is $V_x = c/n_x$ and $V_y = c/n_y$ for the *x-axis* (fast speed) and *y-axis* (slow speed), respectively. Here, c is the speed of light in vacuum, and n_x and n_y are the refractive indices in the directions of the *x-axis* and *y-axis*, respectively. As shown in Figure 2.15, if n_x and n_y are different, which can be caused by elliptical core for example, then the optical input pulse is split into x and y polarizations which travel at different speeds. Finally, the optical pulse output is broadened which degrades the achievable communication speed.

2.4.3 ASE noise

In general, noise in a communication system contains many sources, such as thermal noise and shot noise in electronic circuits. However, the greatest effect on the optical communication systems is owed to amplified spontaneous emission (ASE) noise. ASE arises from the spontaneous transition of electrons from the higher to the lower energy state in the erbium doped fiber of the amplifier (EDFA) [41-42]. The EDFA is normally an amplifier that amplifies the optical signal before the signal is fed into the photo detector at the receiver side and between optical spans. However, the EDFA not only amplifies the signal but also amplifies the noise signal, as shown in Figure 2.16 below.

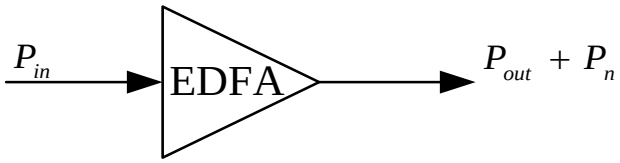

Figure 2.16. The EDFA amplifies the received signal plus its own noise.

Hence, P_{in} is the launch power input, P_{out} is the power output, and P_n is the noise power. ASE can be modeled as an Additive White Gaussian Noise (AWGN) process [42:43]. In addition, according to the previous section, the received signal with ASE noise can be re-expressed as [36]

$$E_{RX}(t) = G\,E_{TX}(t) + n(t), \tag{2.20}$$

and thus $n(t)$ is a complex Gaussian random variable with zero mean that is uncorrelated with the transmitter signal and G is the amplification gain. The quantity that indicates the quality of the optical signal is the optical signal to noise ratio (OSNR), which is generally expressed in decibels (dB) and is given by

$$OSNR = 10\log_{10}\left(\frac{S}{N}\right) \quad \text{dB.} \tag{2.21}$$

where S represents the optical signal power. N is the optical noise power, which is normally measured by multiplying the limitation of the bandwidth, B_r, with the noise power spectral density N_O. Therefore, Equation (2.21) can be rewritten as

$$OSNR = 10\log_{10}\left(\frac{S}{N_O B_r}\right) \quad \text{dB.} \tag{2.22}$$

Normally, B_r is equal to 0.1 nm (i.e., 12.5 GHz at 1550 nm).

2.4.4 Phase noise effect

In communication systems, the signal phase can be disturbed in many ways. One of them is the phase noise (PN) caused by a non-ideal laser source that cannot

generate only one exact frequency. Therefore, the result is that many different frequencies are generated which are close to the main frequency f_0 and grouped together within a certain bandwidth. The bandwidth is called the linewidth $\Delta\nu$, and it is measured at the 3 dB points below the maximum spectral power, namely the full-width at half-maximum (FWHM) [44**]** as shown in Figure 2.17.

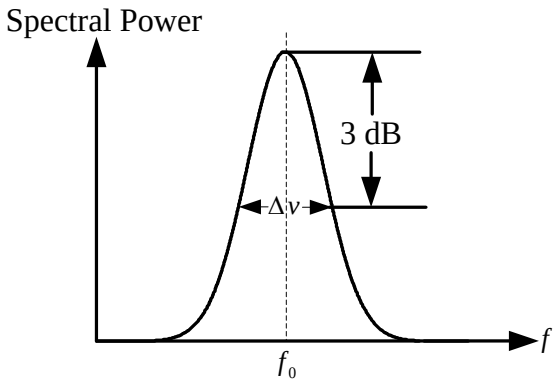

Figure 2.17. Measurement of the laser linewidth $\Delta\nu$.

The PN is modeled by the Wiener-Lévy process [36, 45], which is expressed by the random walk process, denoted by

$$\psi_n = \psi_{n-1} + \Delta\psi_n, \tag{2.23}$$

where $\Delta\psi_n$ is the Gaussian random variable with a zero mean and the variance depending on the laser linewidth. If the sampling frequency is fixed, the variance is given as

$$\sigma^2 = 2\pi\Delta\nu / f_s. \tag{2.24}$$

Hence, f_s and $\Delta\nu$ are the sampling frequency and the laser linewidth, respectively.

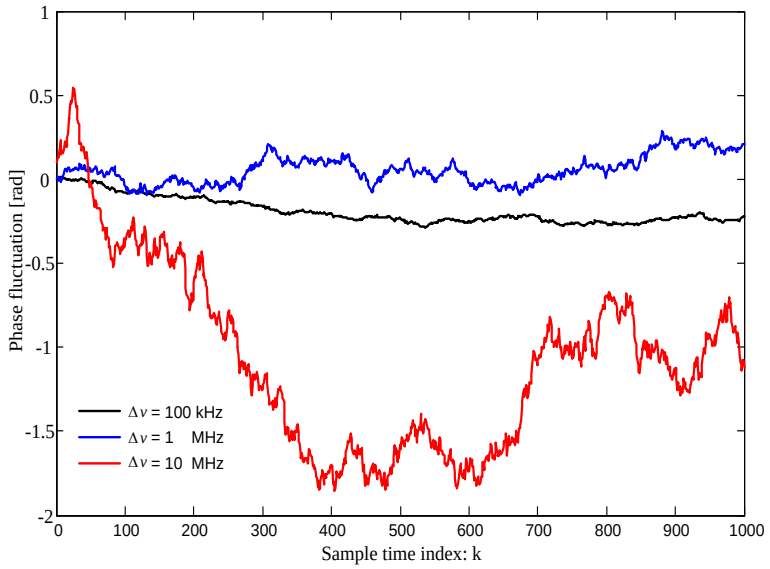

Figure 2.18. Phase fluctuation caused by various laser linewidths.

Figure 2.18 shows an example of the phase fluctuation in terms of the discrete time sample index at a sampling frequency of 2.5 GHz, where $\Delta\nu$ is set to 100 kHz, 1 MHz and 10 MHz. The greater $\Delta\nu$ induces more strongly the phase fluctuation. Thus, the phase of all the subcarriers is rotated and then ICI occurs. Therefore, the PN must be estimated and compensated. This will be discussed in the next chapter.

2.5 Design parameters

To make the system work properly, the trade-off between hardware implementation complexity and system performance requirement must be considered. Usually, good performance comes with increasing implementation complexity in any communication system as well as in the OFDM modulation technique. Therefore, in OFDM communication system, there are several parameters that should be considered to find the optimum system resources, for instance, the IFFT/FFT size, the number of CP samples (or the guard time duration) to mitigate ISI from optical pulse broadening $\Delta\tau$, the bit rate, and the channel bandwidth. However, if the IFFT/FFT size is increased, the system performance becomes more sensitive to phase noise and carrier frequency offset.

Reconnecting to CD and PMD has impacts, as discussed in Sections 2.4.1 and 2.4.2. The specific impacts in a standard single mode fiber (SSMF) are

$17\,ps/(nm\cdot km)$ for CD and $0.1ps\sqrt{km}$ for PMD (ITU-T Fiber Recommendations G.653 and G.655 [38]). For instance, if a fiber length of 1,000 km is assumed, the accumulated CD in total is 17 *ns/nm* (or 17,000 *ps/nm*) and the PMD is 3.16 *ps*. For example, assuming a sampling rate is 28 Gs/s (or 35.7 ps) and one complete OFDM symbol consists of 288 samples (according to 256 FFT size + 32 of CP length). Therefore, one symbol length is 10.28 *ns* (35.7 × 288) and CP length is 1.14 *ns*. Thus, it is insufficient to neglect ISI owing to the accumulated CD, and it is necessary to determine its length.

Let us start by letting T_s denote the sampling rate and by considering N_{CP} and N_C, then the condition of the complete elimination of ISI is given by [9, 37] as

$$N_{CP}T_s > \tau, \tag{2.25}$$

and the pulse broadening owing to CD dominates PMD. Therefore, in this dissertation, the pulse broadening owing only to CD, τ_{CD}, is considered. $N_{CP} = N_C/8$ is used and τ_{CD} can be obtained by [12, 46] as follows:

$$\tau_{CD} = DL\frac{c}{f^2T_s}, \tag{2.26}$$

where *D* is CD in *ps/(nm·km)*, *L* is the length of the fiber, *f* is the carrier frequency, and *c* is the velocity of light in vacuum. Then, by combining Equation (2.25) and (2.26), the required IFFT/FFT size to neglect ISI is given as

$$N_C > \frac{8cD}{f^2T_s^2}L. \tag{2.27}$$

From Equation (2.27), Table 2.1 gives N_C versus channel dispersion tolerance in units of fiber spans. Normally, the distance is presented by a unit of span, and each span is approximately 79 km. Please note that Equation (2.27) is true only if there is no over-sampling. In oversampling, T_s may in fact be as short as desired, without thereby τ_{CD} may changed.

Table 2.1. The relation between the distance *D* in spans and the IFFT/FFT size required.

Number of Spans	CD [*ns/nm*]	$\Delta\tau$ [*ns*]	Estimated Number of Subcarriers (N_C)	Number of IFFT/FFT Size
1	1.36	0.30	68	128
7	9.52	2.13	478	512
15	20.40	4.57	1025	1024
30	40.80	9.15	2049	2048
60	81.60	18.30	4098	4096

Table 2.1 shows that the greater the N_C , the greater is the distance of transmission that can be achieved to neglect ISI; however, it is dependent on the types of mapped constellation points. For instance, with 4096 points of IFFT/FFT, the maximum distance that can be reached is 60 spans (4740 km).

Furthermore, two important parameters used are the bit rate and the spectrum bandwidth. The bit rate is expressed by [46] as follows:

$$BR = \frac{N_{uf} M T_s}{N_C + N_{CP}}, \tag{2.28}$$

where N_{uf} is the number of useful subcarriers and M is the number of bits transmitted in each subcarrier. Then, the bandwidth can be calculated by [46]

$$BW = \left(N_{uf} + N_p\right) f_k, \tag{2.29}$$

where N_p is the amount of pilot data and f_k is the frequency spacing. Normally, for wavelength division multiplexing (WDM) transmission systems, the bandwidth in each channel should not exceed 50 GHz. Therefore, one OFDM spectrum band should not have more than 50 GHz. The bit rate can be doubled by using polarization division multiplexing (PDM). In addition, if the N_{uf} and T_s are fixed, the bit rate depends on increasing or reducing M .

CHAPTER 3

OFDM Frame and Radio Frequency Synchronization

3.1 Introduction

As shown in the previous chapter, synchronization is required both on OFDM frame and frequency to make the OFDM communication system work properly. This chapter focuses on the two main synchronization processes, which are the FFT window and the CFO correction. The process location is shown in Figure 3.1.

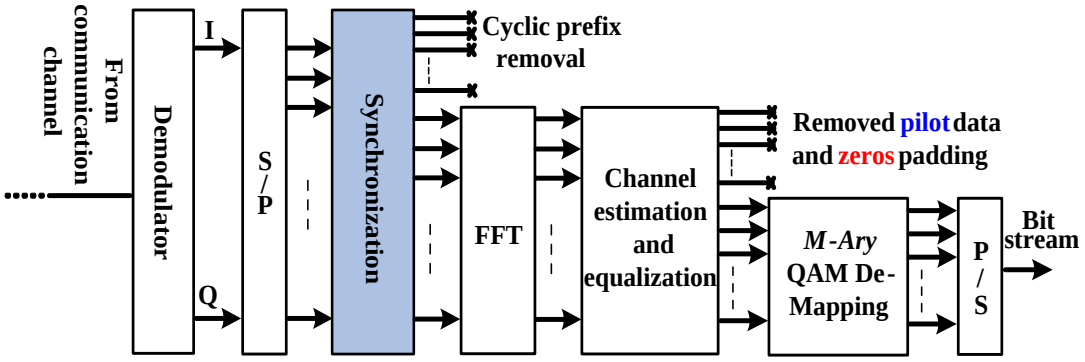

Figure 3.1. Block diagram of the considered part in this chapter.

OFDM frame synchronization is needed to correctly demodulate the received signal by FFT. Otherwise, the phasor of the received data signal will be rotated. Consequently, intersymbol interference (ISI) and intercarrier interference (ICI) will occur, which are described in detail later in this chapter. Therefore, the FFT window must be correctly identified and bound in the cyclic prefix (CP) area. In addition, the corrected FFT window supports a better estimation and compensation of IQ imbalance [47].

For CFO, which directly generates ICI, the signal loses orthogonality of each subcarrier. The CFO comes from the demodulated frequency at the receiver and is not

identical to the frequency at the transmitter. Therefore, the two frequencies must be equal and the offset at the receiver must be cancelled to compensate for ICI.

The impacts of ISI and ICI due to a mismatched FFT window are given in Section 3.2. Next, the OFDM frame synchronization method and results including the proposed method are shown in Sections 3.2.1 and 3.2.2, respectively. Then, the effect of CFO is given in Section 3.3. In the last section, the estimation and compensation for CFO are proposed.

3.2 OFDM Frame synchronization

This section deals with the impacts of time and frequency mismatch in OFDM communication systems. This directly contributes to ISI and ICI problems. These effects cannot be avoided within real-world communication systems. However, it is possible to compensate for them as discussed in the following sections**.**

3.2.1 Impacts of FFT window mismatch

At the transmitter end, the OFDM signal including CP is generated using an inverse fast Fourier transform (IFFT) with a certain length and values of the input data (for example, *M-ary* QAM constellation mapping). It is then IQ-modulated onto an optical carrier.

At the receiver end, the data is recovered by an FFT unit. The corrections to the original specific length and position must be known and the specific length is called the FFT window, which is required to neglect ISI and minimize ICI. The correct FFT window must be detected, otherwise the received phasor will be rotated causing ISI and ICI. The starting point of the FFT window consists of three main cases which are either too late, correct, or too early. These positions are discussed below and shown in Figure 3.2.

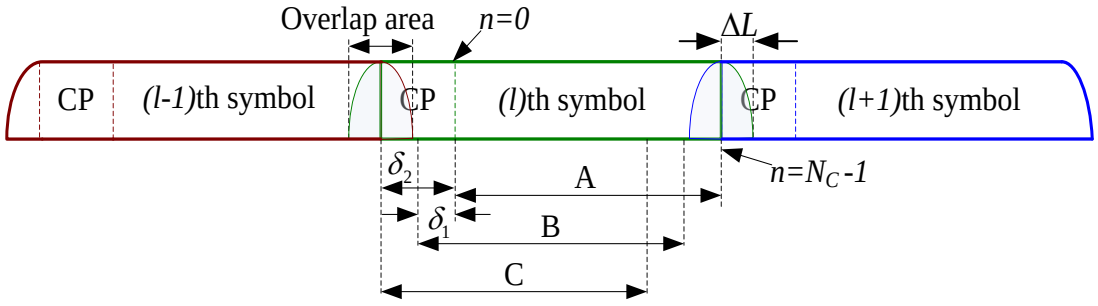

Figure 3.2. The three FFT window starting point cases to neglect ISI:

A. Too late.

B. Correct point.

C. Too early.

Figure 3.2 shows an example of three adjacent OFDM symbols which are the *(l-1)*th, the *(l)*th and the *(l+1)*th symbol. A CP is appended to the head of each OFDM symbol as a repetition of the end of the OFDM symbol itself. This allows performing linear convolution of optical channel and OFDM signal to be worked as circular convolution [48]. Therefore, each OFDM symbol has the sample index *n* sequence where $n \in \{-N_{CP}, \ldots, -1, 0, 1, \ldots, N_C - 1\}$.

In addition, at the receiver part, each symbol is dispersed owing to the optical channel as discussed in the previous chapter. Therefore, some parts of the two adjacent symbols are overlapped and added. Obviously, as discussed below, three main scenarios are possible. Define the variables as follows:

- l is the symbol index.
- n is the sample index input to the FFT calculation unit on each symbol.
- $Y_l(k)$ is the received baseband signal in frequency domain where $k = 0, \ldots, N_C - 1$ is subcarrier index on (*l*)th symbol.
- $y_l(n)$ is the received sample baseband signal in time domain on (*l*)th symbol obtained by $y_l(n) = x_l(n) \otimes h(n)$. $\otimes$ stands for convolution operator and $h(t)$ is channel impulse response (CIR).
- $X_l(f)$ is the transmitted signal in frequency domain on (*l*)th symbol.
- $x_l(n)$ is the transmitted sample signal in time domain on (*l*)th symbol.

- ΔL is the number of overlapped samples on each symbol and it is shorter than N_{CP}.
- δ_1 is the timing offset samples from $n=0$ to the starting point of B.
- δ_2 is the timing offset samples from $n=0$ to the starting point of C.

Scenario A

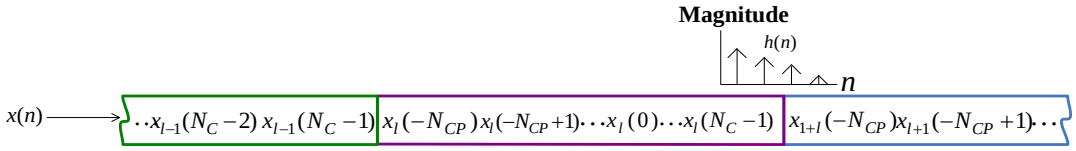

Figure 3.3. Behavior of the two adjacent OFDM symbols for Scenario A.

In this case, from Figure 3.2, the starting point occurs at $x_l(0)$ and it can be redrawn again by putting the details of sample indices into each OFDM frame as shown in Figure 3.3. In this case ISI will occur at the end sample area of $x_l(n)$ owing to the optical channel, *h(t)*. To illustrate the ISI impact, assume that $N_C = 32$, $N_{CP} = 8$ and CIR is 4. Then calculate convolution of the OFDM symbol sequence and CIR sequence. By time reversing the CIR and then sweeping it across the OFDM symbol sequence, we obtain the equation below,

$$y(0) = x_{l+1}(-6)h(3) + x_{l+1}(-7)h(2) + x_{l+1}(-8)h(1) + x_l(31)h(0) \quad (3.1A)$$

$$y(1) = x_{l+1}(-7)h(3) + x_{l+1}(-8)h(2) + x_l(31)h(1) + x_l(30)h(0) \quad (3.1B)$$

$$y(2) = x_{l+1}(-8)h(3) + x_l(31)h(2) + x_l(30)h(1) + x_l(29)h(0) \quad (3.1C)$$

y(0), y(1) and *y(2)* are the convolution outputs. From Figure 3.3, it can be easily observed that the input to the FFT unit, $y_l(n)$ contains ISI signal which is derived from considering some parts of the successive *(l+1)*th OFDM symbol. Consequently, the system performance would be degraded if we select this case as a starting point for FFT window.

Scenario B

In this case, the starting point occurs before the end of the CP part but after the end of the ISI area as analyzed from the previous section. The input to the FFT unit is shifted to the left by δ_1 and it contains only samples from the *(l)*th symbol, i.e.

$x_l(n-\delta_1)$ where $n=0,\ldots,N_C-1$. Therefore, there is no ISI from the previous OFDM symbol because there is no overlapped area between the two adjacent OFDM symbols. However, this causes a rotated phasor for each subcarrier but the orthogonality of the subcarriers relative to each other is still maintained. Consequently, there is also no ICI. For easy of understanding, a mathematical model is shown. From Equation (2.1) in the preceding chapter, the following is obtained [49-50]:

$$\begin{aligned} Y_l(k) &= FFT(y_l(n)) = FFT(x_l(n-\delta_1))FFT(h(n)) \\ &= \sum_{n=0}^{N_C-1} x_l(n-\delta_1)e^{-j2\pi nk/N_C} \cdot \sum_{m=0}^{N_C-1} h(n)e^{-j2\pi mk/N_C} \\ &= \sum_{n=0}^{N_C-1}\left(\frac{1}{N_C}\sum_{f=0}^{N_C-1} X_l(f)e^{j2\pi(n-\delta_1)f/N_C}\right)e^{-j2\pi nk/N_C} \cdot H(k) \\ &= \frac{1}{N_C}\sum_{f=0}^{N_C-1} X_l(f)e^{-j2\pi\delta_1 f/N_C}\sum_{n=0}^{N_C-1} e^{j2\pi(f-k)n/N_C} \cdot H(k) \\ &= X_l(k)e^{-j2\pi k\delta_1/N_C} \cdot H(k). \end{aligned} \qquad 3,2$$

Where,

$$\sum_{n=0}^{N_C-1} e^{j2\pi(f-k)n/N_C} = \begin{cases} N_C, & for \quad f=k \\ 0, & for \quad f\neq k \end{cases}. \qquad (3.3)$$

Equation 3.2. indicates that only the phasor is rotated, while the orthogonality of all subcarriers is still maintained.

Figure 3.4 shows an example of the impact of FFT window where the position is within the CP but it is shifted by δ_1 samples. For simplicity, the result is presented in terms of 16-QAM constellation points in the complex plane and the optical channel impact is omitted. The picture is simulated with a 1024-point FFT size with 128 points of CP, but without noise or channel dispersion. On the left hand side is the case where the FFT window position is correct, when the starting point is the same as Scenario A but there is no overlapped and added area, and the constellation points are located on the correct positions. The right hand side presents the case in which the constellation points have been rotated because the starting point of the FFT window is

shifted as shown in Figure 3.2. As a result, more than 16 points are generated in the complex plane.

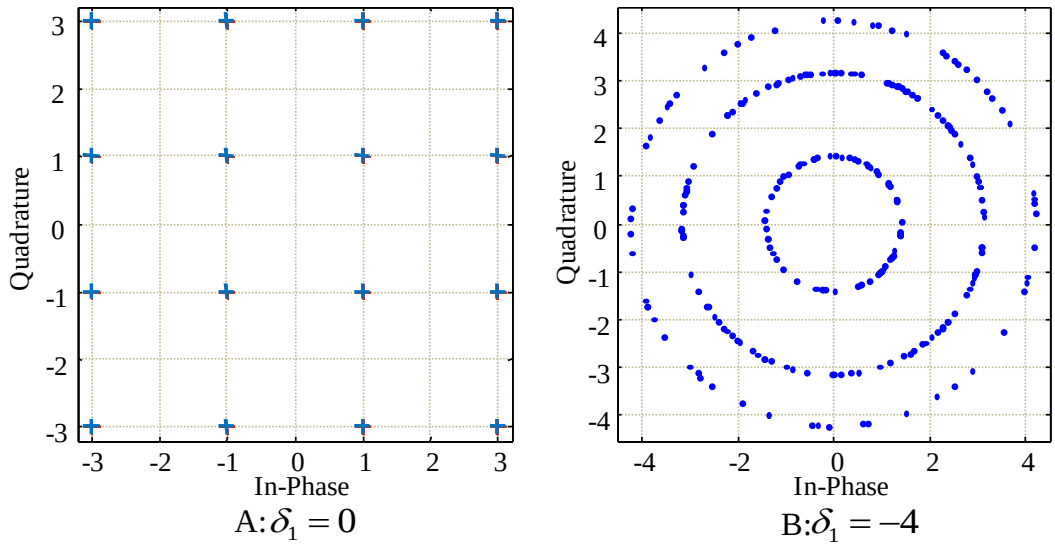

Figure 3.4. The 16-QAM constellation points rotated owing to the timing error of the OFDM frame; A: without impact; B: when the starting point is at δ_1.

However, at the receiver part, if the position error is small, the rotating phasor in each subcarrier can be compensated very easily in the channel equalization unit by using one-tap equalization, which will be discussed in Chapter 4. Therefore, this position would be a correct point of the starting FFT window which can neglect ISI and ICI problems.

Scenario C

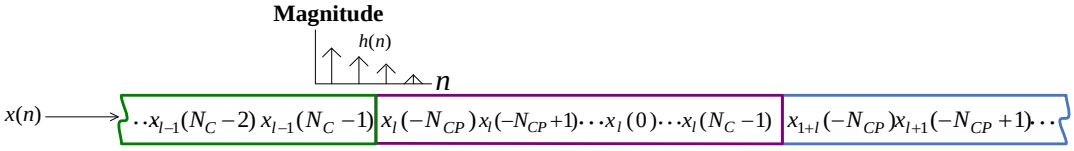

Figure 3.5. Behavior of the two adjacent OFDM symbols for Scenario C.

From Figures 3.2, the starting point is at the beginning of the *(l)*th symbol. Therefore, the input signal of FFT unit contains ISI signal as analyzed from Scenario A. The starting point of the main part is shifted to the left by $\delta_2 = N_{CP}$, i.e. $x_l(n-\delta_2) = x_l(n-N_{CP})$ where $n = 0,\ldots,N_C-1$, which are from the *(l)*th symbol.

From Figure 3.5 and by assuming N_C and N_{CP} are the same as Scenario A, the ISI impact from $x_{l+1}(n)$ symbol can be seen after computing convolution of those two sequences from CIR and OFDM symbol sequence in the following,

$$y(0) = x_{l-1}(29)h(3) + x_{l-1}(30)h(2) + x_{l-1}(31)h(1) + x_l(-8)h(0) \quad (3.4A)$$

$$y(1) = x_{l-1}(30)h(3) + x_{l-1}(31)h(2) + x_l(-8)h(1) + x_l(-7)h(0) \quad (3.4B)$$

$$y(2) = x_{l-1}(31)h(3) + x_l(-8)h(2) + x_l(-7)h(1) + x_l(-6)h(0) \quad (3.4C)$$

As can be seen in Equations (3.4A) - (3.4C), ISI occurs. In addition, the input signal to FFT unit is shifted by δ_2; therefore, the phasor of the desired signal is also rotated after calculating FFT as analyzed in Equation (3.2).

3.2.2. OFDM frame synchronization algorithm

Based on all cases of FFT window lag in the OFDM symbol, the starting point is clearly very important and must be detected properly as discussed in the last section. Many researchers and research institutes have proposed various techniques for OFDM frame synchronization both in wireless and optical communication applications [8-10, 51-53]. However, in this dissertation, only three useful and powerful techniques are treated, namely a special OFDM-symbol-aided technique, CP-bases-aided method, and an orthogonal-code-aided method, as discussed in the next section. All these techniques are based on a correlation technique.

3.2.2.1 Special OFDM symbol aided technique

A widely used technique, also employed in optical OFDM communication systems, is from Schmidl and Cox [50]. They proposed that at the transmitter end, one special OFDM symbol is split into two parts. The first (Part A) and second (Part B) parts are set to be identical in the time domain, as shown in Figure 3.6. However, the total symbol length is the same as the normal OFDM symbol. Then, the signal is followed by many normal OFDM symbols, for example, 50, 100, or 150 symbols. In total, one set is called OFDM frame.

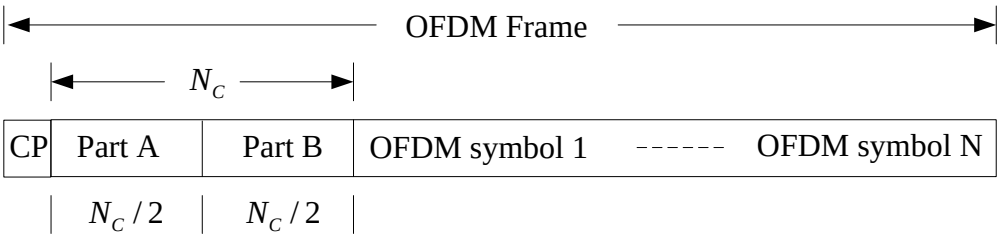

Figure 3.6. An example of OFDM frame in the time domain, including a special symbol for detecting the starting point of the FFT window.

N_C is the FFT size. At the receiver end, the received sample signal is fed into two branches for calculating the correlation and finding a maximum peak, as shown in Figure 3.7.

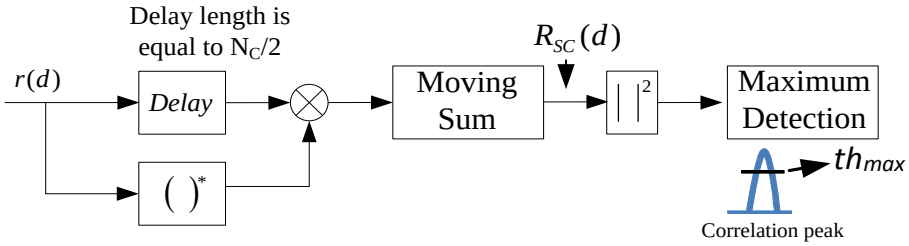

Figure 3.7. The correlator proposed by Schmidl and Cox.

Here, $th_{\max}$ is the maximum threshold. The correlator is shown in Figure 3.7. The received signal $r(d)$ is split into two branches. One branch is delayed, e.g., by a RAM, where the length is equal to the half of the OFDM symbol length. The other one denoted by $()^*$ is fed to the complex conjugator. Next, both signals are multiplied and fed to the moving sum unit, where the length of the summation is equal to $N_C/2$. Then, the signal magnitude is squared. Thus, the starting point of the OFDM frame is defined by the correlation peak. Hence, the length of the waiting room is called the sliding correlation window length.

Obviously, the peak reaches the maximum when the second part is shifted until it matches to the first part. Finally, The FFT window is obtained/detected when the maximum of the correlation peak is higher than $th_{\max}$. From Figure 3.7, the signal after the moving sum can be mathematically expressed as [51]

$$R_{SC}(d) = \sum_{n=0}^{N_C/2-1} r^*(d+n)r(d+n+N_C/2), \tag{3.5}$$

and the output signal before sending to the decision circuit is

$$P_{SC}(d) = \left|R_{SC}(d)\right|^2, \tag{3.6}$$

where P_{SC} is the correlation output and $r(d)$ is the received sample signal in the time domain.

Hence, to compromise and guarantee the starting point of the FFT window correctly and to implement easily (or with low complexity) in hardware, the correlation peak is compared with a threshold, which is set to be high enough in order to define the starting point. If the peak is higher than the threshold level, the starting FFT window is detected. This implies that there is no need to calculate the normalized factor, as proposed in [53]. Similarly, implementation of the division unit in hardware can be avoided, which would take a lot of resources and calculation time.

3.2.2.2 CP-based-aided method

In reality, this method is very similar to that reported by Schmidl and Cox [51], which has been discussed in the previous section. However, to find the starting position of the FFT window, in this section, the CP and the useful sample, which are used as CP itself, are also used to calculate the correlation peak. Again, both are identical in the time domain from the transmitter end, as shown in Figure 3.8. This approach is called the CP-based technique.

The correlation peak is calculated by the same way as in Equation (3.5) and (3.6) at the receiver part, except that the length of sliding window is smaller and it is equal to the CP length. Then, the maximum peak is also detected by the same way as in the last section.

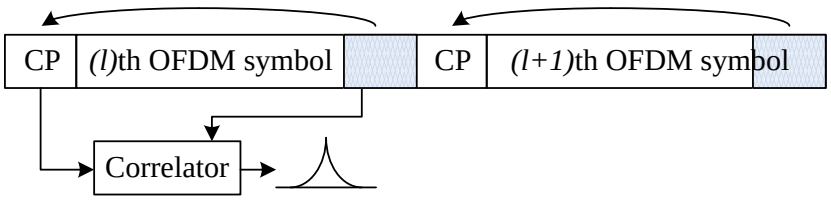

Figure 3.8. OFDM frame synchronization using CP.

The correlation peak is given by [49]

$$P_{CP}(d) = \left| \sum_{n=0}^{N_{CP}} r^*(d+n) \cdot r(d+n+L_{CP}) \right|. \tag{3.7}$$

3.2.2.3. Orthogonal-code-aided method

This is the proposed method for this thesis. This technique is similar to the code division multiple access (CDMA) scheme. The transmitter sends an orthogonal code sequence, which can be generated from either an m-sequence code, a Gold sequence code, or a Barker code [26, 54-55]. However, from the investigation using simulation method, a modified Gold sequence code is found to give better results and is used in this thesis. For details, please see Appendix D. All these are called orthogonal code symbols (OCSs). An OCS is added to the head of the OFDM frame and then sent out, as shown in 3.9A.

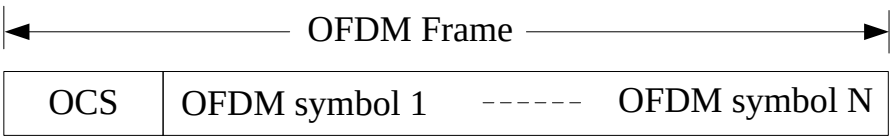

A: The OFDM frame, including one OCS for synchronization.

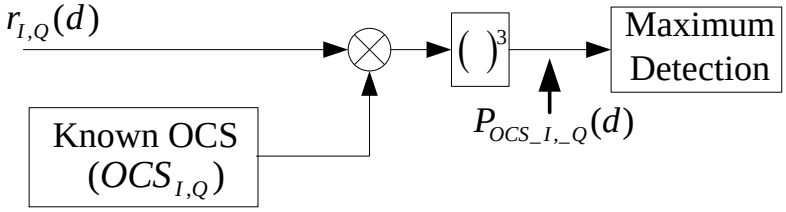

B: The correletor, which is proposed by OCS aiding.

Figure 3.9. OFDM frame synchronization by the OCS method.

At the receiver end, the sampled $r_{I,Q}(d)$ is correlated with the known OCS code separately for I and Q channel. The detail of the correlation calculation for I channel is given by

$$P_{OCS\_I1}(d) = \left(\sum_{n=0}^{L_{OCS}-1} OCS_I(n) r_I(d - L_{OCS} + n) \right)^3, \quad (3.8A)$$

$$P_{OCS\_I2}(d) = \left(\sum_{n=0}^{L_{OCS}-1} OCS_Q(n) r_I(d - L_{OCS} + n) \right)^3. \quad (3.8B)$$

The correlation calculation for Q channel is expressed by

$$P_{OCS\_Q1}(d) = \left(\sum_{n=0}^{L_{OCS}-1} OCS_I(n) r_Q(d - L_{OCS} + n) \right)^3, \quad (3.9A)$$

$$P_{OCS\_Q2}(d) = \left(\sum_{n=0}^{L_{OCS}-1} OCS_Q(n) r_Q(d - L_{OCS} + n) \right)^3, \quad (3.9B)$$

where $P_{OCS\_I1}(d)$, $P_{OCS\_I2}(d)$. $P_{OCS\_Q1}(d)$ and $P_{OCS\_Q2}(d)$ are the correlation output one and two for each I and Q channel. OCS_I and OCS_Q denote the known OCS for I and Q channel, and L_{OCS} is the length of the OCS. $(\cdot)^3$ is used for noise suppression and detecting the polar of I and Q channel. The proposed algorithm searches for the maximum or minimum peak of the correlation, which is done by comparing the correlation output with the maximum threshold, $th_{\max}$, and the minimum threshold, $th_{\min}$, respectively, to detect the starting point of OFDM frame and IQ channel swapping. $th_{\max}$ and $th_{\min}$ are used to check the polarity of the I and Q channel. If the peak of the correlation output is higher than $th_{\max}$, there is no polarity of I and Q inverted. However, if the peak of the correlation output is less than $th_{\min}$, it indicates that the polarity of the I and Q is inverted. In additional, to detect the starting point as well as to correct swapped I and Q channels, both input I and Q must be correlated with the same OCS_I and OCS_Q. As a result, there are four main cases of I and Q detection behavior which are shown in Table 3.1.

Table 3.1. I and Q detection behavior.

Indicator	Condition of no I and Q inversion	
$\hat{M}\max_I$	$\left(P_{OCS\_I1}(d)\right)^3 > th_{\max}$ and $\left(P_{OCS\_I2}(d)\right)^3 < th_{\max}$	No I and Q swapped
$\hat{M}\max_Q$	$\left(P_{OCS\_Q1}(d)\right)^3 > th_{\max}$ and $\left(P_{OCS\_Q2}(d)\right)^3 < th_{\max}$	
$\hat{M}\max_I$	$\left(P_{OCS\_I1}(d)\right)^3 < th_{\max}$ and $\left(P_{OCS\_I2}(d)\right)^3 > th_{\max}$	I and Q swapped
$\hat{M}\max_Q$	$\left(P_{OCS\_Q1}(d)\right)^3 < th_{\max}$ and $\left(P_{OCS\_Q2}(d)\right)^3 > th_{\max}$	
	Condition of I and Q inversion	
$\hat{M}\min_I$	$\left(P_{OCS\_I1}(d)\right)^3 < th_{\min}$ and $\left(P_{OCS\_I2}(d)\right)^3 > th_{\min}$	No I and Q swapped
$\hat{M}\min_Q$	$\left(P_{OCS\_Q1}(d)\right)^3 < th_{\min}$ and $\left(P_{OCS\_Q2}(d)\right)^3 > th_{\min}$	
$\hat{M}\min_I$	$\left(P_{OCS\_I1}(d)\right)^3 > th_{\min}$ and $\left(P_{OCS\_I2}(d)\right)^3 < th_{\min}$	I and Q swapped
$\hat{M}\min_Q$	$\left(P_{OCS\_Q1}(d)\right)^3 > th_{\min}$ and $\left(P_{OCS\_Q2}(d)\right)^3 < th_{\min}$	

According to all the conditions in Table 3.1 $\hat{M}\max_I$, $\hat{M}\max_Q$, $\hat{M}\min_I$ and $\hat{M}\min_Q$ are the maximum and minimum peak which is used to indicate the start point of OFDM frame for I and Q channel. Please note that owing to phase noise distortions, the correlation peak can become positive or negative, that is why the algorithm needs to search for both minimum and maximum. Hence, the IQ component swapping can be defined from swapping between I and Q correlation peak. An example of I and Q detection behavior is shown in Figure 3.10

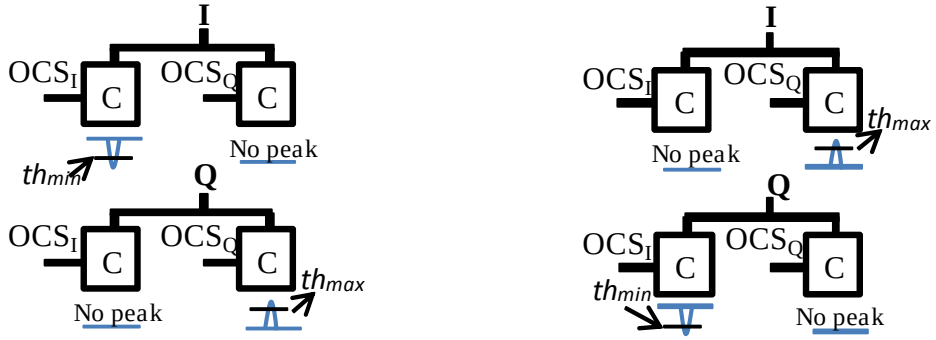

A: In case of no IQ swapped and I inverted. **B:** In case of IQ swapped and I inverted.

Figure 3.10. An example of the OCS peak detection and I and Q alignment technique.

Obviously, the proposed method can detect all the situations of phase rotation. For more details regarding the m-sequence code, Gold sequence code, and Barker code, please see Appendix B–D.

3.2.3. OFDM frame synchronization performance results

In this section, the performance of the OFDM frame synchronization is shown for all methods. In addition, the functionality of the proposed method is confirmed by both simulation and experimental results.

3.2.3.1 Simulation results

In this section, the system performance of the proposed algorithm for OFDM frame synchronization and IQ alignment is investigated by simulations using the setup described later. In this simulation, one OFDM symbol was defined by 288 samples (FFT size of 256 + 32 in CP length). Each subcarrier is modulated by 4-QAM. 128 subcarriers around the spectrum center are zero padded for oversampling. The sampling rate is set to 28 Gs/s. A fiber length of 1,000 km of standard single mode (SSM) fiber with a chromatic dispersion (CD) of 17 *ps/(nm·km)* is assumed.

Figures 3.11A and 3.11B show the correlation peak results of the conventional scheme from Schmidl and Cox, and the proposed method, respectively. In comparison with the conventional method, the proposed method shows a clearer correlation peak, even for a low OSNR of 14 dB observed for both I and Q components. Additionally, there is no plateau and only one correlation peak is detected.

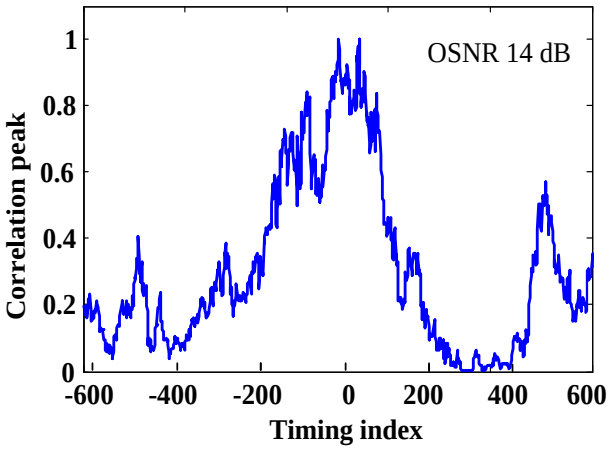

A: The correlation peak of the widely used technique (Schmidl and Cox)

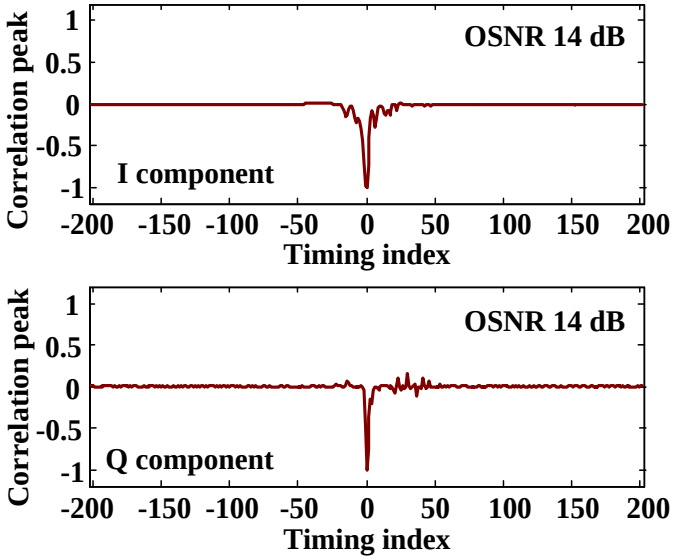

B: The correlation peak of the proposed method

Figure 3.11. Correlation peak of the conventional scheme (A) and the proposed method (B).

Next, the correlation peak under CFO environment is studied. Hence, all the parameters are the same as in the previous setup, but a CFO of 100 MHz has been considered. Figures 3.12A and 3.12B plot the correlation peak results of the conventional and the proposed method for a CFO of 100 MHz. The proposed method still shows a clear correlation peak on both I and Q components. However, the curve around the base of the peak is getting bigger and the base is getting wider. Additionally, the maximum peak is also shifted to the left hand side by 1 step from the exact FFT window starting point, which is not a problem for the system performance because it is very simple to compensation in one-tap equalization unit.

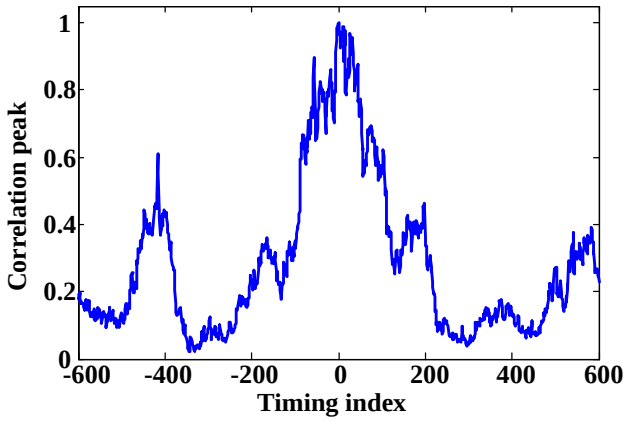

A. The correlation peak of the Schmidl and Cox method.

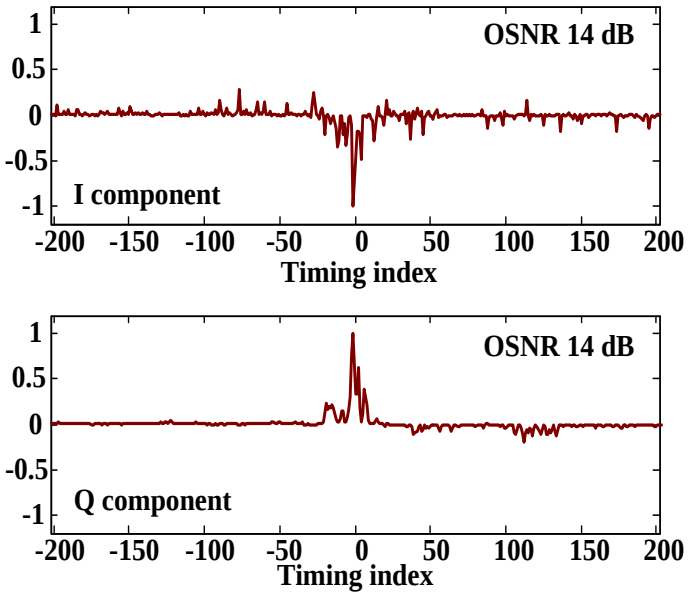

B. The correlation peak of the proposed method.

Figure 3.12. Correlation peak for a CFO of 100 MHz by (A) from Schmidl and Cox and (B) the proposed method.

3.2.3.2 Experimental results

Figure 3.13 shows the experimental setup of the self-homodyne CO-OFDM.

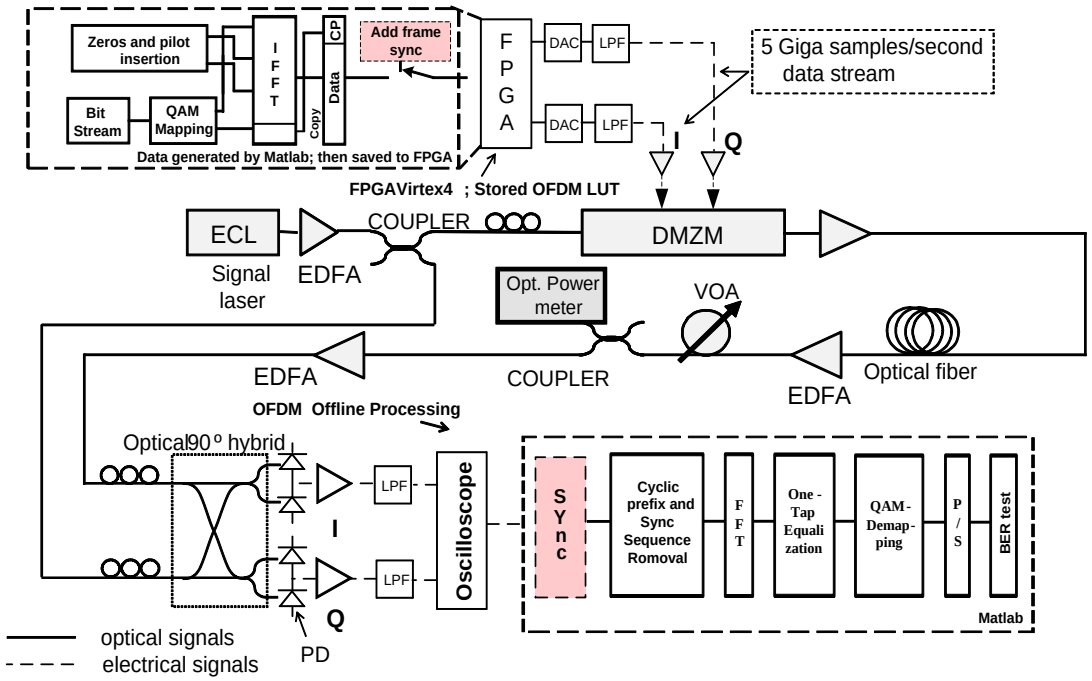

Figure 3.13. Experimental setup for OFDM synchronization and IQ aligning.

At the transmitter end, the OFDM symbol data are preprocessed in two synchronized Virtex-4 FPGAs for I and Q. The OFDM frame is generated as described in the simulation section. Then, the digital samples are converted into the analog domain by two Micram digital-to-analog converters at the rate of 5 Gs/s and a resolution of 6 bits. For electrical-optical (E/O) conversion, a Dual-Parallel Mach-Zehnder Modulator (DPMZM) is used to modulate the 1550 nm light of an external cavity laser (ECL) with a specified linewidth of 150 kHz and 3 dBm launch power input for each optical fiber span. After transmission over the SSMF fiber, the signal is fed to a variable optical attenuator (VOA), followed by an erbium-doped fiber amplifier (EDFA) to add ASE noise. The polarization is manually controlled. At the receiver, the signal is mixed with a local oscillator laser using a polarization-diverse 90° optical hybrid. Two differential photodiode pairs convert the signal from the optical to the electrical domain (O/E). After photodetection and linear amplification, I and Q are sampled and stored by an oscilloscope (TDS6804B) for offline processing.

Figures 3.14A and 3.14B show the correlation peak for the I and Q component of one OFDM frame at a received power of −14 dBm and −29 dBm, respectively, after passing through an optical fiber length of 160 km (about 2 spans). The proposed method shows a good performance under practical conditions even for a low received input power at −29 dBm. There is only one peak and no plateau.

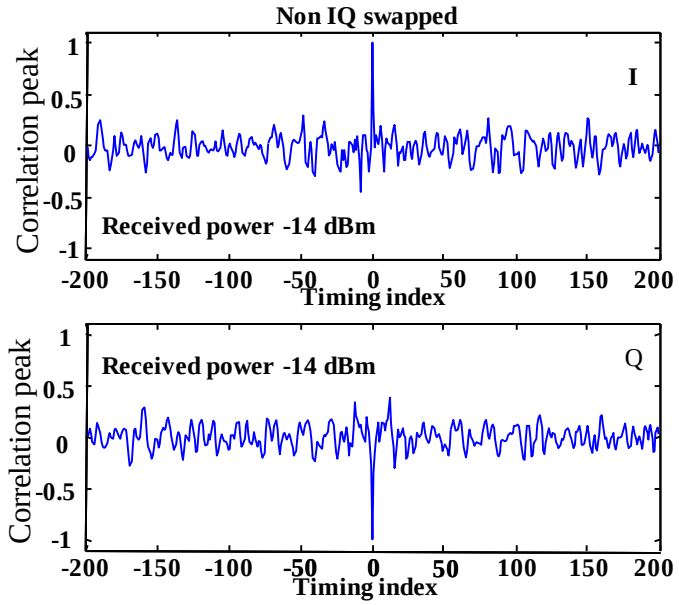

A: The correlation peak of the IQ components at the received power of −14 dBm.

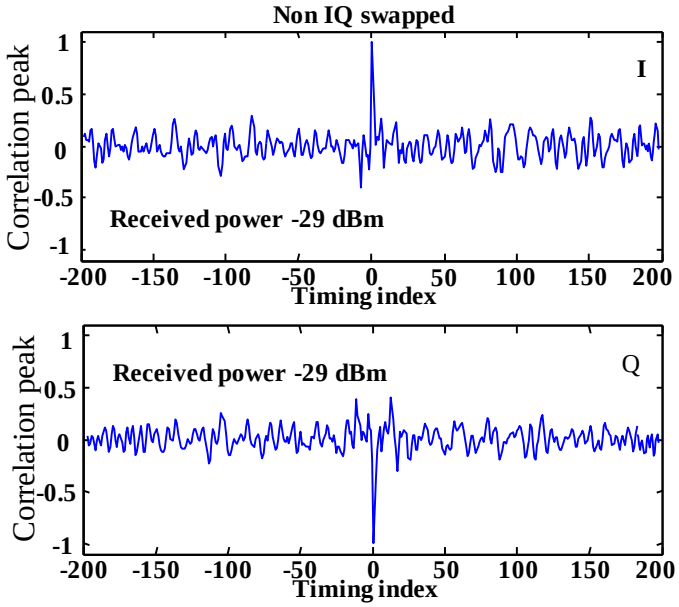

B: The correlation peak of the IQ components at the received power of –29 dBm.

Figure 3.14. Correlation peaks of the IQ components for the OFDM frame after 160 km.

Next, the performance of the correlation peak under a CFO of 60 MHz is obtained. The OCS sequence and OFDM signal, which are induced by CFO, were programmed using Matlab and saved into FPGAs, as already discussed in the experimental setup. CFO is discussed in detail in the next section.

Figure 3.15 shows the IQ component correlation peakat the received powers of –29 dBm. After passing through the optical fiber length of 160 km, the proposed method still gives good performance even under CFO of 60 MHz. Again, there is only one peak and no plateau. However, the correlation curve is fluctuated.

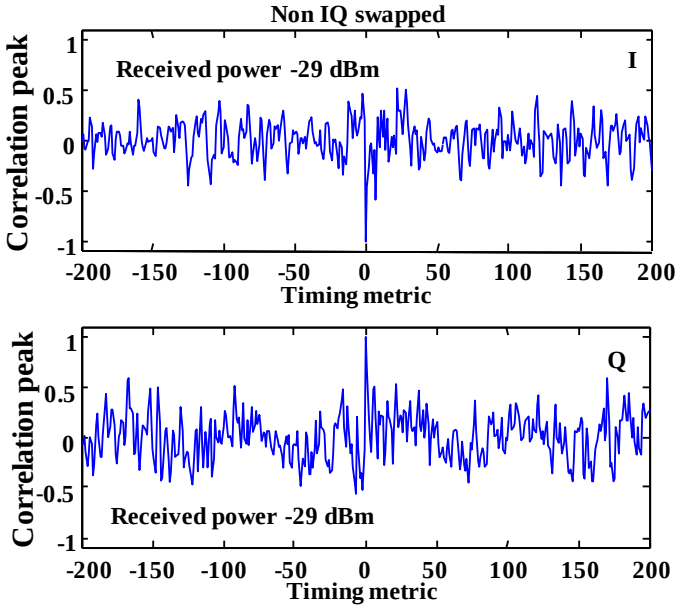

Figure 3.15. Correlation peak of the IQ components for the OFDM frame synchronization under a CFO of 60 MHz.

3.3 Carrier frequency offset

Carrier frequency offset (CFO) is one issue that needs to be managed and corrected. In this section, the impact of CFO to OFDM communication systems is presented. Then, the proposed method for CFO compensation is given in the following section. Finally, to verify the proposed method, both simulation and experimental results are shown.

3.3.1 Impacts of the carrier frequency offset

The CFO, which is generally caused by the local oscillator (LO), generates a frequency that is not exactly the same as the carrier from the transmitter. However, to making them the same is difficult because the lasers are sensitive to temperature and current, and the CFO can drift up to GHz region at the receiver after down-conversion to baseband [56]. Consequently, the frequency difference between transmitter laser and local oscillator generates CFO and that is denoted by f_{offset}, where $f_{offset} = f_{Tx} - f_{Rx}$. Hence, f_{Tx} is the transmitter carrier frequency and f_{Rx} is the receiver carrier frequency. In reality, the baseband signal must start at zero Hertz after down-conversion for the OFDM spectrum band.

Normally, the CFO is normalized with the subcarrier spacing, denoted by f_k, and CFO can be split into an integer part I, and a fractional part $\widetilde{\varepsilon}$. The quantities are expressed by $f_{offset} = (I + \widetilde{\varepsilon}) f_k$. The normalized CFO f_ε is given by [48, 56]

$$f_\varepsilon = \frac{f_{offset}}{f_k} = (I + \widetilde{\varepsilon}), \tag{3.10}$$

where $|\widetilde{\varepsilon}| < 0.5$.

The fractional CFO introduces ICI because all the main lobes of the subcarriers are leaked and added to each other as shown in Figure 3.16. Then, the signals of all subcarriers are no longer orthogonal to each other.

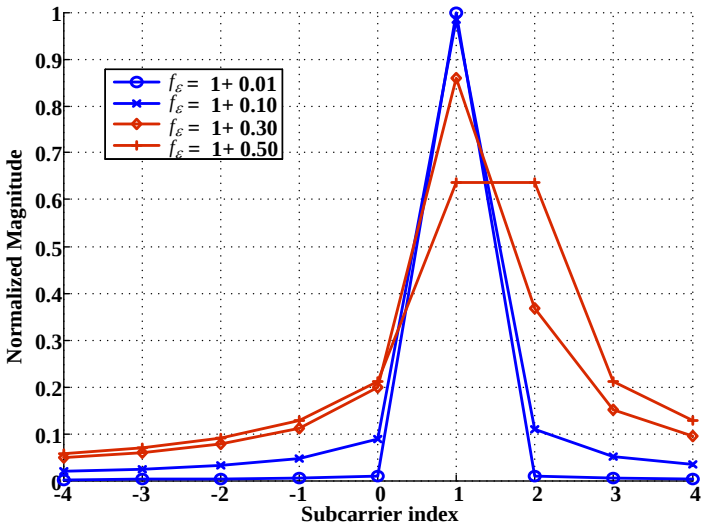

Figure 3.16. Subcarrier leaking owing to the frequency offset for an FFT size of 8.

Figure 3.16 plots the spectrum magnitude of a subcarrier, which is induced by CFO. Hence, in this example, I=1 is assumed. The plot clearly shows that increasing the fractional CFO increases the leaking and adding power to the neighbor subcarriers. Then, ICI occurs. For $\widetilde{\varepsilon} = 0.01$ and 0.10, the magnitudes are little reduced and the base of the main sidelobe becomes wider.

The integer CFO part does not cause ICI because there is no magnitude leaking to the neighbor subcarriers, rather the whole spectrum band is shifted by an

integer of I where $I = -N_C/2 \ldots N_C/2$. To recover the signal in each subcarrier correctly, they just needed to be shifted back.

For further understanding of ICI due to fractional CFO, the mathematical expression is given below [49]:

$$
\begin{aligned}
Y_l(k) &= FFT\left(y_l(n)\right) = FFT\left(x_l(n)e^{j2\pi\tilde{\varepsilon}n/N_C}\right) \\
&= \frac{1}{N_C}\sum_{n=0}^{N_C-1}\left(\sum_{f=0}^{N_C-1}X_l(f)e^{j2\pi n(f+\tilde{\varepsilon})/N_C}\right)e^{-j2\pi kn/N_C} \\
&= \frac{1}{N_C}\sum_{f=0}^{N_C-1}X_l(f)\left(\sum_{n=0}^{N_C-1}e^{j2\pi n(f+\tilde{\varepsilon}-k)/N_C}\right) \\
&= \frac{1}{N_C}X_l(k)\sum_{n=0}^{N_C-1}e^{j2\pi n\tilde{\varepsilon}/N_C} + \frac{1}{N_C}\sum_{f=0,f\neq k}^{N_C-1}X_l(f)\sum_{n=0}^{N_C-1}e^{j2\pi n(f+\tilde{\varepsilon}-k)/N_C} \\
&= \underbrace{X_l(k)\frac{\sin(\pi\tilde{\varepsilon})}{N_C\sin(\pi\tilde{\varepsilon}/N_C)}e^{j\pi\tilde{\varepsilon}(N_C-1)/N_C}}_{desired\ signal} \\
&\quad \underbrace{+\sum_{f=0,f\neq k}^{N_C-1}\frac{\sin(\pi(f+\tilde{\varepsilon}-k))}{N_C\sin(\pi(f+\tilde{\varepsilon}-k)/N_C)}X_l(f)e^{j\pi(f+\tilde{\varepsilon}-k)(N_C-1)/N_C}}_{(ICI)},
\end{aligned}
\tag{3.11}
$$

where $y(n)$ is the input signal to the FFT unit and the optical channel impact is not considered. From Equation (3.11), the first term clearly denotes that both the phase and amplitude are distorted, while the second term is the result of interference between neighbor subcarriers. The interference causes a loss of orthogonality for all subcarriers. Therefore, this leads to disruption in phase and amplitude of the constellation points, as shown in Figure 3.15.

Figure 3.17 illustrates a 16-QAM constellation which is distorted by ICI impact. The $\tilde{\varepsilon}$ is assigned to be 0.01, 0.1, 0.3, and 0.5. The result confirms that amplitude and phase are increasingly distorted and the constellation is also collapsed. Therefore, ICI is one cause of performance degradation of the OFDM modulation system in both wireless and optical communication systems.

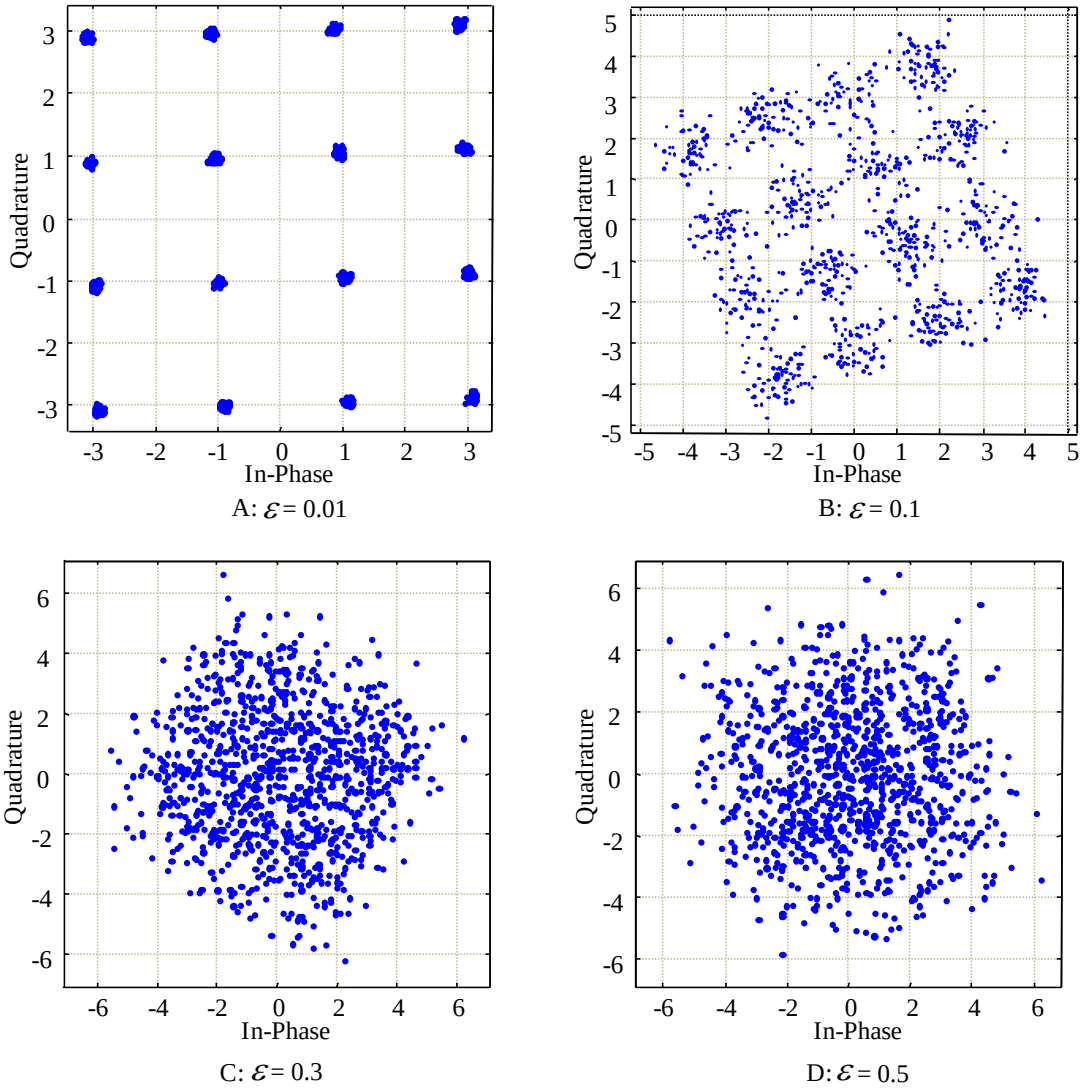

Figure 3.17. Phase and amplitude distortion owing to ICI for OFDM symbols, which are plotted in a 16-QAM constellation point mapping.

3.3.2 Carrier frequency offset correction

There are two well-known methods for estimating the fractional CFO. One is the Schmidl and Cox method, which considers in the time domain. Reconnecting to Equation (3.9), the fractional CFO can be estimated by calculating the phase between the first and second parts of the training symbol, which is given by [48]

$$\tilde{\varepsilon} = \frac{\angle R_{SC}(d)}{2\pi}, \tag{3.12}$$

where $R_{SC}(d)$ is given by Equation (3.5), and $\angle$ is the angle operator.

The second method is the Moose method, which considers in the frequency domain. Moose proposed transmitting two training OFDM identical symbols. By doing so, the fractional CFO is estimated as [55]

$$\tilde{\varepsilon} = \frac{1}{2\pi}\tan^{-1}\left(\frac{\sum_{K=1}^{N_C}\mathrm{Im}\left(Y_1(K)Y_2^*(K)\right)}{\sum_{K=1}^{N_C}\mathrm{Re}\left(Y_1(K)Y_2^*(K)\right)}\right), \tag{3.13}$$

where Y_1 and Y_2 are the output signals of the FFT unit of the first and second TS and $(\cdot)^*$ stands for complex conjugate operator.

Unfortunately, those two methods can estimate only the fractional CFO which is only a few MHz. For large CFO, including both integer and fractional CFOs is beyond the range and they cannot be estimated.

To overcome this problem, the RF-pilot tone based method [5, 57] is used in this dissertation. Only one RF-pilot tone is needed. The method is that the RF-pilot is inserted by adding a DC offset to the signal at the transmitter side. As a result, after taking FFT, the DC offset will appear at the first FFT bin output at the receiver side, as can be seen in inset A on the top of the Figure 3.18. Hence, bin means a sub-channel output index of FFT.

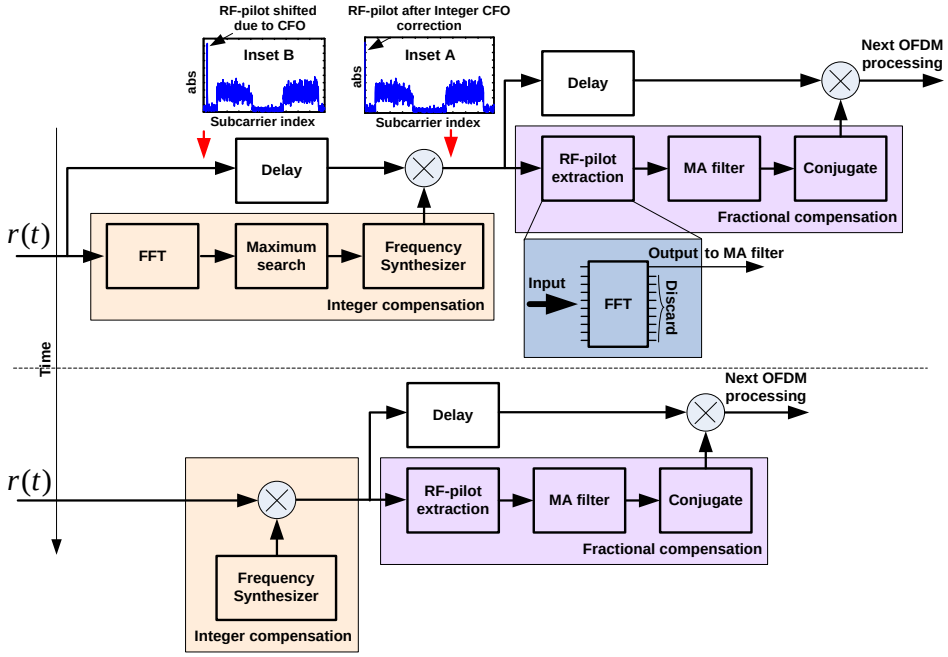

Figure 3.18. Proposed CFO compensation method for CO-OFDM.

By doing so, when the OFDM signal is passed through the CFO environment, the RF-pilot will be shifted, as shown in inset B of Figure 3.18. For implementing a filter to extract the RF-pilot tone, the filter bandwidth needs to be carefully selected and it is fixed in a certain band, but in reality, the CFO fluctuates by time. Generally, the filter bandwidth is in the hundred MHz region [58]. However, if the CFO is large and it can be increased up to the GHz range, then, the filter bandwidth may not be enough to cover such a large range.

To solve this problem at the receiver end, the CFO compensation should be done in two stages where the first one is rotating the whole frequency band back (integer CFO compensation) and the second is for fractional CFO compensation as shown in Figure 3.18. Obviously, from the first stage, it is possible to fix the center frequency of the filter to cancel the fractional CFO in the second stage.

From Figure 3.18, the integer offset is estimated by searching for the RF-pilot peak, I_{peak}, by the absolute value (abs) from all the FFT bin, where the input signal is from the OFDM frame synchronization processing and the FFT size is the same as N_C. Next, the frequency synthesizer generates the same frequency according to the FFT bin index that contains the RF-pilot peak and conjugated phase. Generally, for simple implementation of digital frequency synthesizer, a numerically controlled

oscillator (NCO) can be used [59-60]. The integer CFO, *I*, from the bin*th* index can be obtained by [56]

$$I = \begin{cases} I_{peak} - 1 & , 1 \le I_{peak} \le N_C / 2 \\ I_{peak} - N_C - 1 & , N_C / 2 + 1 \le I_{peak} \le N_C \end{cases}. \quad (3.14)$$

Then, the generated frequency is multiplied by the received signal to cancel the integer CFO.

The second issue is the fractional CFO compensation. In this process, firstly, the RF-pilot is extracted by using a low pass filter. In this thesis, a small FFT size, such as 32- or 64-point, is used as a filter and takes the FFT output only from the first bin, as shown in the inset of Figure 3.18 (however, it is not necessary to use FFT as a filter but other types of the filters can be used as well). If the sampling rate is fixed, the filter bandwidth depends on the FFT size. Next, the extracted pilot is fed to the moving average (MA) filter in order to minimize noise and followed by taking the conjugate before multiplying it by the received signal in order to cancel the fractional CFO.

Note that in case of slow changing of CFO, after the integer CFO is acquired, it can be held and this process can be skipped to decrease the cancelling time. However, the fractional CFO compensation stage should be performed every time because this method can also be used for PN compensation, as discussed in [5].

3.3.3 Carrier frequency offset correction performance results

This section presents simulation and experimental results of the proposed compensation method.

3.3.3.1 Simulation results

In this section, the performance of the proposed method is confirmed by simulation. The simulation parameters are the same as in Section 3.2.3.1, only the CFO is set to 2 GHz and the FFT size is increased to 1024 points in order to obtain more impact to the system. As a result, the frequency spacing is 27.343 MHz and the CFO is 73.149. Figure 3.19, shows the OFDM spectra for the case of the spectrum

band affected by CFO, which shifted to 74th bin owing to the integer CFO part, as shown in Figure 3.19A. After using the first stage, the whole spectrum is rotated back, as shown in Figure 3.19B.

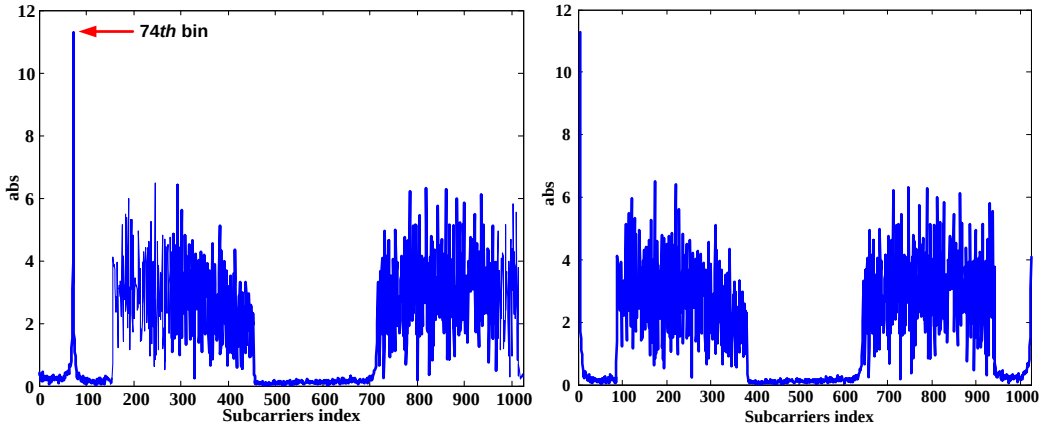

(A) (B)

Figure 3.19. The simulation result of

A: the shifted OFDM spectrum band due to CFO of 73.149.

B: the back rotated spectrum band after the first stage.

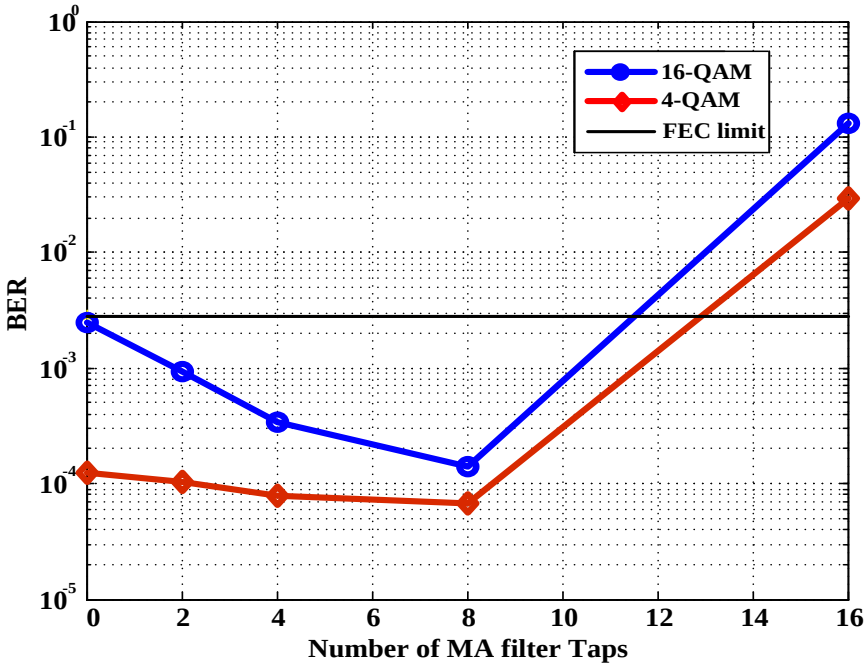

Figure 3.20. BER versus the number of MA filter taps for simulation result.

First, the impact of using MA filter taps (MFT) is considered. Figure 3.20 plots the bit error ratio (BER) versus the number of MFT. The MFT is varied by steps of 2^n from 2 to 16. However, in Figure 3.20, there is started by MFT=0 which means that the estimated fractional CFO signal is unfiltered. It can be clearly seen that when the MFT is increased, the BER is significantly improved and the optimum MFT is 8 taps, especially for 16-QAM. The BER is decreased and reaches the minimum at $9.09 \cdot 10^{-5}$ for 4-QAM and $8.60 \cdot 10^{-4}$ for 16-QAM. However, after the optimum taps are reached, the BER starts increasing again because the average estimated phase is getting away from the correct phase because the filter bandwidth is too narrow.

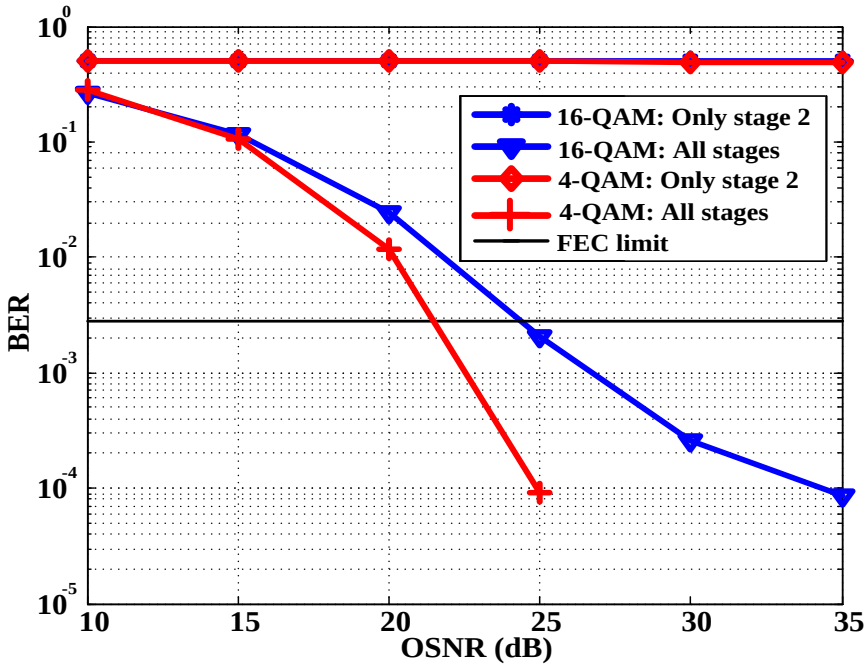

Figure 3.21. BER versus OSNR (dB) for simulation method.

Figure 3.21 plots the BER versus OSNR, which was varied in steps of 5 dB from 10 dB to 35 dB of 4-QAM and 16-QAM. The FFT size for the second stage filter is 64. As a result, the filter bandwidth for the second stage is fixed at 437 MHz. By the curves of using only the second stage, it can be seen that only the second stage is not enough to compensate for a wide range of CFO, but it also needs the first stage to rotate the whole spectrum back. BER of $9.09 \cdot 10^{-5}$ and $8.60 \cdot 10^{-5}$ for 4-QAM and 16-QAM are achieved, respectively. Obviously, the proposed method can also

compensate for PN as discussed in [6, 58, 72] and in this simulation and the sum of laser linewidth of 1 MHz is used.

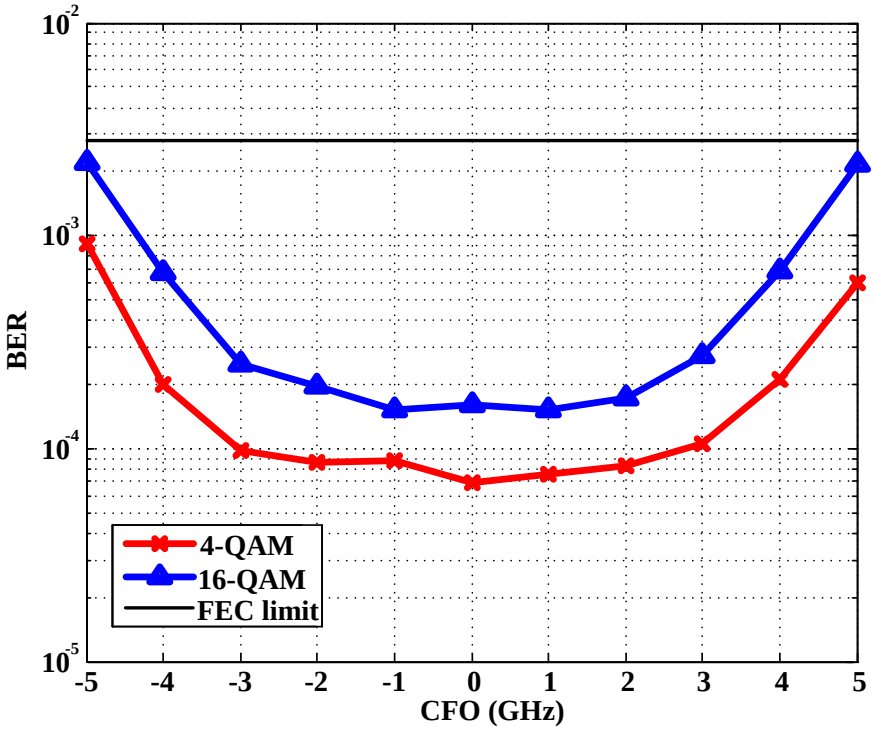

Figure 3.22. BER versus CFO where 4-QAM and 16-QAM are considered.

Figure 3.22 plots the BER against CFO which varies from –5 GHz to 5 GHz. The simulation setup is the same as shown in Figure 3.21. The OSNR of 25 dB and 30 dB are set for 4-QAM and 16-QAM, respectively. As we can see, the CFO is greatly compensated from –2 GHz to 2 GHz. At the CFO –3 GHz and 3 GHz, the BER performance is slightly decreased. However, when the CFO is increased to ±5 GHz, the BER is increased dramatically, but it is still below the forward error correction (FEC) limit. The proposed method can cover a very wide range of estimated CFO and is highly tolerant to PN.

3.3.3.2 Experimental results

In this section, the system performance is confirmed by an experimental method. The experimental setup and parameters are the same as in Section 3.2.3.2, but the OFDM signal is given for a CFO of 9.216 (180 MHz).

Figure 3.23A shows the absolute value (abs) of the FFT output. As can be seen, the RF-pilot is located at the 10th bin, which indicates the integer CFO. Figure 3.23B shows the abs of the FFT output after the received signal is compensated for integer CFO. The RF-pilot is rotated back to the DC subcarrier, which means that the integer CFO is completely compensated.

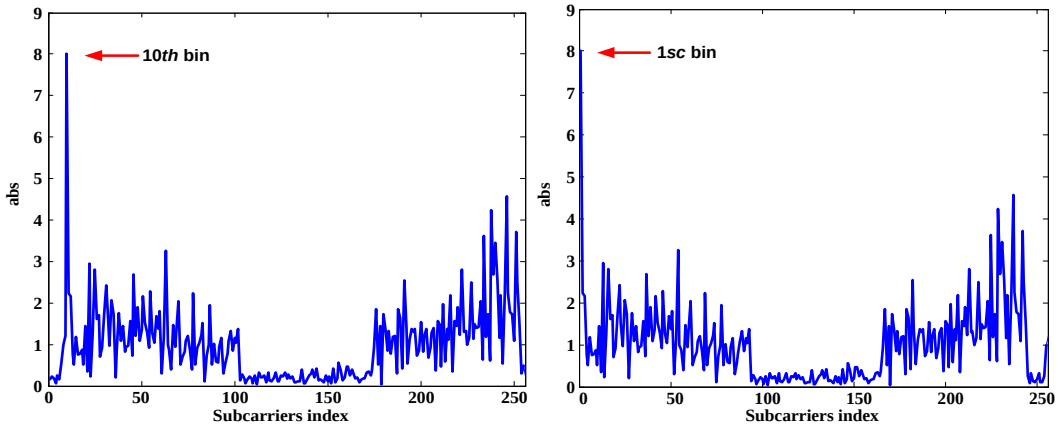

(A) (B)

Figure 3.23. The experimental result of

A: the shifted OFDM spectrum due to CFO of 9.216.

B: the rotated spectrum back after the first stage.

Next, the BER improvement of using an moving average (MA) filter is considered. Figure 3.24 presents the BER against the MFT. The MFT is varied the same way as in Figure 3.21 and again note that at the number MFT of 0 means, the MA filter is not applied. It is clearly seen that when the MFT is increased up to 8, the BER is slightly improved and the optimum MFTs is 8 taps, which is compatible to the simulation results. By using an MA filter, at the optimum MFTs taps, the BER of $2.11 \cdot 10^{-4}$ and $7.61 \cdot 10^{-4}$ can be achieved for Rx input power of –29 dBm and –34 dBm, respectively. However, for the Rx input power of –34 dBm, after the optimum taps are reached, the BER starts increasing again because the estimated average phase gets far away from the correct phase and the MA bandwidth is too small.

Without using MA filter, the BER is only $7.61 \cdot 10^{-4}$ and $1.2 \cdot 10^{-3}$ for Rx input power of –29 dBm and –34 dBm, respectively. However, all BER values are below the FEC limit.

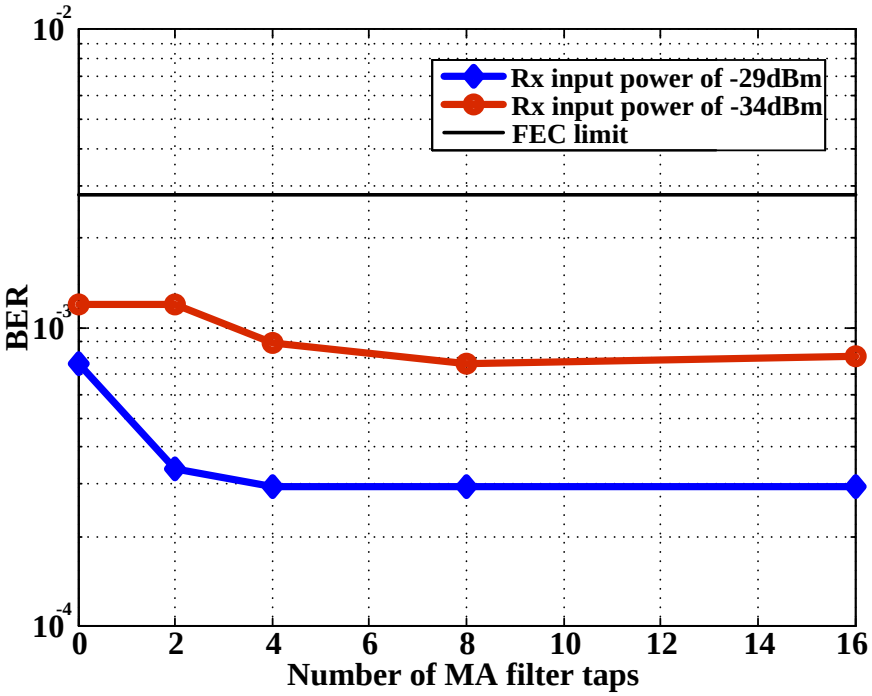

Figure 3.24. Experimental BER versus the number of MA filter taps.

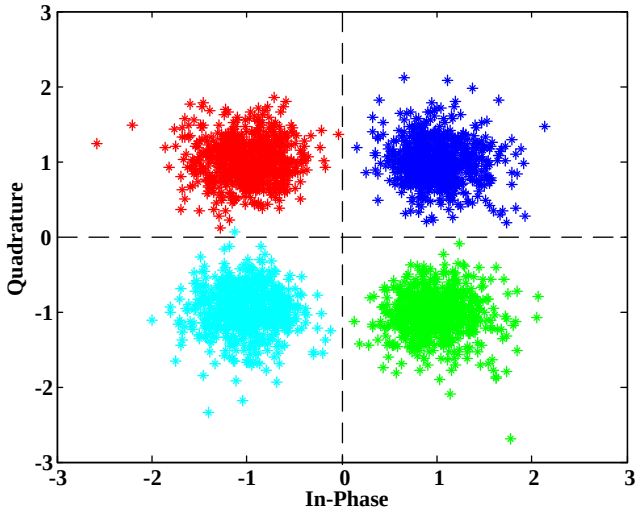

Figure 3.25. 4-QAM constellation after compensated for CFO.

Finally, the 4-QAM constellation at the Rx input power of –29 dBm is shown in Figure 3.25. The constellation points are not rotated and this means that CFO is cancelled.

CHAPTER 4

Optical Channel Compensation and ISI Tolerance of the Cyclic Prefix Free OFDM

4.1 Introduction

This chapter addresses another important technique which is necessary for the function of OFDM communication systems, i.e. the optical channel impairment compensation. Both chromatic dispersion (CD) and random phase noise (PN) are considered in this dissertation, and they are compensated simultaneously. CD leads directly to intersymbol interference (ISI) when the cyclic prefix (CP) is not long enough, and PN directly creates intercarrier interference (ICI). Both degrade system performance. However, for long communication links, the accumulated CD becomes very large. Thus, a large CP is required, which may reduce the effective data rate andthe PN would become a more serious problem. Therefore, to address this issue, CP-free OFDM is investigated. However, ISI compensation must be employed on. To combat ISI, half and full window functions are investigated, as detailed and discussed in this chapter.

For channel equalization, generally, information from the transmitter side can facilitate channel estimation and compensation. Therefore, in this dissertation, the pilot-aided method is considered by distributed insertion of the known pilot data into some of the subcarriers to each OFDM symbol. At the receiver end, after OFDM frame synchronization and conversion back to the frequency domain, optical channel effect compensation follows. The compensation unit is called one-tap equalization, and it is the unit of consideration in this chapter, as shown in the gray block in Figure 4.1.

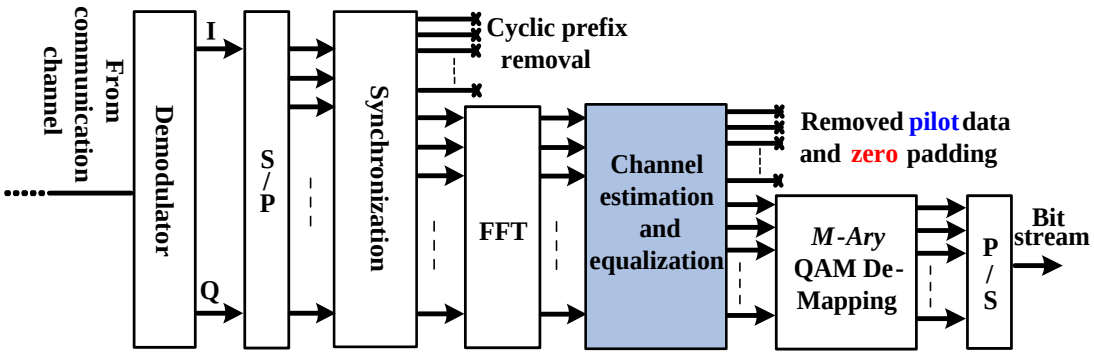

Figure 4.1. The considered part of the receiver block considered in this chapter.

4.2. Phase rotation due to CD and PN

The received time domain sample data distorted by PN and CD can be modeled in the time domain by

$$y(n) = \left(x(n) \otimes h(n)\right) pn(n) + \tilde{z}(n), \tag{4.1}$$

or in the frequency domain by [62]

$$\begin{aligned} Y(k) &= \sum_{p=0}^{N_C-1} X(k)H(k)PN(k-p) + \tilde{Z}(k) \\ &= X(k)H(k)PN(0) + \sum_{p=0, p\neq k}^{N_C-1} X(p)H(p)PN(k-p) + \tilde{Z}(k) \end{aligned}, \tag{4.2}$$

where $\otimes$ is the convolution operator and the capital letter represents frequency domain and lower-case indicates time domain. $y(n)$ and $Y(k)$ are the received samples, $x(n)$ and $X(k)$ are the constellation mappings. $pn(n)$ and $PN(k)$ are the random phase noise. According to Equation 2.23, $pn(n) = e^{j\psi_n}$ which is generated by a Wiener random process with a zero mean and a fluctuation that depends on the variance $\sigma = \sqrt{2\pi\Delta\nu T_s}$. The relation of $PN(k)$ and $pn(n)$ can be expressed by [62]

$$PN(k) = \frac{1}{N_C}\sum_{n=0}^{N_C-1} pn(n)e^{-j2\pi nk/N_C} = \frac{1}{N_C}\sum_{n=0}^{N_C-1} e^{j\Psi_n}e^{-j2\pi nk/N_C}. \quad (4.3)$$

When there is no phase noise, $\sigma = 0$ and $PN(k)$ becomes $\delta(k)$. $\delta(k)$ is the Kronecker delta function, $\delta(k) = \begin{cases} 0, & k \neq 0 \\ 1, & k = 0 \end{cases}$. Therefore, the second term of Equation (4.2) will be disappeared and the first term becomes $Y(k) = X(k)H(k)$. In case of $PN(0)$, it is called the common phase error term which affects every subcarrier [62]. $PN(0)$ is given by

$$PN(0) = \frac{1}{N_C}\sum_{n=0}^{N_C-1} e^{\Psi_n}. \quad (4.4)$$

Finally, $\tilde{z}(n)$ and $\tilde{Z}(k)$ are the ASE noise at the *n*th time domain sample and the *k*th subcarrier, respectively.

Hence, due to the consideration of only one optical polarization channel, only the CD is considered in this work. The transfer function of CD in the frequency domain can be obtained by [63]

$$H(k) = e^{j\frac{\pi cDL}{f_{cf}^2}f_k^2}, \quad (4.5)$$

where D is the CD coefficient, L is the length of the fiber, f_k is the frequency of the *k*th subcarrier, and f_{cf} is the optical center frequency used for the transmitter and receiver. Then, examples of the phase responses of various fiber lengths are shown in Figure 4.2.

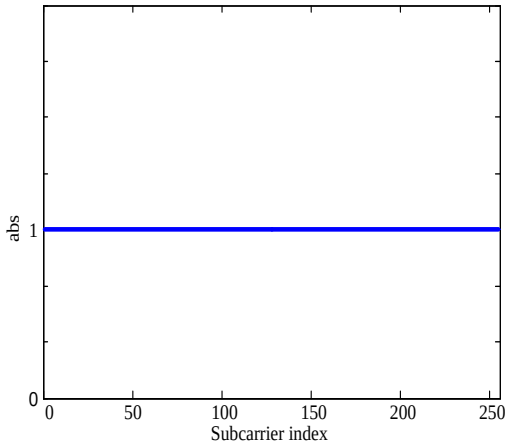

A: Magnitude for all the length of cable.

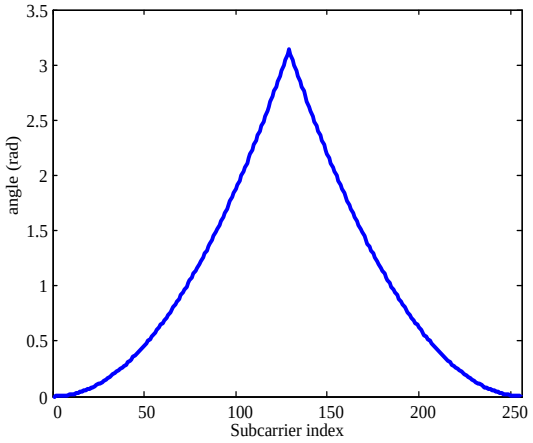

B: Fiber length of 80 km (1 span).

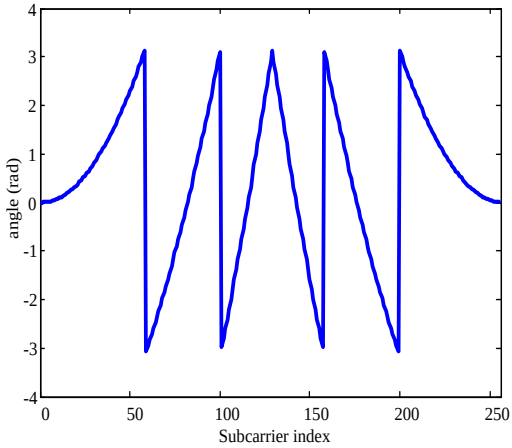

C: Fiber length of 400 km (5 spans).

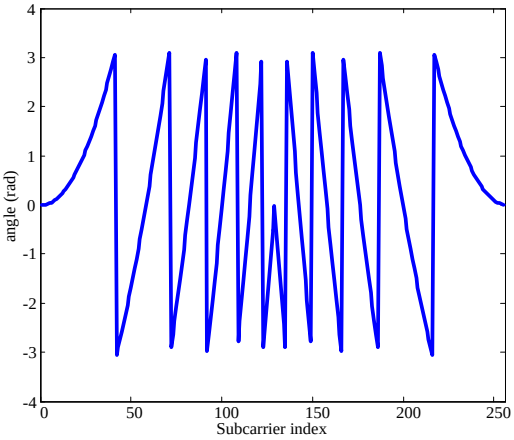

D: Fiber length of 800 km (10 spans).

Figure 4.2. The angle rotation in radians with various fiber lengths.

Figure 4.2 plots the phase response of each subcarrier in the frequency domain, where the sampling rate is 20 Gs/s, FFT size is 256, and CD coefficient is 16 *ps/(nm·km)*. The magnitude of the transfer function is the same for all fiber lengths as shown in Figure 4.2A. The rotating phasor for the fiber lengths of 80 km, 400 km, and 800 km are presented in Figures 4.2B–4.2D. It is shown that the longer cable causes more fluctuated phase rotation and it rotated within $-\pi$ to π.

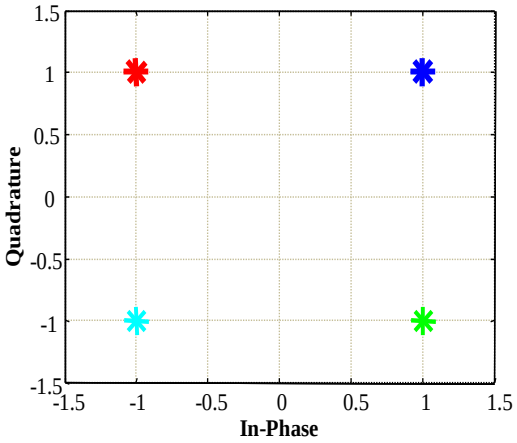

A: No CD effect.

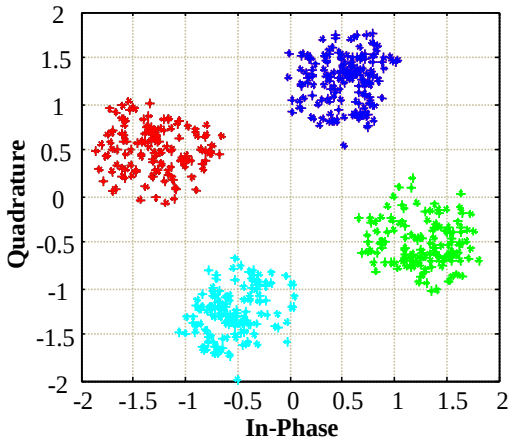

B: Fiber length of 80 km (1 span).

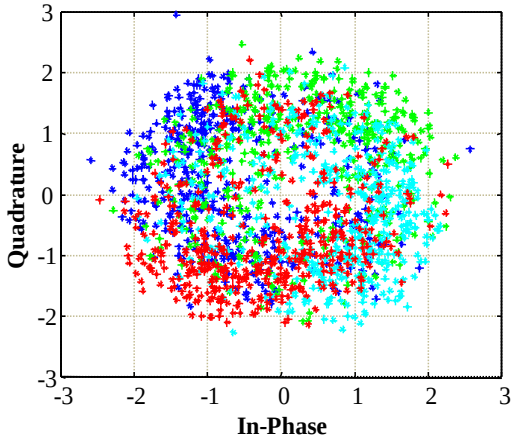

C: Fiber length of 400 km (5 spans).

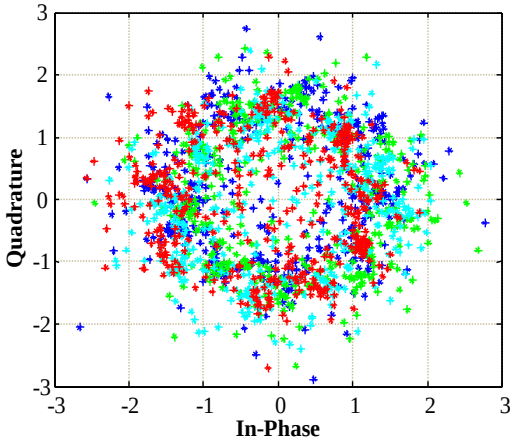

D: Fiber length of 800 km (10 spans).

Figure 4.3. The 4-QAM constellation distorted by CD for various fiber lengths.

Figure 4.3 plots the 4-QAM constellation after demodulating OFDM symbols, which are distorted due to CD, the IFFT/FFT size is 256, and CP has 32 samples, and 128 zeros are inserted onto the subcarriers around the middle of IFFT input for oversampling at the transmitter. The laser linewidth $\Delta\nu = 100$ kHz is used. The sampling rate and other parameters are the same as in Figure 4.2, but the ASE noise is still not considered. Figure 4.3A shows the original correct constellation diagram position, where the data points are located in 4 quadrants of the complex plane. From Figure 4.3B to Figure 4.3D, it can clearly be seen that the phase and amplitude are

distorted. For80 km, the degradation is insignificant. However, for 400 km and 800 km, the demodulated symbol produces many phases and amplitudes which are distributed over the whole complex plane.

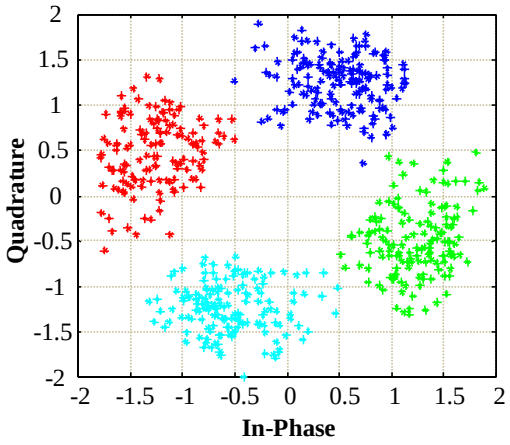

A: Laser linewidth of 100 kHz.

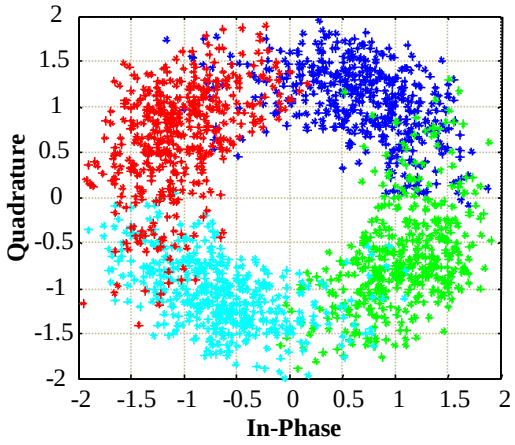

B: Laser linewidth of 500 kHz.

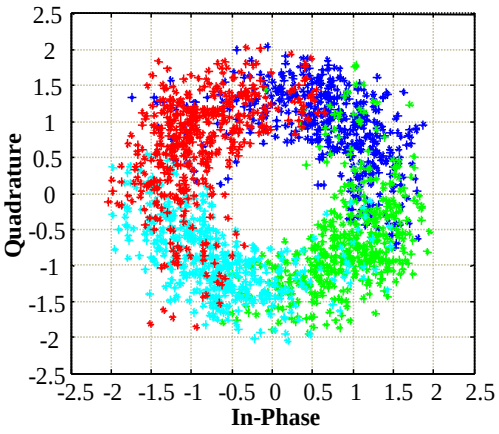

C: Laser linewidth of 1000 kHz.

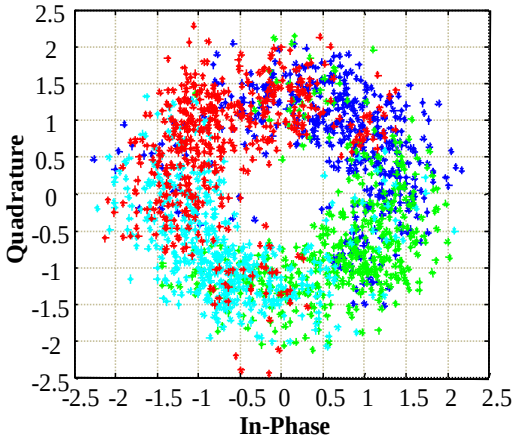

D: Laser linewidth of 2000 kHz.

Figure 4.4. The 4-QAM constellation destroyed by various PN.

Figure 4.4 shows the 4-QAM constellation in which the OFDM symbols are distorted only by PN, where a sampling rate of 10 Gs/s and an FFT size of 256 are used. Laser linewidths of 100 kHz, 500 kHz, 1000 kHz and 2000 kHz are considered. The fiber length of 80 km is used. Again, the ASE noise is not considered.. From Figure 4.4A to Figure 4.4D, it can be seen that phase and amplitude are distorted due

to the PN, constellation diagram also produces many phases and amplitudes but these results are not distributed to the whole complex plane.

4.3. Channel estimation and equalization

As already noted, both CD and PN degrade the system performance. Thus, the channel coefficient must be estimated and compensated to recover the information signal. There are two main schemes for this: blind channel estimation (BCE) and pilot-aided channel estimation (PCE). For BCE, some statistical information of the optical channels is required and must be precalculated. Additionally, the computations are highly complex, as proposed in [64-66]. Consequently, in this thesis, the PCE is used because it has lower complexity and outperforms the BCE. However, it loses some pilot data or bandwidth for learning the channel coefficient, as explained in the next section. The information data refers to a transmitted constellation point in the complex plane, which is mapped from the input bit stream. The pilot data is the known constellation mapping.

4.3.1 Pilot insertion technique

In the pilot insertion technique, the known data are inserted into various subcarriers of each OFDM symbol in the frequency domain at the transmitter part. The pilot can be inserted in two ways: the pilot is inserted into a non-rotation subcarrier index scheme or into a rotation subcarrier index scheme. The former is simpler and used in this dissertation. There are two types, called the Block type and Comb type [68-69], as shown in Figures 4.5 and 4.6, respectively.

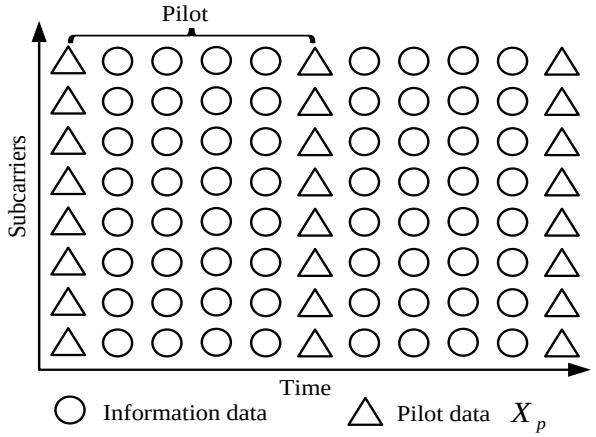

Figure 4.5. The Block type pilot insertion.

For the Block type (or time type), certain special OFDM symbols are used as pilot symbol. All subcarriers are modulated by known symbols, and no information data are transmitted within symbol. It is called the pilot OFDM symbol. Then, it is followed by some useful symbols, in which all subcarriers are modulated by useful information data. The information data are called information OFDM symbols. Normally, the OFDM pilot symbols are inserted uniformly between information OFDM symbols, for example every 10, 50, or 100 useful symbols. Obviously, if the channel response changes in the pilot symbol period, then the system cannot update or track the channel coefficients corresponding to the information OFDM symbols. Consequently, this type would not be appropriate. In particular, when large FFT size is considered, the OFDM symbol is increased in length. Therefore, the pilot symbol duration is also long which causes the channel response to be changed within the pilot symbol period. However, this type is widely used for learning optical communication channels [5-6, 10].

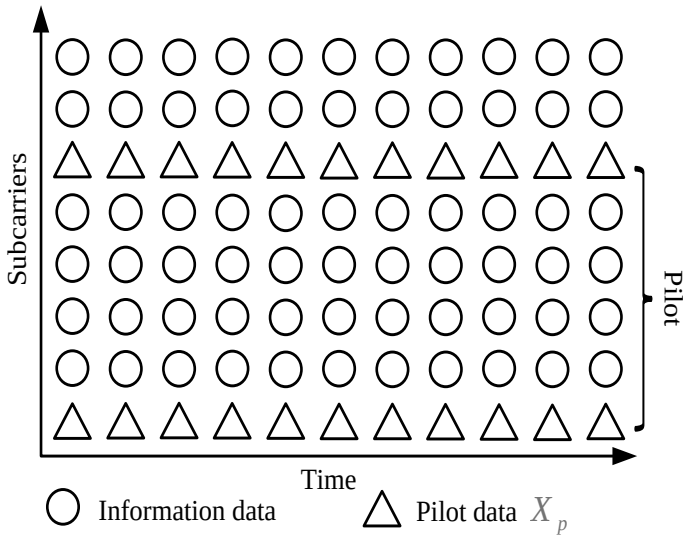

Figure 4.6. The Comb type pilot insertion.

For the Comb type (or frequency type), the known pilots and useful information data are combined together in each OFDM symbol. The pilot data are inserted uniformly in every symbol, such as at every 8, 16, 32 subcarriers. In Figure 4.6, the pilots are added at every 4 data symbol. In each symbol, both are located at a certain position in every OFDM symbol.

Obviously, this technique can be used to update the channel coefficients in a symbol-by-symbol manner without depending on the FFT size because the pilots are inserted at a certain subcarrier in every symbol. For a frequency-selective channel impact, such as the PMD effect discussed in Chapter 2, the Comb approach may not be suitable. However, if the pilot data are inserted closely enough between the subcarriers, the desired result should still be achieved. In addition, the Comb type can also compensate for both CD and PN simultaneously and can be traced symbol by symbol.

The lattice type is a combination of the two previous schemes, developed by inserting the pilots both in the Comp and Block types, as shown in Figure 4.7. In every OFDM symbol, the pilot insertion is shifted by a fixed length, although the pilot duration between the information data is not changed. Hence, if the channel response is slow enough and the estimated data from the pilot can be saved from every symbol, the channel response of all subcarriers can be estimated perfectly. This would enable it to keep track of the time-varying and frequency-selective channel impacts. However, this gives rise to a very complex system.

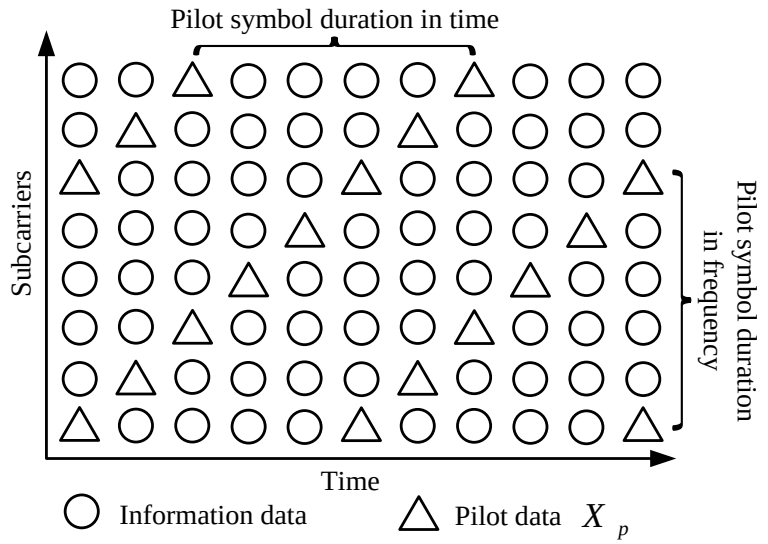

Figure 4.7. The lattice type pilot insertion.

To track the channel coefficient and obtain a simple implementation, the Comb-type approach is used in this thesis. The pilot data subcarrier indexes and the information data subcarrier indexes can be combined together. The pilot and useful

information are set into a group, and each OFDM symbol contains many groups, where each group can be expressed by [68]

$$X(k) = X(mL + l) = \begin{cases} X_p(m) & ,l = 0 \\ information\ data & ,l = 1...L-1 \end{cases}, \tag{4.6}$$

where X is the data, which can be either pilot or information data (useful data) in each *k*th subcarrier index. X_p is the pilot data. L is the pilot duration length between the information data and $m = 0...L-1$ is the subcarrier index in each group of information data and pilot data.

For clear understanding, an example of pilot and information data position for each OFDM symbol is given. The parameters for the following example are set: $N_C = 16$ and $L = 4$. Hence, N_p is $16/4 = 4$, $l = 0...3$, and $m = 0...3$. From Figure 4.6 and Equation (4.4), an example of the pilot and information data position in each OFDM symbol can be determined from Figure 4.8.

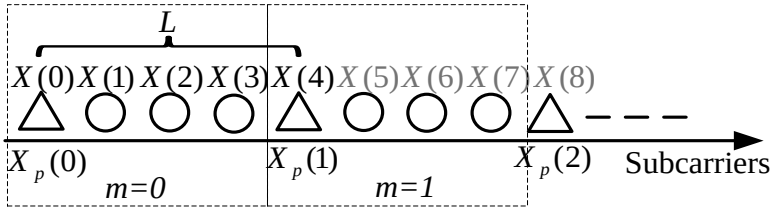

Figure 4.8. An example of pilot data and information data location in an OFDM symbol.

4.3.2. Estimation and compensation of channel coefficients

The estimation and equalization of channel distortions at the receiver are detailed in this section. Many techniques are used for this purpose, including least-square (LS) [49], least-mean-square error (LMSE) [49], and minimum-mean-square-error (MMSE) [48]. However, the LMSE and MMSE must know the actual channel statistics to carry out the mean error computations. Such an action is either impossible or very difficult to implement in practice. Therefore, in this dissertation, the LS is considered because it is simple to implement in terms of hardware. The LS method

identifies the channel coefficients, $\hat{\mathbf{H}}$, that minimizes the cost function, as expressed by [49]

$$\begin{aligned} J(\hat{\mathbf{H}}) &= \left\| \mathbf{Y} - \mathbf{X}\hat{\mathbf{H}} \right\|^2 \\ &= (\mathbf{Y} - \mathbf{X}\hat{\mathbf{H}})^H (\mathbf{Y} - \mathbf{X}\hat{\mathbf{H}}) \\ &= \mathbf{Y}^H\mathbf{Y} - \mathbf{Y}^H\mathbf{X}\hat{\mathbf{H}} - \hat{\mathbf{H}}^H\mathbf{X}^H\mathbf{Y} + \hat{\mathbf{H}}^H\mathbf{X}^H\mathbf{X}\hat{\mathbf{H}} \end{aligned} \tag{4.7}$$

where $\|\cdot\|$ is the norm operator and $(\cdot)^H$ is the Hermitian transpose. For simplicity, the subcarrier index indicator is dropped in Equation (4.5) and a bold font is used to indicate the matrix and vector quantity instead. Hence, $\mathbf{Y} = \mathbf{XH}$ where $\mathbf{X}$ is the constellation mapping which can be defined by a diagonal matrix

$$\mathbf{X} = \begin{bmatrix} X(0) & 0 & \cdots & 0 \\ 0 & X(1) & & \vdots \\ \vdots & & \ddots & 0 \\ 0 & \cdots & 0 & X(N_p - 1) \end{bmatrix}, \tag{4.8}$$

where N_P is the number of pilot subcarriers used in each OFDM symbol and $\hat{\mathbf{H}} = \left[\hat{H}(0) \quad \hat{H}(1) \quad \hat{H}(2) \quad \ldots \quad \hat{H}(N_P - 1)\right]^T$ is a vector of channel coefficients. $\mathbf{Y} = \left[Y(0) \quad Y(1) \quad Y(2) \quad \ldots \quad Y(N_P - 1)\right]^T$ is a received signal vector. From Equation (4.5), since $\mathbf{X}$ is diagonal matrix and by ordinary matrix multiplication, the flowinging are obtained by,

$$\mathbf{Y}^H\mathbf{Y} = \left(\mathbf{Y}^*\right)^T\mathbf{Y} = \sum_{k=0}^{N_P-1} Y^*(k)Y(k), \tag{4.9A}$$

$$\mathbf{Y}^H\mathbf{X}\hat{\mathbf{H}} = \left(\mathbf{Y}^*\right)^T\mathbf{X}\hat{\mathbf{H}} = \sum_{k=0}^{N_P-1} Y^*(k)X(k)\hat{H}(k), \tag{4.9B}$$

$$\hat{\mathbf{H}}^H\mathbf{X}^H\mathbf{Y} = \left(\hat{\mathbf{H}}^*\right)^T\left(\mathbf{X}^*\right)^T\mathbf{Y} = \sum_{k=0}^{N_P-1} \hat{H}^*(k)X^*(k)Y(k), \tag{4.9C}$$

$$\hat{\mathbf{H}}^H\mathbf{X}^H\mathbf{X}\hat{\mathbf{H}} = \left(\hat{\mathbf{H}}^*\right)^T\left(\mathbf{X}^*\right)^T\mathbf{X}\hat{\mathbf{H}} = \sum_{k=0}^{N_P-1} \hat{H}^*(k)X^*(k)X(k)\hat{H}(k). \tag{4.9D}$$

By combining Equations (4.9A) to (4.9D), $J(\hat{\mathbf{H}})$ can be given by

$$J(\hat{\mathbf{H}}) = \sum_{k=0}^{N_p-1}\Big(Y^*(k)Y(k) - Y^*(k)X(k)\hat{H}(k) - \hat{H}^*(k)X(k)^*Y(k) + \hat{H}^*(k)X^*(k)X(k)\hat{H}(k)\Big). \tag{4.10}$$

Then, the next step is to take the derivative of Equation (4.10) with respect to $\hat{H}(k)$, followed by setting the derivative equal to zero, given as

$$\begin{aligned}\frac{\partial J(\hat{\mathbf{H}})}{\partial(\hat{H}(k))} &= 0 - Y^*(k)X(k) - 0 + \hat{H}^*(k)X^*(k)X(k) = 0 \\ &= -Y(k) + \hat{H}(k)X(k) = 0.\end{aligned} \tag{4.11}$$

Finally, the LS channel estimation for each subcarrier developed using the LS method is [49, 68]

$$\hat{H}(k) = Y(k)X(k)^{-1}. \tag{4.12}$$

Here, we can see that if $Y(k)$ is the received *k*th subcarrier that contains pilot data and $X(k) = X_p$, the optical channel coefficients can be extracted using the pilot aided method by Equation (4.10).

4.3.2.1 Interpolation method

Reconnecting to the Comb-type pilot insertion, $\hat{H}_p$, is available only for the subcarriers containing the known pilot data and not for the subcarriers containing the useful information data. Therefore, all subcarriers that contain useful information must be also estimated. This is achieved by interpolation. In this dissertation focuses on two schemes, namely, linear interpolation (LI) (first order interpolation) and non-linear interpolation (NLI) (second order interpolation). The LI method can be expressed as [68-69]

$$\hat{H}(k) = \hat{H}(mL + l) = \big(\hat{H}_p(m+1) - \hat{H}_p(m)\big)\frac{l}{L} + \hat{H}_p(m), \tag{4.13}$$

where $l = 0 \ldots L - 1$. Alternatively, NLI can be given by

$$\hat{H}(k) = \hat{H}(mL + l) = c_1 \hat{H}_p(m-1) + c_0 \hat{H}_p(m) + c_{-1} \hat{H}_p(m+1), \tag{4.14}$$

where

$$c_1 = \frac{1}{2}\left[\left(\frac{l}{L}\right)^2 + \left(\frac{l}{L}\right)\right], \tag{4.15}$$

$$c_0 = 1 - \left(\frac{l}{L}\right)^2, \tag{4.16}$$

$$c_{-1} = \frac{1}{2}\left[\left(\frac{l}{L}\right)^2 - \left(\frac{l}{L}\right)\right]. \tag{4.17}$$

The linear and second order interpolation method interpolate the estimated optical channel coefficients from LS method between $\hat{H}(m)$ and $\hat{H}(m+1)$. The linear interpolation gives only a straight line between them while the second order gives a smooth asymmetrical curve. Another interesting interpolation is cubic spline interpolation which can give a smoother curve than those two methods owing to the existence of the first order and the second order derivative in calculation process at each data point [69-70]. Therefore, it is more complicated to implement in hardware when compared with the linear and second order interpolation and is beyond the scope of this dissertation. Figure 4.9 shows an example of the three interpolation methods.

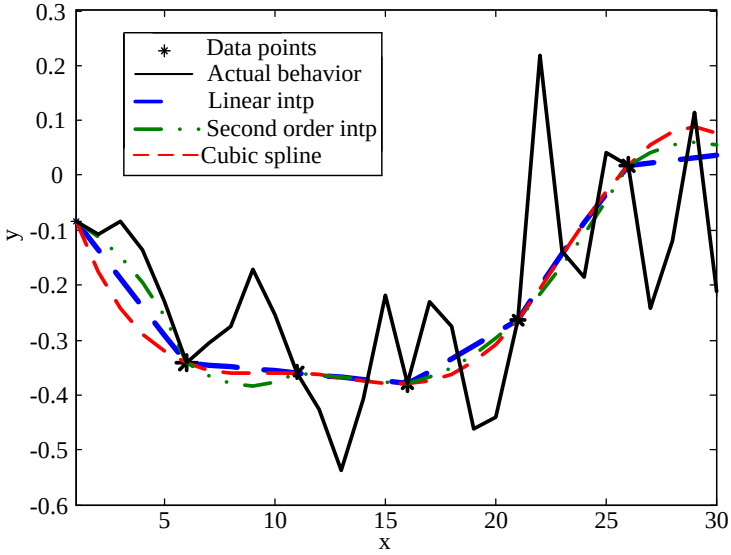

Figure 4.9. An example of interoperated curve by various interpolation methods.

As can be seen in Figure 4.9, each interpolated curve shows different tracking of the actual behavior such that its performance can be measured by calculating the mean square error (MSE) [70], given by

$$MSE = \frac{1}{M}\sum_{i=1}^{M}\left(\hat{E}_i - E_i\right)^2, \tag{4.18}$$

where M is the length of data, $\hat{E}_i$ is the interpolated data and E is the actual behavior data. The MSE performances are shown in Table 4.1.

Table 4.1. Comparison MSE of Figure 4.9

	Linear interpolation	Second order interpolation	Cubic spline interpolation
MSE	0.0184	0.0215	0.0198

From Table 4.1 it can be seen that the linear interpolation method gives the best MSE. However, different actual behavior may gives different MSE performance on each interpolation method. Therefore, each interpolation method may have suboptimum performance for different optical channel effect as shown in Figure 4.16.

Finally, to recover the information data back, the estimated channel $\hat{H}(k)$ must be applied to the received OFDM symbol to mitigate the optical channel effect, which is given by

$$\hat{X}(k) = \frac{Y(k)}{\hat{H}(k)} = \frac{X(k)H(k)}{\hat{H}(k)} + \frac{\tilde{Z}(k)}{\hat{H}(k)}. \tag{4.19}$$

From Equation (4.19), if $\hat{H}(k)$ is perfectly estimated, the accuracy of $\hat{X}$ is dependent on the noise power.

4.3.2.2 Common phase error method

The common phase error (CPE) [9-10] method is widely used for phase estimation and compensation. According to known pilot insertion, which is also inserted similar to Comb type, as discussed in Sections 4.3.1 and 4.3.2.2, the calculation phase error for the CPE method is given by [9-10, 12]

$$\hat{H}_{CPE} = \frac{1}{N_P} \sum_{k=1}^{N_P} \left(\angle Y_P(k) - \angle X_P(k) \right), \tag{4.20}$$

where $\angle$ is the phase angle operator, $Y_P(k)$ is the received pilot data on the *k*th subcarrier, $X_P(k)$ is the known pilot data on the *k*th subcarrier, and N_P is the number of pilot, $_P$, subcarriers used in each OFDM symbol. Finally, the compensation for phase rotation of the received useful information data for each *k*th subcarrier is given as

$$\hat{X}(k) = Y(k)\hat{H}^*_{CPE}, \qquad k = 1,..., N_C. \tag{4.21}$$

4.3.3. Experimental setup of channel compensation

Figure 4.10 shows an experimental setup for optical channel compensation of the self-homodyne CO-OFDM, which is the same as that described in Chapter 3. The blue box is considered in this chapter.

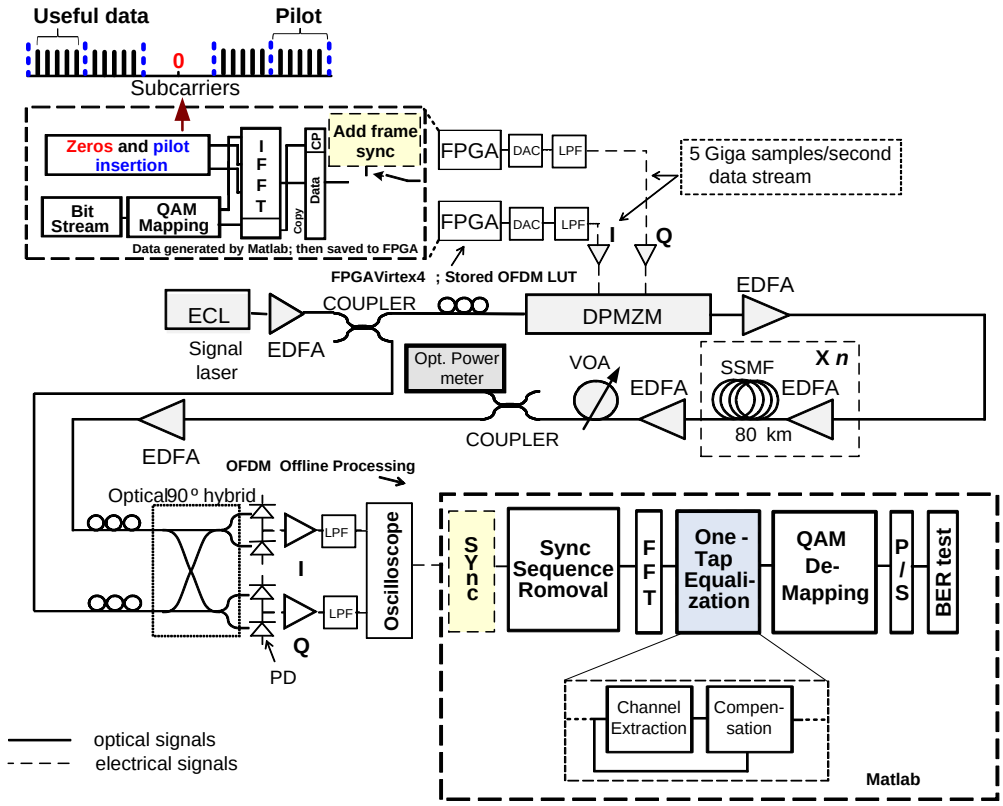

Figure 4.10. The experimental setup for channel compensation of CO-OFDM.

Again, at the transmitter end, the OFDM data are preprocessed in Matlab and then stored in two synchronized Virtex-4 FPGAs for I and Q. The OFDM frame is generated, consisting of 32 training sequence (TS) (OCS symbol) samples for frame synchronization, followed by 167 OFDM symbols. In one OFDM symbol, each subcarrier is modulated by 4-QAM. 128 subcarriers around the center of the spectrum are modulated with zeros for oversampling. The pilot data are inserted at each 16th position in the information data.

The digital samples from the two FPGAs are converted to the analog domain using two Micram digital-to-analog converters at 5 Gs/s (200 ps) with a resolution of 6 bits. Therefore, each OFDM symbol length is 57,600 ps (288 × 200 ps). For E/O conversion, a Dual-Parallel Mach-Zehnder Modulator (DPMZM) is used to modulate the 1550 nm light of an external cavity laser (ECL) with a specified linewidth of approximately 150 kHz. Then, the light is transmitted over a standard single mode

fiber. For each fiber span, the signal is amplified by the EDFA in between. Additionally, for each fiber span, the launch power is –3 dBm.

At the receiver end, the signal is attenuated by a variable optical attenuator (VOA) followed by an EDFA. The polarization between transmitter and receiver is controlled manually. The received signal is demodulated by a 90° optical hybrid. Two differential photodiode pairs convert the optical signals into electrical signals (O/E). The received I and Q signals are sampled and stored by an oscilloscope (TDS6804B) for subsequent offline processing.

Inside the offline processing unit, for recovering the information, the OFDM frames are synchronized by the method discussed in Chapter 3. Then, the QCS and CP are removed. The channel effects are mitigate, mainly including the CD and PN, which are cancelled in the frequency domain, after the FFT, by following Equations (4.10)–(4.15). Finally, the 4-QAM de-mapping and bit error ratio (BER) calculation steps are performed, where the BER is shown in the next section.

4.3.4. Experimental results of channel compensation

To confirm the proposed methods, the experimental results are shown in this section. Figure 4.11 plots a comparison of the BER of the OFDM signal after passing 320 km. SSMF is used for all three methods of error compensation. With a pilot after every 16 useful data subcarriers, the proposed methods clearly outperform CPE. In addition, the first order interpolation gives better BER than the second order interpolation. As an example, for Rx input power of –24 dBm, a BER of $3.2 \cdot 10^{-5}$ can be achieved for the first order interpolation, $4.5 \cdot 10^{-4}$ for second order interpolation, and $4.8 \cdot 10^{-2}$ for the CPE method.

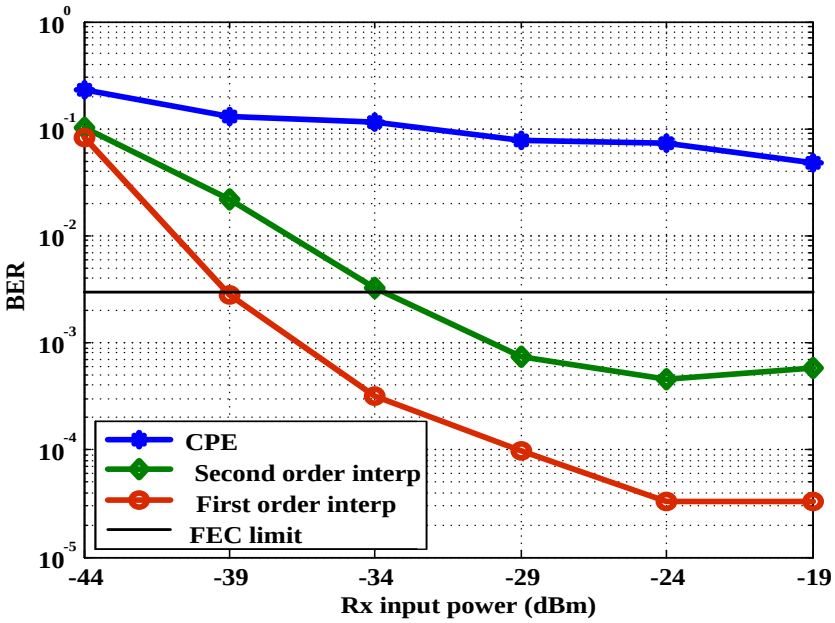

Figure 4.11. BER comparison of the various estimated phase methods.

Figure 4.12 shows the reason that the second order interpolation and the CPE method give less favorable BER. We can see that some points of the interpolated phase error between the two adjacent pilot data by the second order (green line) cannot be traced through the middle of the phase error fluctuation angle (blue line) and some points of that is far away. In addition, the second order interpolation curve is smooth and asymmetric while error phase fluctuation on Figure 4.12 is sharp and fast, so it would be a reason of worse BER for short transmission lengths but in case of long-haul transmission it would give better BER as shown in Figure 4.16.

For the CPE method, the maximum likelihood (MLH) [10] (please refer to Section 4.3.2.2) of the estimated angle is calculated from all the pilot data, and the result gives the mean value (yellow line). In addition, it is used for compensating all the subcarriers. Consequently, the estimated phase for both methods is far from the true phase angle.

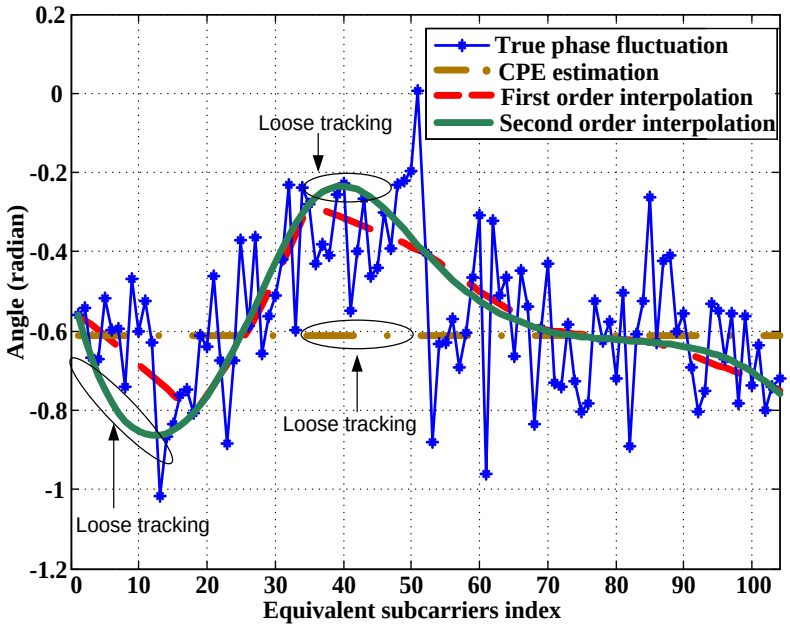

Figure 4.12. A comparison of the phase fluctuation tracking for the various estimation approaches.

Next, Figure 4.13 shows a comparison of the BER in terms of fiber length. The lengths of 160 km and 320 km are shown. A BER of $1.6 \cdot 10^{-6}$ can be achieved for 160 km, while a value of $3.2 \cdot 10^{-5}$ is obtained for 320 km.

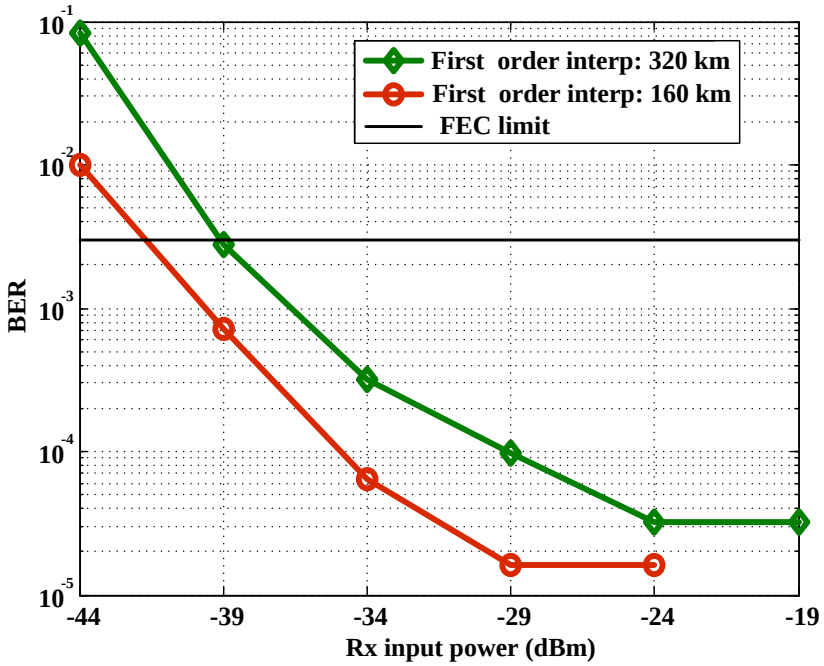

Figure 4.13. A comparison of the BER in terms of the optical fiber length for linear interpolation (first order interpolation).

Next, Figures 4.14 and 4.15 show the 4-QAM constellations at the receiver without and with phase compensation at the Rx input power at −19 dBm and −34 dBm for 160 km and 320 km, respectively.

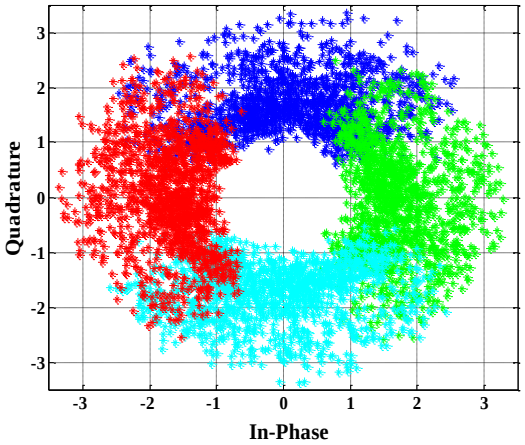

A: Without compensation at an Rx input power of −19 dBm

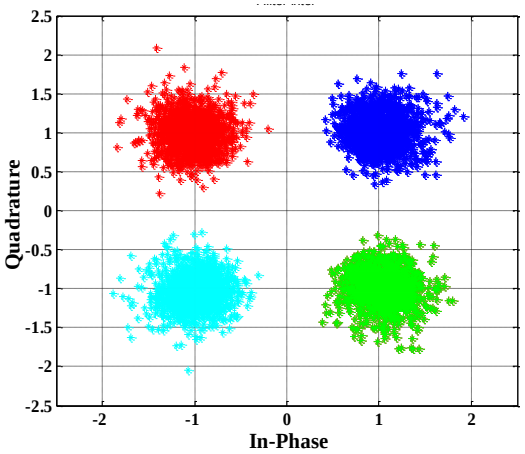

B: With compensation at an Rx input power of −19 dBm

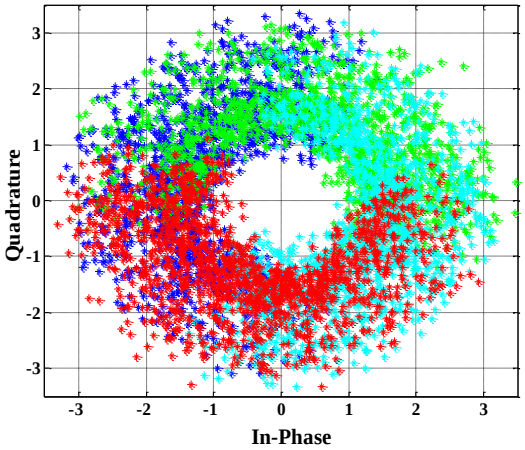

C: Without compensation at an Rx input power of −34 dBm

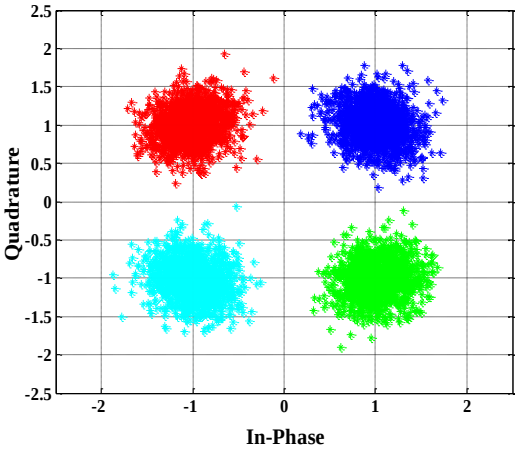

D: With compensation at an Rx input power of −34 dBm

Figure 4.14. The 4-QAM constellations without and with compensation for the channel effect at 160 km of fiber length.

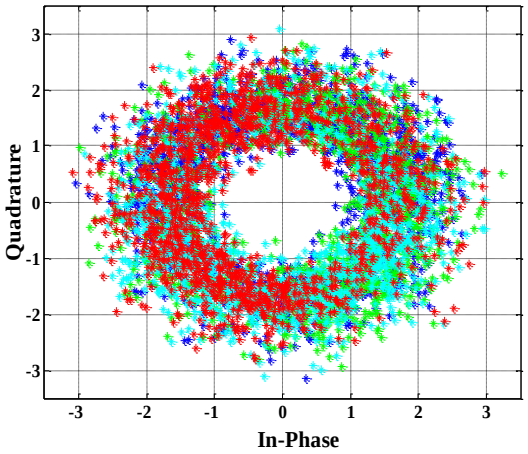

A: Without compensation at an Rx input power of –19 dBm

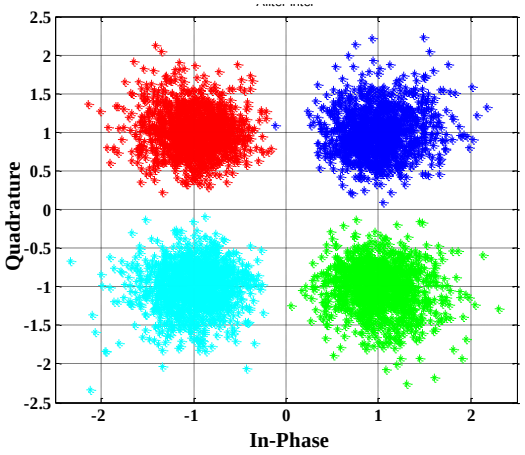

B: With compensation at an Rx input power of –19 dBm

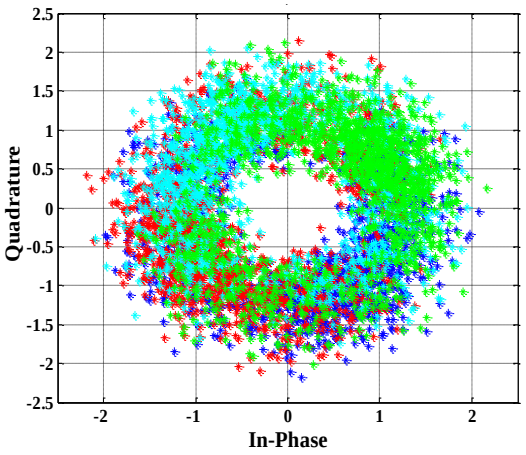

C: Without compensation at an Rx input power of –34 dBm

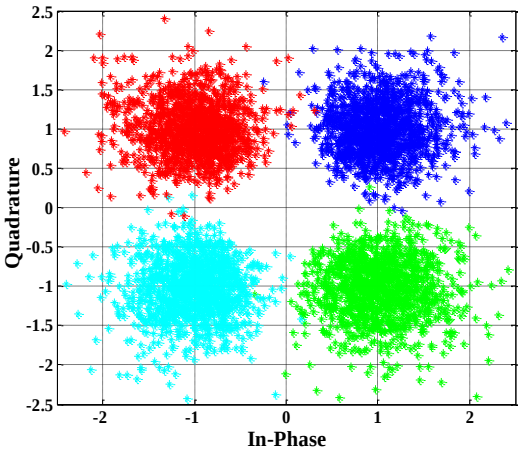

A: With compensation at an Rx input power of –34 dBm

Figure 4.15. The 4-QAM constellations with and without compensation for the channel effect at 320 km of fiber length.

From Figures 4.14 and 4.15, it can be confirmed that the channel effect is compensated for both 160 km and 320 km of fiber length. The constellation is not rotated or distributed over the complex plane. However, owing to the higher ASE noise, the constellation points increase in size.

However, due to the limitation of the experimental setup, we extend the investigation by using a simulation method. The sampling rate is increased up to 28 Gs/s, the laser linewidth is 200 kHz, and the optical signal to noise ratio (OSNR) is 25 dB. We vary the length of the fiber, which is represented by the number of spans. Each span consists of 80 km SSMF with a CD coefficient of 17 *ps/(mn·km)*.

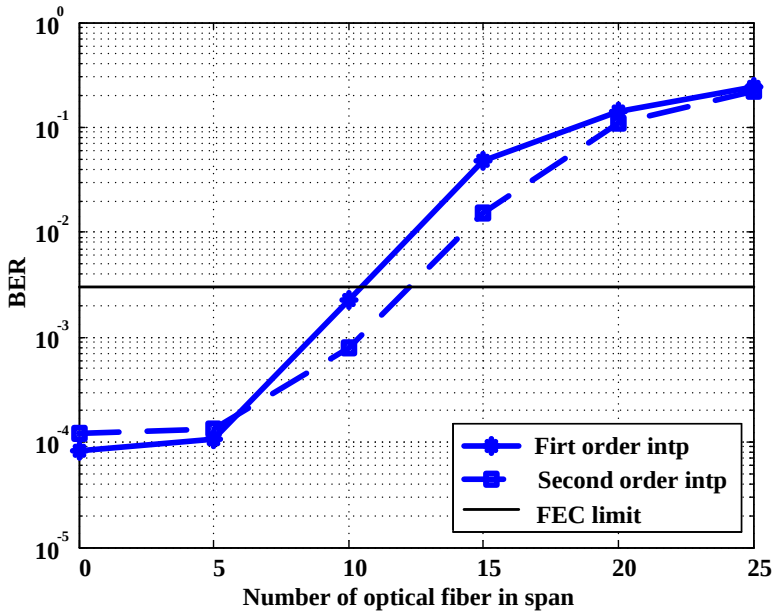

Figure 4.16. BER comparison of the various estimated phase methods for various optical fiber length.

Figure 4.16 shows the BER results over several numbers of spans where 16-QAM is used. At the forward error correction (FEC) limit, a fiber length of 1040 km (13 spans) can be achieved for second order interpolation method. It is also observed that the second order interpolation gives better BER when the cable is longer than 5 spans, because the second order interpolation can be better fitted to the phase rotation from CD. On the other hand, when the cable is shorter than 5 spans, the curve of the phase rotation is low so that the second order interpolation loses tracking. Therefore, the linear interpolation gives better BER.

4.4 Interference tolerance of the cyclic-prefix-free OFDM symbol

Generally, owing to the dispersive channel, the CD effect in particular results in overlapped and added OFDM symbols. Thus, ISI occurs for CP-free OFDM symbols, as show in an example in Figure 4.17.

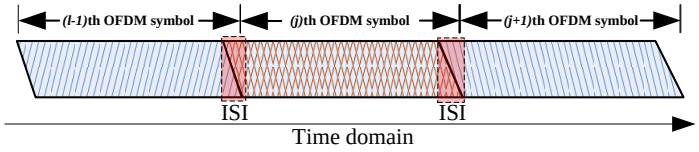

Figure 4.17. The ISI behavior of the CP-free OFDM communication in the time domain.

Therefore, to get rid of the ISI effect, we propose a window function with an exponential decay at one side and at both sides of each OFDM symbol. The window function for the one side is given by [72]

$$g_{half}(n)=\begin{cases}\frac{1}{2}\left(1-\cos\left(\pi n/w\right)\right), & 1<n\le w\\ 1 \quad , & w<n\le N_C,\\ 0 \quad , & otherwise\end{cases} \tag{4.22}$$

and this is called half windowing, where w is the window size. Full window function (both sides of each OFDM symbol) is given by [73-74]

$$g_{full}(n)=\begin{cases}\frac{1}{2}\left(1-\cos\left(\pi n/w\right)\right) \quad , & 1<n\le w\\ 1 \quad , & w<n\le N_C-w\\ \frac{1}{2}\left(1+\cos\left(2\pi-\pi n/w\right)\right), & N_C-w<n<N_C\\ 0 \quad , & otherwise.\end{cases} \tag{4.23}$$

The example for $w=16$ is shown in Figure 4.18.

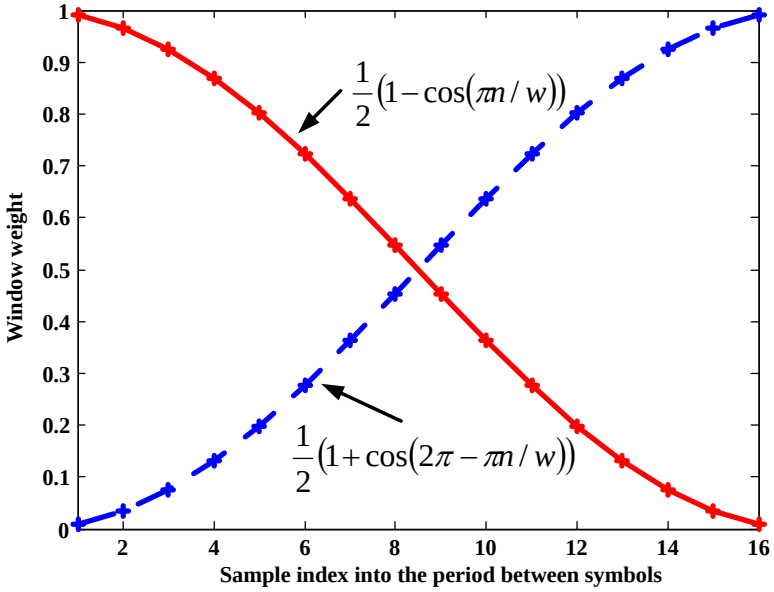

Figure 4.18. Illustration of the window function decay curve when $w=16$ is used.

After windowing using the half window function, each OFDM will look similar to Figure 4.19,

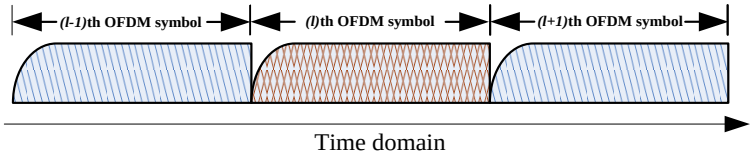

Figure 4.19. The half window scheme for each OFDM symbol at the transmitter.

and the case for full windowing scheme is shown in Figure 4.20.

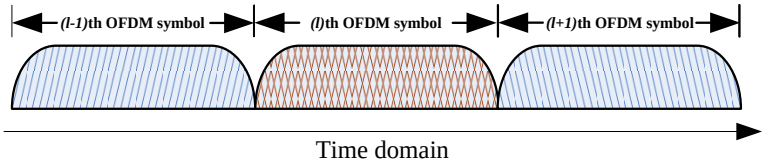

Figure 4.20. The full window scheme for each OFDM symbol at the transmitter.

Then the windowed OFDM symbols are transmitted through the channel, and the received signal would look similar to the image in Figure 4.21.

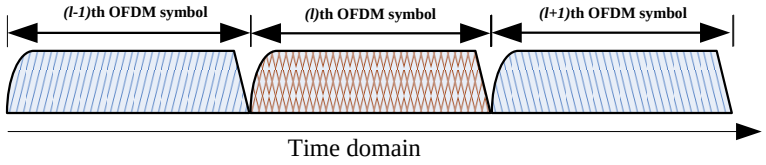

Figure 4.21. The OFDM symbol at the receiver after windowing.

Comparing Figure 4.21 with Figure 4.17, Figure 4.21 shows less overlapped and added area for each OFDM symbol. That would result in more tolerance to ISI. However, due to the OFDM signal, which is the combination of many frequencies, the signal is truncated in time domain by window function, and so the sinusoidal of each frequency will be truncated as well. Therefore, the OFDM power spectra will be shifted, as depicted in Figure 4.22. As a result, the subcarrier orthogonallity will be destroyed when the length of the window function becomes large. However, the data on each subcarrier can be completely demodulated by FFT calculation at the receiver side if the truncation is not too large when compared with the FFT size [74].

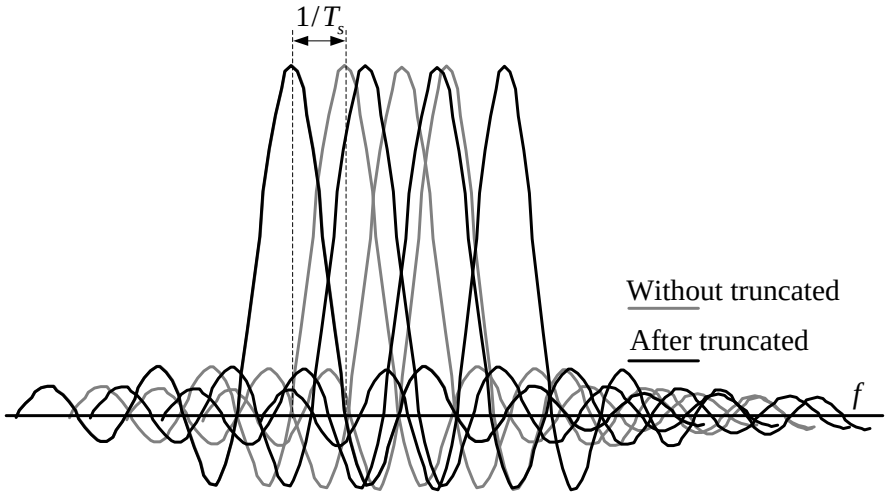

Figure 4.22. The OFDM power spectra after applying window function.

4.5 Experimental results of CP-free CO-OFDM

In this section, the experimental results for CP-free OFDM are discussed. The experimental setup is the same as that detailed in Section 4.3.3. Figure 4.23 shows four BER curves, denoted as

- the normal OFDM symbol (NOS) including a CP of 32 samples;
- the half and full window function with $w=8$ scheme of the CP-free OFDM, which are denoted by HWCPF and FWCPF, respectively; and
- the normal CP-free (NCPF) OFDM (without windowing).

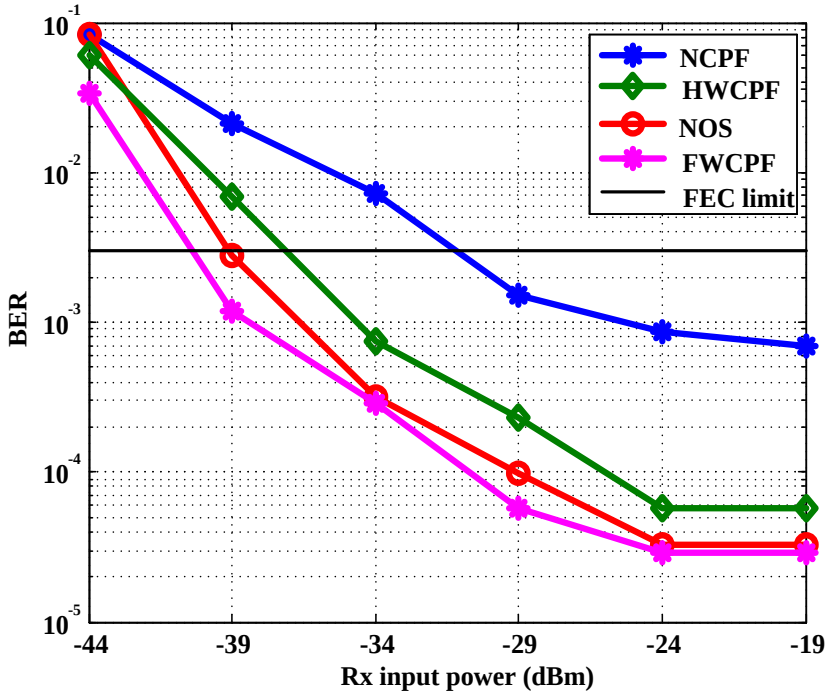

Figure 4.23. BER versus Rx input power with various OFDM symbol types.

From Figure 4.23, by comparing NCPF, HWCPF and FWCPF, it can be concluded that the performance is significantly improved when both half window and full window are applied. As expected, FWCPE gives slightly better BER than NOS. However, NOS still achieves better BER than HWCPF.

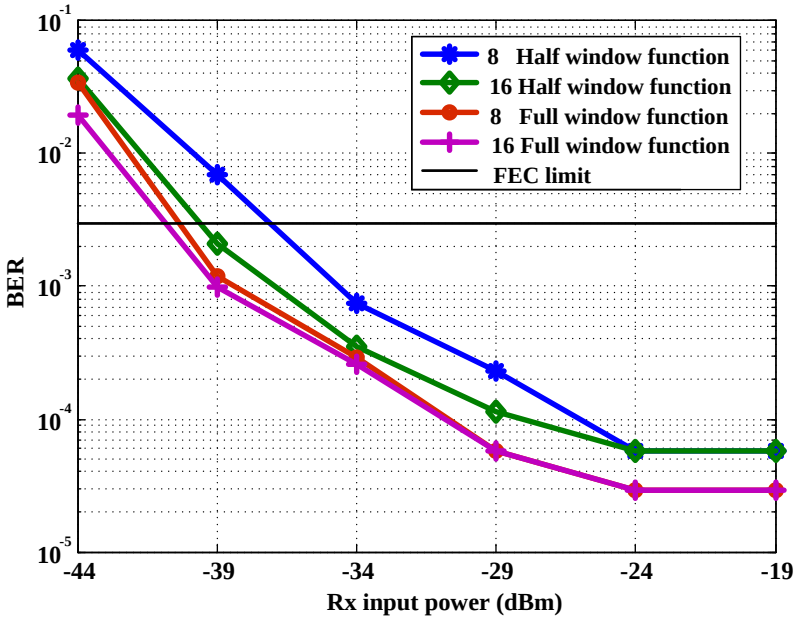

Figure 4.24. The BER with various Rx input powers and various window functions.

Figure 4.24 presents a system performance comparison of various windowing methods. Two window sizes of $w=8$ and $w=16$ for half and full windowing are investigated. The BER shows a significant improvement with a full window of size $w=16$ with full , while the half window gives a slightly worse BER at the Rx power input from −44 dBm to −34 dBm. However, full window with $w=8$ and $w=16$ give almost the same BER at the Rx inputs power from −34 dBm to −19 dBm. For example, at the Rx input power of −29 dBm and $w=16$, the BER of $5.79\cdot10^{-5}$ is obtained for half windowing, while a value of $3.24\cdot10^{-5}$ can be achieved for full windowing.

In addition, to improve the system performance, the moving average filter (MAF) is applied. It is located in the one-tap equalization, which is in between the channel impulse response extraction and the compensation unit, as shown in Figure 4.25.

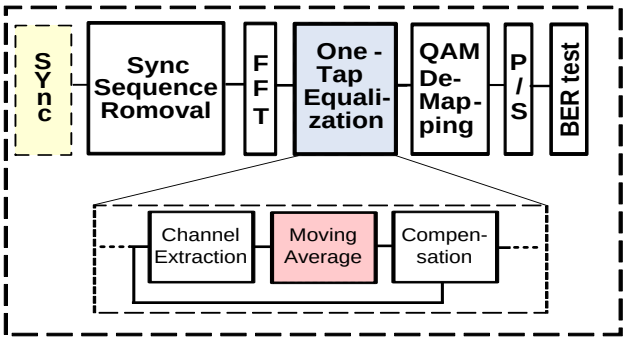

Figure 4.25. The improved channel estimation and compensation method using the MAF in the one-tap equalization unit.

Next, let $\hat{H}(k,d)$ be the estimated channel coefficient at the *k*th subcarrier on the *d*th OFDM symbol. Then, the MAF is given by

$$\hat{H}_{MAF}(k,d) = \frac{1}{L_{ft}} \sum_{m=0}^{L_{ft}-1} \hat{H}(k,d+m), \tag{4.24}$$

where, $\hat{H}_{MAF}(k,d)$ is the MAF of $\hat{H}(k,d)$ and L_{ft} is the number of filter taps. By Equations (4.10)-(4.15), $\hat{H}_{MAF}(k,d)$ is used to compensate for the optical channel distortion. For efficient hardware implementation, the number of filter taps should be selected as a power of 2, where L_{ft} = 1, 2, 4, 8, and 16 taps are considered.

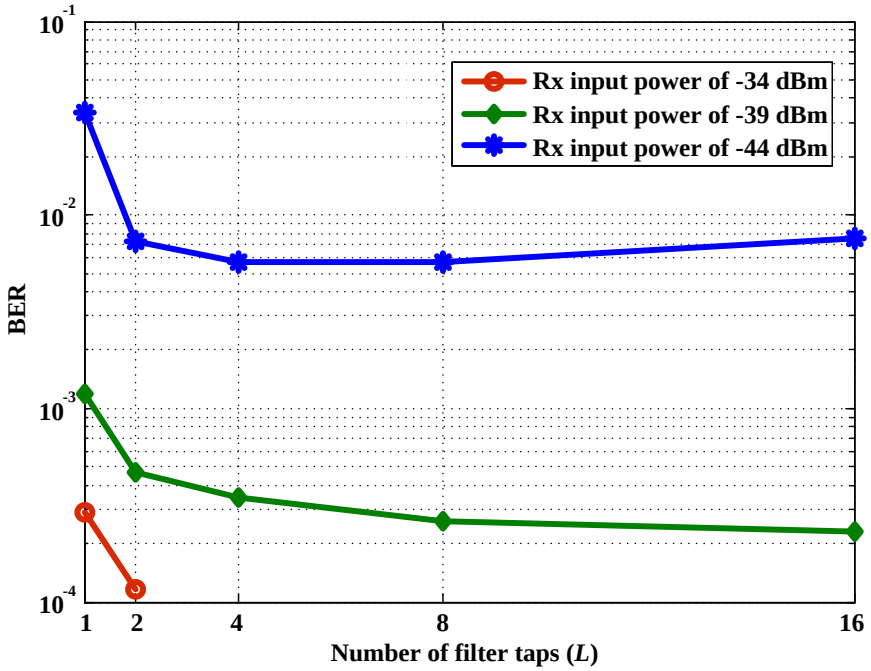

Figure 4.26. BER improvement by MAF for various Rx input power values.

Figure 4.26 presents the performance of the system improved by the MA filter. It can be clearly seen that for the filter taps L of 4, 8, and 16 at the RX input power of –34 dBm, the system is BER-free. For the RX input power of –39 dBm and –44 dBm, by increasing the number of filter taps up to L = 4, it shows a significant BER improvement. A further increase shows a slightly better result. For example, at L = 16, the BER is improved from $1.18 \cdot 10^{-3}$ to $2.31 \cdot 10^{-4}$ for the RX input power of –39 dBm.

It is observed that if we consider the length of window function w which acts as the length of CP, the achieved of communication distance is not so much when compared with using normal CP because of the fact that if w is too large, the loss of orthogonality of subcarriers is high. It degrades the system performance.

However, the achieved efficiency of OFDM symbols can be 100%, with no power loss due to adding a CP. Therefore, transmission rate and effective bandwidth are higher.

CHAPTER 5

Conclusion and Discussion

This dissertation has presented two main issues of coherent optical orthogonal frequency division multiplexing (CO-OFDM) receiver. The first one is the synchronization unit and the other is the optical channel distortion compensation unit.

For synchronization, the starting point of a FFT window and the carrier frequency offset (CFO) were explored. In comparison with the conventional and the widely used approach by Schmidl and Cox, the proposed method using orthogonal-code-aided method was found to be simpler and more accurate for FFT window synchronization technique. Simulation and experimental results demonstrated that the proposed method outperforms the alternative approach in terms of both hardware efficiency and system performance. Next, CFO effect must be cancelled. The two steps RF-pilot based method has been proposed. Only one RF-pilot tone is used. The proposed procedure can achieve a wide range of frequency offset estimation and higher OFDM frame efficiency.

The optical channel compensation unit is used to cancel the error phasor owning to the optical channel impacts. The optical channel effect of phase noise (PN) and chromatic dispersion (CD) are considered in this thesis. The pilot-aided optical channel compensation had been proposed. The known pilot is uniformly distributed to every OFDM symbol at the transmitter. Then, the channel coefficient is extracted from the known pilot at the receiver. Two interpolation methods are used for interpolating the estimated channel coefficients between the adjacent of the pilot data. The first one is linear interpolation and the second is second order interpolation. The proposed methods has been confirmed by both simulation and experimental. In addition, when comparing against the conventional OFDM, this approach exhibits an enhanced OFDM frame efficiency in addition to retention of the system performance.

Furthermore, intersymbol interference (ISI) in long haul optical communications becomes a serious problem such that the cyclic prefix (CP) also becomes large to neglect the ISI. However, CP reduces the effective communication speed. Therefore, to increase the effective communication speed while reducing the ISI effect, the CP-free OFDM symbol with applying window function has been considered. Experimental results indicated that the CP-free OFDM symbol with applying window function presents a significant improvement in terms of the system performance. Additionally, we found that the CP-free OFDM symbol with use of full window function yields a system performance of value nearly similar to that of the normal OFDM symbol operation at low Rx input powers.

However, for convenience purpose, only self-homodyne CO-OFDM detection has been studied for experimental measurements. In practical systems, heterodyne and polarization division multiplexing (PDM) detection are used. To make them compatible with this present work, it requires more modules to solve some other problems. This is a very sophisticated system and it can be a challenging topic in the future.

Finally, from the entire proposed scheme, this dissertation has presented a powerful and simple algorithm enabling proper performance of CO-OFDM, which can be implemented in hardware such as FPGA and ASIC. Therefore, in future work, the proposed method should be implemented in terms of the necessary hardware. However, the digital bit resolution for processing inside the FPGA or ASIC should also be considered. In additional, the fiber non-linearity was not taken into account in this thesis. Thus, for long haul optical communication distances, the non-linearity effect should be focused, which remains unclear or very complex to compensate in digital domain.

APPENDIX A

Mach-Zehnder-Modulator

Mach-Zehnder-Modulator (MZM) is an optical modulator and the equivalent physical model is shown in Figure A1.

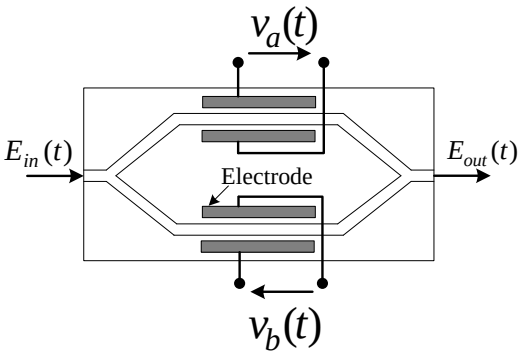

Figure A1. Schematic of optical Mach-Zehnder modulator.

Assuming that the insertion loss is free, the input and output relationship can be given by [74]

$$E_{out}(t) = E_{in}(t)\left(\frac{e^{\left(\frac{j\pi v_a(t)}{V_{\pi 1}}\right)} + e^{\left(\frac{j\pi v_b(t)}{V_{\pi 2}}\right)}}{2}\right), \tag{A1}$$

where $v_a(t)$ and $v_b(t)$ are the external voltage source. $V_{\pi 1}$ and $V_{\pi 2}$ are the control voltage to obtain phase shift of π in between upper and lower arms. Hence, if $v_a(t) = v_b(t) = v_e(t)$ and $V_{\pi 1} = V_{\pi 2} = V_\pi$ are obtained, a pure phase modulation is given and its input and output relation is expressed by

$$E_{out}(t) = E_{in}(t)e^{\left(\frac{jv_e(t)}{V_\pi}\pi\right)}, \tag{A2}$$

however, if $v_a(t) = -v_b(t) = v_e(t)/2$ and $V_{\pi 1} = V_{\pi 2} = V_\pi$, the MZM is operated as a pure amplitude modulation. The input and output relation can be given by

$$E_{out}(t) = E_{in}(t)\cos\left(\frac{v_e(t)}{2V_\pi}\pi\right), \tag{A3}$$

or expressed in power by

$$P_{out}(t) = P_{in}(t)\left(\frac{1}{2} + \frac{1}{2}\cos\left(\frac{v_e(t)}{V_\pi}\pi\right)\right). \tag{A4}$$

Therefore, if two MZMs are combined with a pure phase difference, the fully descriptive phase and amplitude can be achieved. In this case, it is called optical IQ modulator as shown in Figure A2.

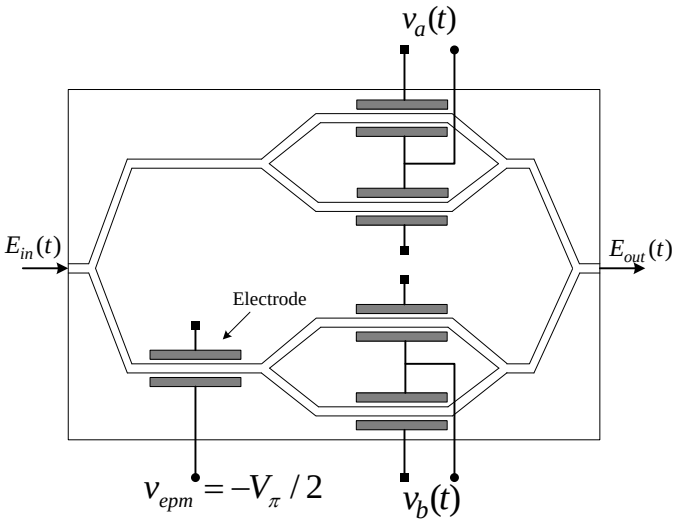

Figure A2. The optical IQ modulator operated as a combination of two MZMs.

From Figure A2, by assuming that the insertion loss is free and driving of the phase modulation unit is accomplished by $V_{epm} = -V_\pi / 2$, then the relationship between the input and output is given by [74],

$$E_{out}(t) = E_{in}(t)\left(\frac{1}{2}\cos\left(\frac{v_a(t)}{2V_\pi}\pi\right) + j\frac{1}{2}\cos\left(\frac{v_b(t)}{2V_\pi}\pi\right)\right), \tag{A5}$$

and the amplitude modulation $A(t)$ and phase modulation $\varphi(t)$ from the IQ modulation are calculated by Equation (A6) and Equation (A7), respectively.

$$A(t) = \left| \frac{E_{out}(t)}{E_{in}(t)} \right| = \frac{1}{2} \sqrt{\cos^2\left(\frac{v_a(t)}{2V_\pi} \pi \right) + j \cos^2\left(\frac{v_b(t)}{2V_\pi} \pi \right)}, \tag{A6}$$

$$\varphi(t) = angle\left(\cos\left(\frac{v_a(t)}{2V_\pi} \pi \right) + j \cos\left(\frac{v_b(t)}{2V_\pi} \pi \right) \right), \tag{A7}$$

where *angle* is phase calculation operator. In addition, MZM is worked at minimum transition point when compared with V_{epm} [74].

APPENDIX B

The Gold code

The Gold code is built from two maximal length sequences (m-sequence) or pseudo-noise (PN) generators, both of which are reduced to a modulo-2 operation, as shown in Figure B [26].

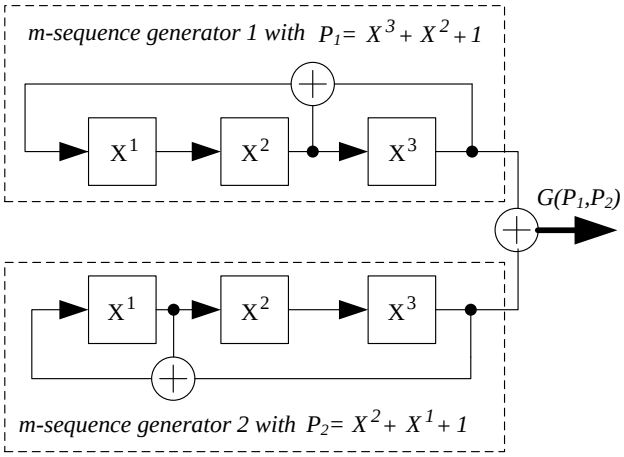

Sequence 1 :	1	0	1	1	0	0	1
Sequence 2 :	1	1	0	0	0	0	0
Sequence 3 :	0	0	1	0	0	1	0
Sequence 4 :	1	1	1	0	1	1	1
Sequence 5 :	0	1	1	1	1	0	0
Sequence 6 :	0	1	0	1	0	1	1

Figure B. An example of the Gold code generator.

In Figure B, the two m-sequence codes are called the preferred pair [26], which is denoted by P_1 and P_2. The length of the code sequence is denoted by $C = 2^M - 2$, where M is the number of the shift register. In this case, $C=6$. The code is constrained to 0 and 1.

APPENDIX C

The Barker code

The Barker code is another widely used code in direct-sequence spread spectrum (DSSS) in IEEE802.11b WLAN and radar systems [26]. This code is different from the Gold code in that it consists of only -1 and 1. Additionally, it is a short form of the PN code, but the correlation sidelobes are lower. The length is mostly 13, but can begin from 1, 2, 3, 4, 5, 7, 11 and 13. The codes are listed in the following table [55]

Table C: The Barker code sequence

Length	Code
1	-1
2	-1 1
3	-1 -1 1
4	-1 -1 1 -1
5	-1 -1 -1 1 -1
7	-1 -1 -1 1 1 -1 1
11	-1 -1 -1 1 1 1 -1 1 1 -1 1
13	-1 -1 -1 -1 -1 1 1 -1 -1 1 -1 1 -1

APPENDIX D

The code used in this thesis

However, in this thesis, a modification of the Gold code and Barker code is used. The sequence contains 1 and -1, similar to the Baker code. Hence, the I and Q channels are shifted 1 bit by adding bit 0 to Q at the first bit and adding bit 0 to the end of channel I. The code length is 32 bits in total. Finally, channel I is

1 1 -1 -1 -1 1 1 -1 1 -1 -1 -1 -1 -1 1 1 -1 1 -1 1 1 1 1 -1 1 1 -1 -1 -1 -1 1 0

and channel Q is

0 -1 -1 -1 -1 1 1 -1 -1 -1 1 1 1 -1 -1 1 -1 -1 1 -1 -1 1 1 -1 1 1 1 1 -1 1 -1 1

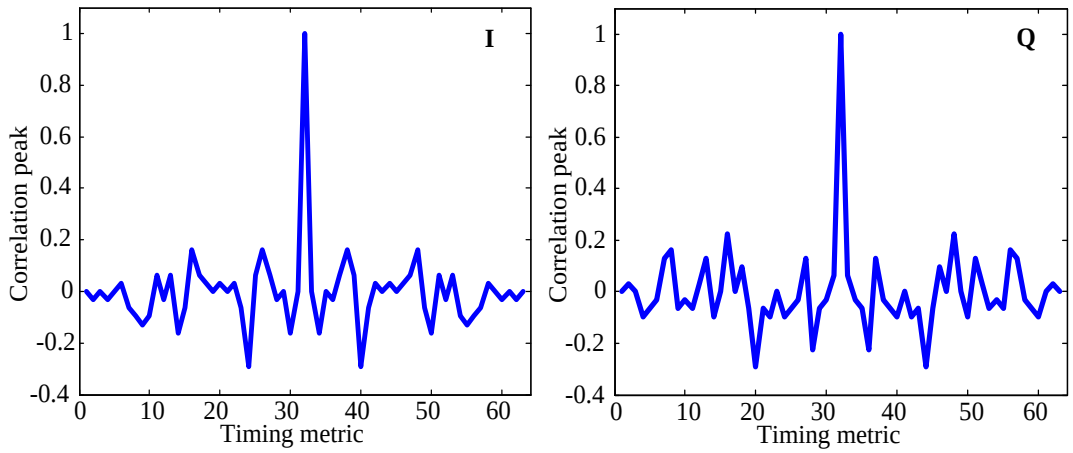

Figure D. The correlation peak between the I channel (*left*) and the Q channel (*right*).

Figure D presents the correlation peaks of the proposed code for the I and Q channels. The peak is high, and the sidelobes are low, i.e., lower than the a half of the peak.

References

[1] P.W Shumate, "*Fiber-to-the-Home: 1977–2007*," IEEE Journal of Lightwave Technology, vol.26, no.9, pp.1093-1103, 2008

[2] T. Ono, et al. "*Key technologies for terabit/second WDM systems with high spectral efficiency of over 1 bit/s/Hz*," IEEE Journal of Quantum Electronics, vol.34, no.11, pp.2080-2088, 1998.

[3] Govind P. Agrawal, "Fiber-Optic Communication Systems," 4th Edition, John Wiley & Son, 2010

[4] A. Barbieri, et al. "*OFDM versus Single-Carrier Transmission for 100 Gbps Optical Communication*," IEEE Journal of Lightwave Technology, vol.28, no.17, pp.2537-2551, 2010.

[5] S.L. Jansen, et al. "20-Gb/s OFDM Transmission over 4,160-km SSMF Enabled by RF-Pilot Tone Phase Noise Compensation," Proc. Optical Fiber Communication (OFC) Conference, California, USA, 2007.

[6] S.L. Jansen, et al. "*Long-haul transmission of 16x52.5-Gb/s polarization division multiplexed OFDM enabled by MIMO processing*," OSA Journal of Optical Networking, vol. 7, no. 2, pp. 173-182, 2008.

[7] S.L. Jansen, "*Multi-Carrier Approaches for Next-Generation Transmission: Why, Where and How?*," Proc. Optical Fiber Communication (OFC) Conference 2012, California, USA, 2012.

[8] W. Shieh, et al. "*Coherent optical OFDM: has its time come?*," OSA Journal of Optical Networking, vol. 7, issue 3, pp. 234-255, 2008.

[9] W. Shieh, et al. "*Coherent optical OFDM: theory and design*," Optics Express, vol. 16, issue 2, pp. 841-859, 2008.

[10] X. Yi, et al. "*Phase Estimation for Coherent Optical OFDM*," IEEE Photonics Technology Letters, vol.19, no.12, pp.919-921, 2007.

[11] Y. Tang, et al. "*Optimum Design for RF-to-Optical Up-Converter in Coherent Optical OFDM Systems*," IEEE Photonics Technology Letters, vol.19, no.7, pp.483-485, 2007.

[12] X. Yi, et al. "*Phase Noise Effects on High Spectral Efficiency Coherent Optical OFDM Transmission*," IEEE Journal of Lightwave Technology, vol. 26, pp. 1309 – 1316, 2008.

[13] K. Puntsri, et al. "*An Ultralow Complexity Algorithm for Frame Synchronization and IQ Alignment in CO-OFDM Systems*," Proc. Optical Fiber Communication (OFC) Conference 2013, California, USA, 2013.

[14] J. Armstrong, "*OFDM for Optical Communications*," IEEE Journal of Lightwave Technology, vol.27, no.3, pp.189-204, 2009.

[15] B.J.C. Schmidt, et al. "*100 Gbit/s Transmission using Single-Band Direct-Detection Optical OFDM*," Proc. Optical Fiber Telecommunications (OFC 2009), San Diego, USA, 2009.

[16] B.J.C. Schmidt, et al. "*Impact of PMD in -Receiver and Polarization-Diverse Direct-Detection Optical OFDM*," IEEE Journal of Lightwave Technology, vol. 27, no. 14, pp. 2792-2799, 2009.

[17] X.Q. Jin, et al. "*Real-time demonstration of 128-QAM-encoded optical OFDM transmission with a 5.25bit/s/Hz spectral efficiency in simple IMDD systems utilizing directly modulated DFB lasers*," Optics Express, vol.17, no.22, pp. 20484–20493, 2009.

[18] R.P. Giddings, et al. "*Experimental Demonstration of Real-Time Optical OFDM Transmission at 11.25 Gb/s over 500m MMFs Employing Directly Modulated DFB Lasers*," IEEE Photonics Technology Letters, vol.23, no.1 pp.51-53, 2011.

[19] S. Chen, et al. "*Real-time IQ Imbalance compensation for coherent optical OFDM transmission*," Proc. Optical Fiber Communication (OFC) Conference 2011, California, USA, 2011.

[20] A. Al. Amin, et al. "*A hybrid IQ imbalance compensation method for optical OFDM transmission*," Optics Express, vol. 18, issue 5, pp. 4859-4866, 2010.

[21] S. Chung, et al. "*Effect of IQ mismatch compensation in an optical coherent OFDM receiver*," IEEE Photonics Technology Letters, vol.22, no.5, pp.308-310, 2010.

[22] Sang-Yuep Kim, et al. "*Cyclic prefix free 10-Gb/s OFDM for a DML-based long-reach optical access using joint time and frequency domain equalization algorithm*," Proc. Optical Fiber Communication (OFC) Conference 2011, California, USA, 2011.

[23] C. Chen, et al. "*Zero-guard-interval coherent optical OFDM with overlapped frequency-domain CD and PMD equalization*," Optics Express, vol. 19, issue 8, pp.7451-7467, 2011.

[24] B. Liang, et al. "*No-guard-interval coherent optical OFDM with self-tuning receiver*," Optics Express, vol. 19, issue 3, pp.2181-2186, 2011.

[25] J. Heiskala, et al. "OFDM Wireless LANs: A Theoretical and Practical Guide," Pearson, 2001.

[26] H. Schulze, et al. “Theory and applications of OFDM and CDMA: wideband wireless communications OFDM and CDMA,” John Wiley & Son, 2005.

[27] https://ccrma.stanford.edu/~jos/st/Orthogonality_Sinusoids.html

[28] J. Proakis, et al. “Digital Signal Processing: Principles, Algorithms, and Applications,” 4th Edition, Pearson Education, 2007.

[29] John G. Proakis, “Digital Communication,” 4th Edition, McGraw-Hill Higher Education, 2000.

[30] Richard G. Lyons, “Understanding Digital Signal Processing,” 3rd Edition, Pearson Education, 2011.

[31] V. Madisetti, “The Digital Signal Processing Handbook,” CRC Press, November 2009.

[32] R. V. Nee, et al. “OFDM for Wireless Multimedia Communications,” Artech House Inc, December, 1999.

[33] M. A. Jarajreh, et al. “Improving chromatic dispersion tolerance in long-haul fibre links using coherent OOFDM,” http://soe.unn.ac.uk/ocr/

[34] M. Nakazawa, et al., “High spectral density optical communication technologies (Optical and Fiber Communications Reports),” Springer, 2010.

[35] Reinhold Noé “Essentials of modern optical fiber communication,” Springer, 2011.

[36] Timo Pfau, “Development and real-time implementation of digital signal processing algorithms for coherent optical receivers,” Doctoral Thesis, Faculty of Electrical Engineering, Information and Mathematics, University of Paderborn, 2009.

[37] C. Thein, “Analysis of optical multicarrier systems,” Diplomar Thesis, Faculty of Electrical Engineering, Information and Mathematics, University of Paderborn, 2009.

[38] http://www.itu.int/

[39] T. Sergey, et al., “*An introduction to the fundamentals of PMD in fibers*,” white paper, http://www.corning.com/opticalfiber/index.aspx.

[40] B. Schmidl, et al., “*Impact of PMD in Single-Receiver and Polarization-Diverse Direct-Detection Optical OFDM*,” IEEE Journal of Lightwave Technology, vol.27, no.14, pp.2792-2799, 2009.

[41] E. Desurvire, et al., “*High-Gain Erbium-Doped Traveling-Wave Fiber Amplifier*,” Optics Letters, vol. 12, 11, pp. 888-890, 1987.

[42] R. Mears, et al., "*Low-Noise Erbium-Doped Fibre Amplifier at 1.54pm*," Electronics
Letters, vol. 23, 19, pp. 1026-1028, 1987.

[43] Munier, F., et al., "*Estimation of Phase Noise for QPSK Modulation over AWGN Channels*," Proc. GigaHertz symposium 2003, Linköping, Sweden, 2003.

[44] V. Exter, et al., "*Excess phase noise in self-heterodyne detection*," IEEE Journal of Quantum Electronics, vol.28, no.3, pp.580-584, Mar. 1992.

[45] N. Wiener, "*Extrapolation, Interpolation, and Smoothing of Stationary Time Series*," Cambridge, The MIT Press, 1964.

[46] S.L. Jansen, et. al., "*Coherent Optical 25.8-Gb/s OFDM Transmission over 4,160-km SSMF*," IEEE/OSA Journal of Lightwave Technology (JLT), vol. 26, no. 1, pp. 6-15, 2008.

[47] J. Kim, et. al., "*IQ imbalance compensation for OFDM based wireless. LANs*," IEICE Electronics Express, Vol.4, No.16, pp.524–530, 2007.

[48] A. B. R. Bahai, et. al., "Multi-Carrier Digital Communications: Theory and Applications of OFDM, 2nd ed.,New York: SpringerVerlag, 2004.

[49] S. C. Yong, et. al., "MIMO-OFDM Wireless Communications with MATLAB®," John Wiley & Son, 2010.

[50] Y. Mostofi, et. al., "*Mathematical analysis of the impact of timing synchronization errors on the performance of an OFDM system*," Transactions on Communications, IEEE, vol.54, no.2, pp. 226- 230, 2006.

[51] T. M. Schmidl, et. al., "*Robust frequency and timing synchronization for OFDM*," IEEE Transactions on Communications, vol.45, no.12, pp.1613-1621., 1997.

[52] T. Liang, et. al., "*An adaptive algorithm of fine synchronization for CO-OFDM system*," Proc. IEEE Communications and Photonics Conference and Exhibition 2011, Shanghai, China, 2011.

[53] S. Kumar, "Impact of nonlinearities on fiber optic communications," Springer, 2011.

[54] D. Esmael, et. al., "*Spreading codes for direct sequence CDMA and wideband CDMA cellular networks*," IEEE Communications Magazine, vol.36, no.9, pp.48-54, 1988.

[55] J. Wen, et. al., "*PN code-aided timing estimation, channel estimation and signal compensation in OFDM systems*," Digital Signal Processing, Elsevier, Volume 20, Issue 3, P. 860-868, May 2010.

[56] P. H. Moose, "*A technique for orthogonal frequency division multiplexing frequency offset correction*," IEEE Transactions on Communications, vol.42, no.10, pp.2908-2914, 1994.

[57] S. Cao, et al. "*Full-range pilot-assisted frequency offset estimation for OFDM systems*," Proc. Optical Fiber Communication (OFC) Conference 2013, California, USA, 2013.

[58] F. Buchali, et al. "*Improved frequency offset correction in coherent optical OFDM systems*," Proc. European Conference on Optical Communication (ECOC), Brussels, Belgium, 2008.

[59] S. Randel, et. al., "*Analysis of RF-Pilot-Based Phase Noise Compensation for Coherent Optical OFDM Systems*," IEEE Photonics Technology Letters, vol.22, no.17, pp.1288-1290, Sept.1, 2010.

[60] M. Thompson, "*Low-latency, high-speed numerically controlled oscillator using progression-of-states technique*," IEEE Journal of Solid-State Circuits, vol.27, no.1, pp.113-117, Jan 1992.

[61] A.I. Ahmed et al. "*FPGA implementation and performance evaluation of a digital carrier synchronizer using different numerically controlled oscillators*," Proc. Canadian Conference on Electrical and Computer Engineering 2007, Vancouver, Canada.

[62] D. Petrovic, et al. "Effects of Phase Noise on OFDM Systems With and Without PLL: Characterization and Compensation," in IEEE Transactions on Communications, vol.55, no.8, pp.1607-1616, Aug. 2007.

[63] W. Shieh, et. al., "*Coherent optical orthogonal frequency division multiplexing*," Electronics Letters, vol. 42, no. 10, pp. 587–589, 2006.

[64] F. Gao, et. al., "*Blind Channel Estimation for OFDM Systems via a Generalized Precoding*," IEEE Transactions on Vehicular Technology, vol.56, no.3, pp.1155-1164, 2007.

[65] S.A. Banani, et. al., "*OFDM with Iterative Blind Channel Estimation*," IEEE Transactions on Vehicular Technology, vol.59, no.9, pp.4298-4308, 2010.

[66] Tangdi Zhang, et. al., "*Blind adaptive scheme for joint frequency offset and channel estimation in OFDM systems*," Proc. IEEE International Conference on Signal Processing Systems (ICSPS), Dalian, China, 2010.

[67] S. Coleri, et. al., "*Channel estimation techniques based on pilot arrangement in OFDM Systems*," IEEE Transactions on Broadcasting, vol.48, no.3, pp. 223-229, 2002.

[68] Meng-Han Hsieh, et al., "*Channel Estimation for OFDM Systems Based on Comb-type Pilot Arrangement in Frequency Selective Fading Channels*," IEEE Transactions on Consumer Electronics, vol.44, no.1, page 217-225, 1999.

[69] George W. Collins, II, "*Fundamental Numerical Methods and Data Analysis*," Harvard University Press (2003), 2003.

[70] S. McKinley, et al., "*Cubic Spline Interpolation*," Math 45: Linear Algebra, 1998.

[71] Burton R. Saltzberg, "*Performance of an efficient parallel data transmission system*," IEEE Transactions on Communication Technology, Vol. 15, No. 6., pp. 805-811, 1967.

[72] R. Chang, et al., "*A Theoretical Study of Performance of an Orthogonal Multiplexing Data Transmission Scheme*," IEEE Transactions on Communication Technology, vol.16, no.4, pp.529-540, 1968.

[73] S. Weinstein, et al., "*Data Transmission by Frequency-Division Multiplexing Using the Discrete Fourier Transform*," IEEE Transactions on Communication Technology, vol.19, no.5, pp.628-634, 1971.

[74] Matthias Seimetz, "High-Order Modulation for Optical Fiber Transmission," Spinger, 2009.

[75] Xian Zhou; , et al., "*Efficient Joint Carrier Frequency Offset and Phase Noise Compensation Scheme for High-Speed Coherent Optical OFDM Systems*," IEEE Journal of Lightwave Technology (JLT), vol.31, no.11, pp.1755-1761, 2013.

Some importance glossaries

Variable	Unit	Description
f_n	Hz	Frequency on each nth subcarrier
f_{offset}	Hz	Frequency offset between transmitter and receiver
f_{Tx}	Hz	Frequency at the transmitter
f_{Rx}	Hz	Frequency at the receiver
N_C		Number of IFFT/FFT size
f_n	Hz	Frequency spacing
T_s	s	Sampling rate
d_k		Constellation diagram point
T	s	Symbol period
N_{CP}		Number of cyclic prefix
N_{sym}		Total length of one complete OFDM symbol
N_p		Number of pilot data
N_{uf}		Number of useful data
$\tilde{a}$	V	Electrical drive signal of upper MZM
$\tilde{b}$	V	Electrical drive signal of lower MZM
E_s	V/m	Electrical field of the transmitter laser
E_u	V/m	Input electrical field into the upper MZM
E_s	V/m	Input electrical field into the lower MZM
E_a	V/m	Output electrical field of the upper MZM
E_b	V/m	Output electrical field of the lower MZM
E_{TX}	V/m	Output electrical field of the optical transmitter
$\Re$		In-phase component
$\Im$		Quadrature component
P_s	W	Optical power of the transmitter laser
ω_s	rad	Angular signal frequency
φ_s	rad	Signal phase
E_r	V/m	Received electrical field of the optical signal
E_{LO}	V/m	Electrical field of the local oscillator
$\tilde{n}$		Noise variable
ω_{IF}	rad	Angular carrier frequency
θ	rad	Signal phase different between Tx and Rx
R	A/W	Photodiode responsivity
λ	m	Wavelength
D	ps/(nm·km)	Chromatic dispersion coefficient
Δv	Hz	Laser linewidth

σ^2	Variance of laser phase noise
β	Propagation constant
τ_{CD}	The pulse broadening owning to CD
Δn	Timing offset in simple
ΔL	Number of overlap and add in sample
$\hat{H}$	Estimated channel coefficients
$\hat{H}_p$	Estimated channel coefficients on the pilot data
$\hat{H}_{CPE}$	Estimated phase by using CPE method
$\hat{H}_{MAF}$	Estimated channel coefficients after applying MA filter
g_{half}	Half window function
g_{full}	Full window function

Some importance acronyms and abbreviations

Abbreviations	Description
IPTV	Internet protocol television
FTTH	Fiber-to-the-home
WDM	Wavelength division multiplexing
QAM	Quadrature amplitude modulation
QPSK	Quadrature phase-shift keying
BPSK	Binary phase-shift keying
CD	Chromatic dispersion
PMD	Polarization mode dispersion
SC	Single carrier
RF	Radio frequency
OFDM	Orthogonal frequency division multiplexing
CP	Cyclic prefix
DIFT	Discrete invert Fourier transform
DFT	Discrete Fourier transform
CFO	Carrier frequency offset
SCFO	Sampling clock frequency offset
ISI	Intersymbol interference
ICI	Intercarrier interference
TS	Training Symbol
CPE	Common phase error
PN	Phase noise
ASE	Amplified spontaneous emission
IFFT	Invert fast invert Fourier transform
FFT	Fast invert Fourier transform
FDM	Frequency division multiplexing
GFB	Guard band frequency
ADC	Analong to digital convertor
DAC	Digital to analong convertor
CIR	Channel impulse response
PAPR	Peak to average power ratio
DSP	Digital signal processing
MZM	Mach-Zehnder modulator
Tx	Transmitter
Rx	Receiver
DGD	Differential group delay
SOP	State of polarization
EDFA	Erbium doped fiber amplifier
AWGN	Additive white Gaussian noise
OSNR	Optical signal to noise ratio
dB	Decibel
FWHM	Full width at half-maximum
ITU-T	International Telecommunication Union -Telecommunication Standardization Sector

VOA	Variable optical attenuator
LO	Local oscillator
MAF	Moving average filter
LS	Least-square
ECL	External cavity laser
SSMF	Standard single-mode optical fiber
MLH	Maximum likelihood
FEC	Forward error control
BER	Bit error rate
FPGA	Field programmable gate array
ASIC	Application specific Integrated Circuit

List of publications

K. Puntsri, O. Jan, A. Al-Bermani, C. Wördehoff, S. Hussin, M.F. Panhwar, R. Noé and U. Rückert "*Pilot-aided CD and PN Compensation Simultaneously in CO-OFDM Systems*," in Proc. Conf. 18th Opto-Electronics and Communications Conference OECC 2013, 29-4 July 2013, Kyoto, Japan.

K. Puntsri, O. Jan, A. Al-Bermani, C. Wördehoff, S. Hussin, M.F. Panhwar, and U. Rückert, R. Noé "ISI Tolerance of Cyclic Prefix Free Coherent Optical OFDM Communication System," 14. ITG-Fachtagung "Photonische Netze," 6-7 May 2013, Leipzig, ITG-Fachbericht.

K. Puntsri, O. Jan, A. Al-Bermani, C. Wördehoff, S. Hussin, M.F. Panhwar, R. Noé and U. Rückert "*An Ultralow Complexity Algorithm for Frame Synchronization and IQ Alignment in CO-OFDM Systems*," Proc. OFC/NFOEC 2013, California, USA, 2013.

O. Jan, D. Sandel, **K. Puntsri**, A. Al-Bermani, M. El-Darawy, and R. Noé, "The robustness of subcarrier-index modulation in 16-QAM CO-OFDM system with 1024-point FFT," Optics Express, Vol. 20, Issue 27, pp. 28963-28968, 2012.

O. Jan, D. Sandel, M. El-Darawy, **K. Puntsri**, A. Al-Bermani and R. Noé, "Phase Noise Robustness of SIM-OFDM in CO-OFDM Transmission," Proc. European Conference on Optical Communication (ECOC2012), Amsterdam, The Netherlands, 16-20 Sept. 2012.

A. Al-Bermani, C. Wördehoff, O. Jan, **K. Puntsri**, U. Rückert and R. Noé, "Real-time Comparison of Blind Phase Search with Different Angle Resolutions for 16-QAM," IEEE Photonics 2012 Conference (IPC12), formerly (LEOS), 23-27 Sept. 2012, San Francisco, California, USA.

K. Puntsri, V. Mirvoda, S. Hussin, O. Jan, A. Al-Bermani, M. F. Panhwar and R. Noé, "A Low Complexity and High Accuracy Frame Synchronization for Optical OFDM and PolMux-Optical OFDM," IEEE Photonics 2012 Conference (IPC12), formerly (LEOS), 23-27 Sept. 2012, San Francisco, California, USA.

S. Hussin, **K. Puntsri** and R. Noe, "Efficiency enhancement of RF-pilot-based phase noise compensation for coherent optical OFDM systems," in Proc. 17th International OFDM Workshop ,(InOWo'12), 29-30 Aug. 2012, Essen, Germany

K. Puntsri, D. Sandel, S. Hussin, O. Jan, A . Al-Bermani, M. F. Panhwar, and R. Noé, "A Novel Method for IQ Imbalance Compensation in CO-OFDM Systems," in Proc. Conf. 17th Opto-Electronics and Communications Conference OECC 2012, Paper 4B3-1, 2-6 July 2012, Busan, South Korea.

M. F. Panhwar, M. El-Darawy, **K. Puntsri** and R. Noé, "Reduced Sampling Rate Frequency Domain CD Equalization for 112 Gb/s PDM-QPSK," in Proc. Conf. 17th Opto-Electronics and Communications Conference OECC 2012, Paper 5B4-4, 2-6 July 2012, Busan, South Korea.

O. Jan, D. Sandel, M. El-Darawy, **K. Puntsri**, A. Al-Bermani, and R. Noé, "Fiber Nonlinearity Tolerance of SIM-OFDM in CO-OFDM Transmission," in Proc. Conf. 17th Opto-Electronics and Communications Conference OECC 2012, Paper P1-14, 2-6 July 2012, Busan, South Korea.

B. Koch, R. Noé, V. Mirvoda, **K. Puntsri**, and D. Sandel, "Two-sided (15 krad/s at Input, 200 rad/s at Output) Endless Optical Polarization Tracking," in Proc. Conf. 17th Opto-Electronics and Communications Conference OECC 2012, Paper 6F3-4, 2-6 July 2012, Busan, South Korea.

A. Al-Bermani, C. Wördehoff, **K. Puntsri**, O. Jan, U. Rückert, R. Noé, "Phase Estimation Filter Length Tolerance for Real-Time 16-QAM Transmission System Using QPSK Partitioning," Workshop der ITG-Fachgruppe 5.3.1, 5-6 July 2012, Gewerkschaftshaus Nürnberg, Germany.

K. Puntsri, V. Mirvoda, S. Hussin, Omar H.A. Jan, A. Al-Bermani, M. F. Panhwar, R. Noé, "A Low Complexity and High Accuracy Frame Synchronization for PolMux-Optical OFDM," Workshop der ITG-Fachgruppe 5.3.1, 5-6 July 2012, Gewerkschaftshaus Nürnberg, Germany.

M. F. Panhwar, M. El-Darawy, **K. Puntsri**, R. Noé, "ADC Sampling Rate Requirements for the Frequency-Domain CD Equalization," Workshop der ITG-Fachgruppe 5.3.1, 5. -6. July 2012, Gewerkschaftshaus Nürnberg, Germany.

S. Hussin, **K. Puntsri** and R. Noe, "Performance Analysis of RF-Pilot Phase Noise Compensation Techniques in Coherent Optical OFDM Systems," in Proc. Conf. 17th European Conference on Network and Optical Communications NOC 2012, 20-22. June 2012, Vilanova I La Geltru, Barcelona, Spain.

O. Jan, M. El-Darawy, A. Al-Bermani, **K. Puntsri**, R. Noe, "Mitigation of Fiber Nonlinearities in CO-OFDM Systems," 13. ITG-Fachtagung "Photonische Netze," 7.-8. Mai 2012, Leipzig, ITG-Fachbericht 233, P3, pp. 170-172, ISBN 978-3-8007-3437-5.

A. Al-Bermani, C. Wördehoff, **K. Puntsri**, O. Jan, U. Rückert, R. Noe, "Real-time Synchronous 16-QAM Optical Transmission System Using Blind Phase Search and QPSK Partitioning Carrier Recovery Techniques," 13. ITG-Fachtagung "Photonische Netze," 7-8. Mai 2012, Leipzig, ITG-Fachbericht 233, P12, pp. 231-215, ISBN 978-3-8007-3437-5.

O. Jan, M. El-Darawy, **K. Puntsri**, A. Al-Bermani, R. Noé, "RF-pilot-based nonlinearity compensation in frequency domain for CO-OFDM transmission," Proc. SPIE Vol. 8434, Paper 8434-18, 16-19. April 2012, Brussels, Belgium.

S. Hussin, **K. Puntsri** and R. Noe, "Performance Analysis of Optical OFDM systems," in Proc. Conf. 3rd International Congress on Ultra Modern Telecommunications and Control Systems ICUMT 2011, 5-7. Oct. 2011, Budapest, Hungary.

K. Puntsri, S. Hoffmann, S. Hussin, A. Al-Bermani and R. Noe, "A Low Complexity and High Accuracy Frame Synchronization for Optical OFDM Systems," in Proc. Conf. 16th Opto-Electronics and Communications Conference OECC 2011, 4-8 July 2011, Kaohsiung, Taiwan.

Ali Al-Bermani, Christian Wördehoff, Sebastian Hoffmann, **Kidsanapong Puntsri**, Ulrich Rückert and Reinhold Noé, "Realtime Implementation of Square 16-QAM Transmission System," Proc. SPIE 8065, 806519 (2011), 28 March 2011, Strasbourg, France.

A. Al-Bermani, C. Wördehoff, S. Hoffmann, **K. Puntsri**, T. Pfau, U. Rückert, R. Noé, "Realtime 16-QAM Transmission with Coherent Digital Receiver," OECC 2010, 5-9. Juli 2010, Sapporo, Japan.

B. Koch, R. Noé, V. Mirvoda, D. Sandel, **K. Puntsri**, "Tracking Speed Comparison of Endless Polarization Controller for Single versus Multiplexed Polarizations," in Proc. Signal Processing in Photonic Communications (SPPCom), Optical Society of America, SPWC1, 21-24 June 2010, Karlsruhe, Germany.

S. Hoffmann, C. Wördehoff, A. Al-Bermani, M. El-Darawy, **K. Puntsri**, U. Rückert, R. Noé, "Hardware-effiziente Phasenschätzung für kohärenten QAM-Empfang mit regulären Stern-Konstellationen," 11. ITG-Fachtagung "Photonische Netze," 3-4 May 2010 Leipzig, Germany, ITG-Fachbericht 222, pp. 221-224.

B. Koch, R. Noé, V. Mirvoda, D. Sandel, **K. Puntsri**, V. Filsinger, "Optisches Polarisationsdemultiplex von 200-Gb/s-PM-RZ-DQPSK bei endlosen Polarisationsänderungen bis 40 krad/s," 11. ITG-Fachtagung "Photonische Netze," 3-4 May 2010 Leipzig, Germany, ITG-Fachbericht 222, pp. 233-236.

B. Koch, R. Noé, D. Sandel, V. Mirvoda, V. Filsinger, **K. Puntsri**, "200-Gb/s, 430-km PDM-RZ-DQPSK (4 Bit/Symbol) Transmission with 10 krad/s Endless Polarization Tracking," Proc. OFC/NFOEC 2010, San Diego, CA, Paper OThD4 , Mar. 21-25, 2010.

B. Koch, R. Noé, V. Mirvoda, D. Sandel, V. Filsinger, **K. Puntsri**, "40-krad/s Polarization Tracking in 200-Gb/s PDM-RZ-DQPSK Transmission over 430 km," IEEE Photonics Technology Letters, VOL. 22, No. 9, pp. 613-615, May 1, 2010.

S. Hoffmann, C. Wördehoff, A. Al-Bermani, M. El-Darawy, **K. Puntsri**, U. Rückert, R. Noe, “Hardware-Efficient Phase Estimation for Digital Coherent Transmission with Star Constellation QAM,” IEEE Photonics Journal, Vol. 2 , No. 2, pp. 174 - 180 (invited).